

Doctoral Thesis

Signal Processing for Ultra Wideband Transceivers

Christoph Krall

Faculty of Electrical Engineering and Information Technology
Graz University of Technology, Austria

First Examiner:
Univ.-Prof. Dipl.-Ing. Dr.techn. Gernot Kubin
Graz University of Technology, Austria

Second Examiner:
Prof. Dr.-Ing. Ilona Rolfes
Leibniz Universität Hannover, Germany

Co-Advisor:
Dipl.-Ing. Dr. Klaus Witrissal
Graz University of Technology, Austria

Graz, April 2008

Kurzfassung

In dieser Dissertation werden neuartige Implementierungsansätze für standardisierte und nicht standardisierte Ultra-Breitband (UBB) Systeme präsentiert. Diese Implementierungsmethoden inkludieren Signalverarbeitungsalgorithmen für UBB Systeme im Sendempfänger Front-End sowie im digitalen Back-End.

Die Parallelisierung des Sendempfängers im Frequenzbereich wurde mit einer hybriden Filterbank durchgeführt. Das standardisierte MB-OFDM Signalisierungsschema erlaubt eine Parallelisierung im Frequenzbereich durch die Verteilung der orthogonalen Träger auf mehrere Recheneinheiten. Weiters wurde die Kanalimpulsantwort im Frequenzbereich parallelisiert und die dadurch auftretenden Effekte untersucht. Eine geringfügig schlechtere Performanz wurde beobachtet, welche auf die verkürzten Filterantworten und Fehlanpassungen im analogen Front-End zurückgeführt werden können. Für diese Performanzeinbußen wurden geeignete Fehlermaße definiert.

Für die UBB Signalgenerierung wurde eine neuartige Methode erarbeitet. Zu diesem Zweck werden mehrere Digital-zu-Analog Umsetzer in einer Struktur verwendet, um eine flexible Signalgenerierung zu ermöglichen. Zuerst wurden die Umsetzer als ideal an den Abtastzeiten ausgerichtet angenommen, sodaß keine Fehlanpassungsspektren auftreten. Weiters wurden Zeitfehler betrachtet und eine Kompensationsarchitektur für die auftretenden Fehler erarbeitet. Diese digitale Vorverzerrung wurde auf einem Demosystem implementiert und kompensiert die Fehlanpassungsspektren um ca. 20 dB.

Des Weiteren wurden Empfängerarchitekturen für das standardisierte IEEE802.15.4a Signalisierungsschema, welches breitbandige Pulse verwendet, untersucht. Drei Empfänger wurden in Einzel- und Mehrbenutzerszenarien verglichen. Ein in dieser Dissertation ausgearbeiteter Empfänger zeigt einen großen Performanzgewinn, da der im Signal vorhandene Spreizcode genutzt wird.

Um nichtlineare Verzerrungen welche bei hohen Datenraten in nichtkohärenten Empfänger-Front-Ends auftreten zu entzerren, wurde ein neuartiger Entzerralgorithmus ausgearbeitet. Der nichtlineare Entzerrer zweiter Ordnung wird mittels der Methode der kleinsten Fehlerquadrate optimiert und berechnet. Dieser nichtlineare Entzerrer ist eine Verallgemeinerung des bekannten linearen Entzerrers. Weiters wurde dieser Entzerrer mit einem adaptiven Lernalgorithmus verglichen, welcher asymptotisch gegen die hier vorgestellte Lösung konvergiert. Dieser Entzerrer verbessert die nichtkodierte Bitfehlerrate um den Faktor 20.

Abstract

In this thesis novel implementation approaches for standardized and non-standardized ultra wide-band (UWB) systems are presented. These implementation approaches include signal processing algorithms to achieve processing of UWB signals in transceiver front-ends and in digital back-ends.

A parallelization of the transceiver in the frequency-domain has been achieved with hybrid filterbank transceivers. The standardized MB-OFDM signaling scheme allows parallelization in the frequency domain by distributing the orthogonal multicarrier modulation onto multiple units. Furthermore, the channel's response to wideband signals has been parallelized in the frequency domain and the effects of the parallelization have been investigated. Slight performance decreases are observed, where the limiting effects are truncated sidelobes and filter mismatches in analog front-ends. Measures for the performance loss have been defined.

For UWB signal generation, a novel broadband signal generation approach is presented. For that purpose, multiple digital-to-analog converters are used in an array to achieve flexible (adaptive) signal generation. Firstly, the converters in the array are assumed to be perfectly aligned to the clock signals, such that no mismatch spectra occur. Secondly, time offsets are introduced in the converter model and a compensation algorithm is presented. A digital predistortion of the signals, to compensate for the mismatch spectra, is presented and implemented, which achieves a reduction of the mismatch spectra by app. 20 dB.

Furthermore, receiver architectures for the standardized IEEE802.15.4a signaling scheme, which is a pulse-based signaling scheme, are investigated. A comparison of three receivers in single and multi-user environments is presented. It is seen that the receiver proposed in this thesis has superior performance in the multi-user case, because it uses spreading information present in the standardized UWB signals.

To reduce the distortions encountered in non-coherent receiver architectures at high data rates, a novel equalization algorithm for nonlinear receiver front-ends is presented. The nonlinear second-order equalizer can be optimized and computed according to a minimum mean squared error (MMSE) criterion. It is found that the nonlinear equalizer is a generalization of the linear equalizer equations. The solution is compared to an iterative learning algorithm (LMS), which shows asymptotic convergence to the presented solution. The presented equalizer improves the uncoded BER floor by a factor of 20.

Acknowledgement

First of all, I want to thank my two main supervisors throughout this thesis Dr. Klaus Witrissal and Prof. Gernot Kubin for their continuous support and help. Many thanks also to Prof. Ilona Rolfes from the University of Hannover, Germany for being the second examiner. I have to thank the Austrian Research Centers which funded this project, especially I want to thank Franco Fresolone, Gerhard Humer, and Reinhard Kloibhofer for their help and support during the three years. Thanks also to the Christian Doppler Forschungsgesellschaft for the three years funding of the project. My thanks also to Prof. Alle-Jan van der Veen and Dr. Geert Leus for their support and comments during my research visit in Delft. Thanks also to the Circuits and Systems Group at TU Delft, you made life easier, far far away from home. Additionally, I want to thank Zoubir Irahhautes for performing the measurements with me. Thanks also to Sven Dortmund from the Institute of Radiofrequency and Microwave Engineering from University of Hanover for the perfect measurements of our UWB antennas. Furthermore, I want to thank Dr. Heinz Koepl from Ecole Polytechnique Federale de Lausanne, Switzerland for his valuable suggestions and discussions. Thanks also to Manfred Stadler and Michael Leitner from EPCOS OHG Deutschlandsberg for contributing the antennas and filters. Thanks also to all current and past members of SPSC who were with me the last three years. All your inspiring discussions about work and non-work issues were very helpful for improving my skills and personality.

Furthermore, I want to thank my parents Maria and Johann Krall for their neverending support during all the years since my birth. My thanks also include my two brothers Helmar and Hannes, with their families. Thanks also to my friends who were backing me up when I needed them, i.e., thanks Thomas, Johannes, René, Markus, Annika, Bettina, Andrea, Herbert, Franz, Lukas, Samantha, Stefan, Birgit, Doris, Christian M., Christian S., Christian S., Christian T., Jürgen, Peter, Marco, Sebastian. Last but not least, I want to thank Trent Reznor for making this awesome music and his continuous efforts against music industry.

Graz, April 2008

Christoph Krall

Contents

1. Introduction	1
1.1. Motivation	3
1.2. Scope of the Work	4
1.3. Outline of the Thesis and Main Contributions	5
2. Subband Modeling of UWB Transceivers	7
2.1. Standardized High-Speed UWB Signals	7
2.2. Modeling in Subbands	10
2.3. Parallel Transmitter Architecture for UWB OFDM Signals	12
2.4. Subband Modeling of the Channel	16
2.4.1. Design of the Filters for Subband Processing	18
2.4.2. Frequency Response Masking Filter Design	19
2.4.3. Mapping the Transfer Function on the Filterbank	21
2.4.4. Synthesizing the UWB Channel	21
2.5. Parallel Receiver Architecture	22
2.6. Simulation Results	25
2.7. Conclusions	28
3. Pulse-Based UWB Communication	33
3.1. Introduction	33
3.2. Flexible Generation of UWB Signals	36
3.2.1. System Model	37
3.2.2. Hardware Implementation	41
3.3. Compensation of Timing Offsets in TIDAC Structures	44
3.3.1. System Model	45
3.3.2. Proposed Compensation Filters	46
3.3.3. Timing Offset Identification	47
3.4. Standardized IEEE 802.15.4a Receiver Architectures	47
3.4.1. Standardized Signaling Scheme	48
3.4.2. Receiver Architectures	49

3.4.3. Receiver Comparison	53
3.5. Conclusions	56
4. Equalization for Nonlinear Receiver Front-Ends	59
4.1. Introduction	59
4.2. Equivalent Nonlinear System Model	61
4.2.1. Volterra Models	62
4.2.2. Simplified Nonlinear System Model	62
4.3. Nonlinear Equalization for Second-Order Volterra Systems	63
4.4. MMSE Volterra Filters	65
4.4.1. First-Order Equalizer	65
4.4.2. Second-Order Equalizer	67
4.4.3. Adaptive Volterra Filters	69
4.4.4. Simulation Results	69
4.5. Conclusions	73
5. Conclusion and Outlook	75
A. UWB Chipsets	79
B. UWB Demonstrator	81
B.1. FPGA Hardware	81
B.2. RF Front-End	82
B.3. UWB Antennas	83
B.3.1. Matching	85
B.3.2. Directivity Measurements	86
B.3.3. Gain Measurements	91
C. Standardized UWB Channels	99
C.1. Statistical Channel Models	99
C.1.1. Description of Different Propagation Effects	99
C.1.2. Statistical Modeling of the Path Loss Exponent	100
C.1.3. Fading	102
C.1.4. General Shape of the Impulse Response	105
C.1.5. Path Interarrival Times	105
C.1.6. Cluster Powers and Cluster Shapes	106
C.2. Parameters of the IEEE 802.15.3a Channel Model	107
C.2.1. The Model	107
C.2.2. Channel Parameters	108
C.3. The IEEE 802.15.4a Channel Model	109
C.3.1. The Model	110
D. Correlation Matrix for the Second-Order Equalizer	115
D.1. Commutation of the Kronecker Product	115
D.2. Correlation Matrix of the Data Terms	115

E. Derivation of the Compensation Filters **119**

- E.1. Two-Periodic Nonuniform Holding Signals 121
 - E.1.1. Solution of the Matrix Equation 121
 - E.1.2. FIR Filter Design Example 122

List of Abbreviations

ADC	Analog-to-Digital Converter
AcR	Autocorrelation Receiver
ALU	Arithmetic Logic Unit
AWGN	Additive White Gaussian Noise
BER	Bit Error Ratio
BPM	Burst Position Modulation
BPSK	Binary-Phase-Shift-Keying
CIR	Channel Impulse Response
CP	Cyclic Prefix
CS	Continuous Spectrum
DAC	Digital-to-Analog Converter
DFT	Discrete Fourier Transform
DS-SS	Direct Sequence Spread Spectrum
DSP	Digital Signal Processing
ECMA	European Computer Manufacturers Association
ED	Energy Detector
FCC	Federal Communication Commission
FD	Frame-Differential
FFT	Fast Fourier Transform
FIR	Finite Impulse Response
FPGA	Field Programmable Gate Array
FRM	Frequency Response Masking
FT	Fourier Transform
GPS	Global Positioning System
HDMI	High-Definition Multimedia Interface

IBI	Inter-Block Interference
ICI	Inter-Carrier Interference
IDFT	Inverse Discrete Fourier Transform
IEEE	Institute of Electrical and Electronics Engineers
IFFT	Inverse Fast Fourier Transform
IIR	Infinite Impulse Response
ISI	Inter-Symbol Interference
ISO	International Standards Organization
LO	Local Oscillator
LOS	Line-of-Sight
LMS	Least Mean Square
LVDS	Low Voltage Differential Signaling
MAC	Medium Access Control of the OSI model
MBER	Minimum Bit Error Ratio
MB-OFDM	Multi-Band Orthogonal Frequency Division Multiplex
ML	Maximum Likelihood
MMSE	Minimum Mean Square Error
MPC	Multi-Path Component
MRC	Maximum Ratio Combining
MUI	Multi-User Interference
NBI	Narrow-Band Interference
NLOS	Non-Line-of-Sight
OFDM	Orthogonal Frequency Division Multiplex
OLA	Overlap-add DFT computation
PAP	Peak-to-Average Power
PSD	Power Spectral Density
PHY	Physical Layer of the OSI model
PPM	Pulse Position Modulation
QAM	Quadrature Amplitude Modulation
QPSK	Quadrature-Phase-Shift-Keying
RF	Radio-Frequency
RFID	Radio-Frequency Identification
RMS	Root Mean Square
RRC	Root Raised Cosine
SER	Symbol Error Ratio
SNR	Signal-to-Noise Ratio
TDMA	Time Division Multiple Access
TG3a	Task Group 3a

TG4a	Task Group 4a
TIDAC	Time-Interleaved Digital-to-Analog Converter
TR	Transmitted-Reference
USB	Universal Serial Bus
UWB	Ultra-Wideband
WLAN	Wireless Local Area Network
WPAN	Wireless Personal Area Network
WUSB	Wireless Universal Serial Bus
ZF	Zero Forcing
ZOH	Zero-Order Hold
ZP	Zero-Padded Prefix

Introduction

In recent years a growing demand on high-speed wireless communication has been recognized. This bandwidth demand is required to achieve cable replacement and high speed wireless personal area network (WPAN) communications applications. A further advantage of the high bandwidth used in broadband systems is high ranging and positioning accuracy. In 2002, the Federal Communications Commission (FCC) released a report and order to allow *unlicensed* operation of services between 3.1 and 10.6 GHz restricting the electromagnetic emission level to a power spectral density (PSD) of -41.25 dBm/MHz [1]. Furthermore, a definition of the term “Ultra Wide-Band (UWB)” has been given in the same document. According to this authority, a UWB signal is defined as a signal which has a -10 dB bandwidth of at least 500 MHz or a fractional bandwidth which is greater than 0.2. The fractional bandwidth is the bandwidth of a system normalized to the center frequency. This milestone in releasing spectrum for unlicensed operation fueled the motivation of many researchers (at industries and at universities) to think of clever ideas to design a system which can operate at such low emission levels. Nonetheless, the communication system has to be robust against noise and interference from other, already existing services in the same spectrum like WLAN, GPS, etc. Usually these systems transmit with much higher power but operate in restricted, licensed (mostly for very high cost) spectral regions provided by national authorities.

To cover the main target applications promised by the distinguished wideband features of UWB technology, two different standardized signaling schemes have been developed. For the first one, the focus was clearly on the cable replacement and short-range high-speed data communication networks, e.g., Wireless USB® 2.0, Wireless FireWire® (IEEE 1394a), Wireless HDMI, etc. To combine all the different perspectives about implementing such a high speed WPAN system, the IEEE formed a standardization task group (IEEE 802.15.3a) which tried to standardize the physical requirements and the medium access control for such a novel communication system. Within this standardization process, many different schemes were submitted to the standardization committee, but finally none of them could get the majority of the votes and the task group failed in its mission. Afterwards one of the proposals (the one with major industry support) was standardized within the European Computer Manufacturers Association (ECMA) and consecutively within the International Organization for Standardization (ISO). Finally, industry has formed the WiMedia alliance which adopted the ECMA/ISO standard. Many chipsets are

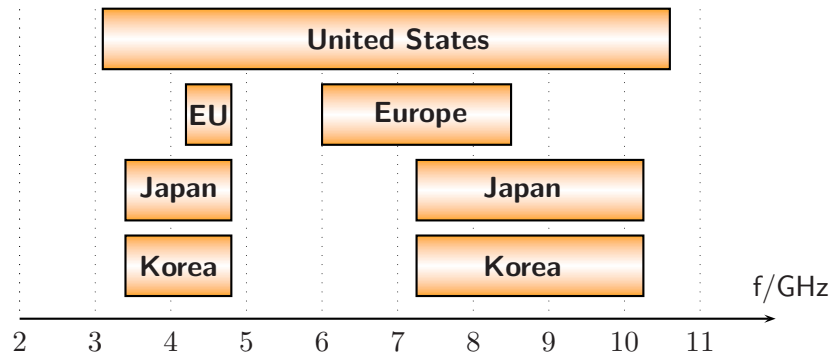


Figure 1.1.: Spectral emission masks for US, Europe, and Asia, lower frequency band emission restricted to low duty-cycle transmission in Europe [1, 2, 3]

available nowadays, implementing this signal generation WiMedia standard based on Orthogonal Frequency Division Multiplexing (OFDM). On the receiver side the whole signal spectrum has to be sampled again at Nyquist rate which is, for such huge bandwidths, consuming a lot of power. Due to the transmit power limitations described above, this high-speed communication is limited to a maximum distance of ten meters. In fact, most of the current implementations achieve distances below 4 m at full data rate [4]. Another disadvantage of the high power consumption is the limitation of battery-powered devices. Due to protocol stack mapping of the wireline USB standard to wireless USB connections (to support backwards compatibility) the effective data rate is limited to app. 40 Mbps which still prevents the breakthrough success of this technology [5].

The second standardized scheme was designed with a completely different focus. However, it generally also offers the possibility for fast data transmission. The original scope was to develop a broadband system which is able to provide an alternative physical layer for low-data-rate WPAN communication. An auxiliary feature of the system is high-precision ranging/positioning (better than one meter accuracy) with very low power consumption [6]. Coming from the sixties, UWB signals have been successfully used in radar applications where short pulses were transmitted and echoes from reflected targets were detected accurately [7]. For that reason many proposals (a total of 26) have been submitted to the standardization task group and were finally merged in 2005. Due to the huge bandwidth used in UWB signals (≥ 500 MHz) the ranging and positioning accuracy is also very high. If we consider a system with a bandwidth of 500 MHz, evaluating the distance in terms of delay estimation of a pulse, we can determine the Cramer-Rao lower bound for a distance estimator as app. 0.02 mm if we assume a Gaussian channel. This very impressive result, which will not be achieved in a realistic system where one has to consider the impact of the wireless propagation channel [8], fuels the motivation to use UWB technology as an alternative to current Radio Frequency Identification (RFID) solutions. For pulse-based systems a standardized communication scheme has been developed and standardized which uses many, closely spaced pulses which are modulating a carrier in phase. To allow for multiple users, these bursts of pulses are randomly placed in a time division multiple access (TDMA) grid. As mentioned before, low complexity and energy efficient implementations should pave the way to the success of this alternative technol-

ogy. This is possible because of the TDMA structure where transceivers can be switched off in long idle periods. On the other hand the receiver structures used to recover the transmitted signals are very simple. They simply try to recover, i.e., determine and store the energy present in a certain frequency band. According to the cumulated energy a decision is made on the transmitted data. However, the propagation channel can severely distort the signals, which is a very challenging problem for a system designer. Even more challenging is the nonlinear behavior of the front-end elements. Interference from services operating in the same spectrum additionally limit the performance of these highly diverse systems.

Recently, the European Union also released a recommendation for the emitted power spectral density (PSD) which has to be implemented individually by the member states [2]. The European view on the unlicensed and free operation of wideband communication systems is more conservative than the one in the US. Potential victim services like WLAN and GPS are explicitly bypassed and the available frequency range was split in two parts. Fig. 1.1 shows the regulation for the US, the proposed regulation masks for the EU, and the regulations for important markets in Asia. It is clearly seen that a device operating worldwide is very restricted in using the full spectral resources.

1.1. Motivation

As mentioned before, the novel Ultra Wide-Band technology also brings a lot of challenges across all different disciplines of electrical engineering. First of all, the circuit design of such systems touches the current limits of the technology for baseband signal processing and for RF circuitry used for carrier generation, mixing, etc. Furthermore, broadband antennas and matching networks for flexible and reconfigurable front-ends have to be designed. Last but not least, many new/modified network protocols have to be found and efficiently implemented to provide reliable and well performing devices for the specific scenarios. The main motivation for the industrial partner supporting this thesis was to find implementation strategies for a realtime channel simulation environment built with state of the art FPGA and DSP hardware. However, the UWB technology still requires more computational power than available on today's hardware.

Keeping these hardware limitations in mind, it is not a trivial task to generate broadband signals in a UWB transmitter because of their huge bandwidth to be processed. Restricting our considerations not only to standardized UWB signals, the generation of pulse-based wideband signals consists only of a few components which appears easy, but requires difficult timing circuitry to generate pulses at the desired positions in time. However, such a simple circuitry is also not the first choice when designing a universal hardware simulator which supports different waveforms. Furthermore, one standardized UWB system for high-speed wireless personal area networks (WPAN) is employing a broadband OFDM signal to transmit data. Implementing this signal generation on FPGA hardware is indeed not easy considering the bandwidth constraints inherently present on the simulation boards. If a parallelization or distribution of the computational complexity can be found, they can be implemented without major changes in the currently available hardware. Furthermore, if this parallelization can be realized on conventional digital signal processing (DSP) hardware, the same results can help chip designers to find more efficient chips with

relaxed conditions for the individual processing units.

Due to the huge bandwidth, the wireless propagation channel contains severe multipath which is complicating (and simplifying at the same time) the receiver design. Because the energy of the transmitted signal is spread in time one can think of collecting this energy from each multipath component (MPC) and coherently combine this energy resulting in an optimal receiver. By doing this, the energy contained in the MPCs is collected like the leaves with a garden rake, providing the name for this receiver architectures, i.e., Rake receivers. However, the implementation complexity of such a Rake receiver is very huge considering that an UWB channel consists of hundreds of MPCs, each requiring a correlator for correct signal reception. Current implementations restrict the number of paths to app. 10 which gives a tradeoff between implementation complexity and performance for this suboptimal receiver. Furthermore, other sub-optimal receiver structures have been proposed already during the years of research in the area. One main drawback of these architectures is that they employ nonlinearities in their analog front-ends resulting in more complex processing in the back-end to recover the data symbols.

All these current implementation issues necessitate research in various areas of the field of electrical engineering. Some of these are adressed in this thesis. However, the hardware limits due to the given architecture are considered as well which will become clear throughout the thesis.

1.2. Scope of the Work

Within this work, current implementation challenges in terms of signal processing with currently available DSP hardware used for UWB devices are investigated. This means that structures have been investigated to process the enormous bandwidth of UWB signals on transmitter and receiver side. However, one main difference to conventional narrowband systems lies in the difference of the mobile radio channel which is not flat fading anymore. For that reason a more complex model for channel simulation has to be used which exceeds the capabilities of currently available DSP hardware. Thus, ways of distributing the computational requirements and computational complexity on multiple systems have to be investigated and are shown in this thesis.

Not only the implementation of the channel simulator is a complicated task when moving to higher bandwidths. Also the signal generation and receiver architectures are required to process the broadband signals. Thus, a transmitter and receiver architecture is presented in this thesis which overcomes this bandwidth limitation. Furthermore, a technique for arbitrary signal generation of very wideband signals is presented in the thesis. However, in a first step, the computations for this system are studied for the error free case. Afterwards hardware mismatches have been introduced and a compensation structure for these mismatches is presented.

For the previously described nonlinear receiver front-ends, appropriate modeling and a theoretical bound, for the processing which is done in the back-end (digital domain) of the receiver is presented. A framework for nonlinear fading memory systems is presented and one possible strategy to combat the nonlinear distortion effects caused by the nonlinearity inherently present in the analogue front-end. Furthermore, first steps of implementing UWB systems for demonstrating the algorithms and methods evaluated by

means of simulations and measurements.

1.3. Outline of the Thesis and Main Contributions

This thesis is organized as follows: Several sections of this thesis have been published at international conferences and in international journals. In this short summary, the according publications are thus mentioned in the context of the respective chapters.

In chapter 2 the parallelization of a UWB communication channel in the frequency domain is presented. Furthermore, a novel signal generation approach is shown, which demonstrates the parallelization for the generation of one standardized OFDM symbol for the WiMedia standard for WPAN applications. Furthermore, a subband receiver architecture is presented and the performance is compared to conventionally used receivers, i.e., receivers able to process the whole bandwidth.

- Christoph Krall and Klaus Witrisal, *Parallel OFDM Signal Generation for UWB Systems*, in Proceedings of the IEEE International Conference on Ultra Wideband (ICUWB2006), Waltham, MA, September 2006, pp. 243-247. [9]

In chapter 3 methods for the implementation of a pulse-based UWB communication system are presented. For a flexible simulation environment a method for the generation of wideband pulses is presented. For that reason multiple Digital-to-Analog Converters (DACs) are used. Furthermore, a method for the compensation of mismatches in a converter array is presented in this chapter. Finally, a novel receiver architecture for the standardized scheme is presented and compared to other possible receiver candidates for the standardized scheme.

- Christoph Krall, Christian Vogel, and Klaus Witrisal, *Time-Interleaved Digital-to-Analog Converters for UWB Signal Generation*, in Proceedings of the IEEE International Conference on Ultra-Wideband 2007 (ICUWB2007), Singapore, Singapore, 24-26 September 2007. [10]
- Christian Vogel and Christoph Krall, *Compensation of Distortions Due to Periodic Nonuniform Holding Signals*, submitted to IEEE 6th Symposium on Communication Systems, Networks and Digital Signal Processing (CSNDSP), Graz, Austria, July 2008.

In chapter 4 a framework for modeling a sub-optimal nonlinear receiver front-end is presented. However, the presented scheme is a non-standardized one. Anyhow, the performance in terms of Bit Error Ratio (BER) [11], robustness to Narrow-Band Interference (NBI) [12] and Multi-User Interference (MUI) [13], and robustness to the effects of the channel (harsh environments) is promising and thus the system is investigated. It is shown that the receiver output depends nonlinearly on the transmitted data symbols and nonlinear techniques for an equalization of front-ends have to be used to combat the effects of the nonlinear receiver.

- Christoph Krall, Klaus Witrisal, Heinz Koepl, Geert Leus and Marco Pausini, *Nonlinear Equalization for Frame-Differential IR-UWB Receivers*, in Proceedings of the IEEE International Conference on Ultra-Wideband 2005 (ICU 2005), Zurich, Switzerland, 5-8 September 2005, pp. 576-581. [14]

Chapter 1. Introduction

- Christoph Krall, Klaus Witrisal, Geert Leus and Heinz Koepl, *Nonlinear Equalization for Second-Order Volterra Systems*, submitted to IEEE Transactions on Signal Processing.

In chapter 5 conclusions about the presented methods are summarized. The chapters are supported with several appendices, which provide detailed equations, measurement results and supporting information to the topics covered in the thesis chapters.

Subband Modeling of UWB Transceivers

In this chapter the standardized high-speed, WPAN UWB systems used as cable replacement is introduced. An implementation on a parallel architecture is proposed and analyzed [15]. The application of this idea is two-fold. First of all, a new parallel transceiver architecture is found. Secondly, if the simulation of a broad range of environments is desired to be computed on hardware for transceiver prototyping, the implementation of a channel impulse response on digital signal processing (DSP) hardware is necessary. For that reason, efficient ways of mapping the broadband frequency response of a UWB channel onto a parallel architecture of FPGA/DSP boards is discussed. Additionally, an analog signal conditioning has to be done to not violate the sampling theorem. For the transceiver and the wireless propagation channel a hybrid filterbank approach is proposed to be able to process parts of the huge signal bandwidth on a parallel DSP platform. If sufficient signal separation for processing on multiple computing units can be achieved, each unit can be optimized separately and computational costs can be saved for each unit. Furthermore, to extend the system to be able to generate a standardized UWB signals, all the signal generation units have to be used in parallel. This can be done in a very efficient way considering a parallelization of the essential signal generation operation, the inverse fast Fourier transform (IFFT). Additionally, a parallel receiver implementation is discussed in the last section of this chapter¹.

2.1. Standardized High-Speed UWB Signals

When the FCC authorized unlicensed transmission in the 3.1 - 10.6 GHz frequency band in 2002, the IEEE was forming a task group to specify a standardized communication system for wireless personal area networks (WPANs), capable of transmitting at speeds up to 480 Mbps data rate. This task group was assigned to the WPAN activities in the IEEE 802.15 standardization body and was called Task Group 3a (TG3a), looking for an alternative physical layer for WPANs. Conventionally, such a task group has several sub-groups defining different items for the upcoming standard like a model for the wireless broadband channel for different scenarios, signaling, etc. For the wireless channel,

¹The section about the parallel signal generation for OFDM UWB signals and the respective simulation results has been published by the author on an international conference [9].

measurements have been used to characterize a fully stochastic channel model which can be used for the different specified scenarios. This channel model is summarized in Appendix C. It is based on the measurement campaigns conducted in 2002 and 2003 (see [16] and references therein). Due to the problem that the industry was pushing the new technology to get a standardized model as an input for the system design, the model is very general and partly inaccurate. These channel models have been refined in another task group (TG4a) where more physical effects have been considered and modeled [17].

For standardized signaling, many proposals have been submitted to the standardization task group. However, two major proposals have been selected to get a majority vote on, and to get one or both of them standardized. The first one was supported widely by industry and has been submitted by a group of researchers from Texas Instruments [18] in 2004. This proposal describes a multiband orthogonal frequency division multiplexed (OFDM) signal with a bandwidth of 528 MHz, which is hopped very fast in frequency. The second proposal was a broadband direct sequence spread spectrum (DS-SS) signal which was also occupying a bandwidth larger than 500 MHz [19]. However, none of the two proposals could get the majority of the votes and finally, the task group failed in standardizing a signaling scheme. For that reason, the first proposal (which had a lot of industrial supporters) was submitted to the European Computer Manufacturing Association (ECMA) to be standardized there. There it was standardized in Dec. 2005 and a final standardization document was released [15]. Consecutively, a standardization has been done of the same scheme within the International Standards Organization (ISO) and was published under the number ISO 26907 [20]. By standardizing this scheme, industry had a worldwide standard for implementing high-speed UWB systems which pushed many companies to have products on the market. Nowadays, the first solutions are around from several manufacturers providing chipsets up to 480 Mbps realizing a wireless USB connection (see App. A). However, a breakthrough of this technology is still lagging behind because of the backwards compatibility of the system to wireline USB connections, limiting the effective data rate [5]. All supporters and partners of this standardization have been gathered in the WiMedia Organization (www.wimedia.org) which also hosts the current version of the standard and makes minor refinements [21].

WiMedia Standard As already mentioned, finally the WiMedia standard for high-speed data communication is used nowadays to implement high-speed UWB systems. For that reason its general signal structure is discussed here and a proposal for a parallel system implementation is presented in later sections. For the 7.5 GHz bandwidth available in the US, the standardized system uses 14 partitions for transmitting a fast frequency-hopped-signal. These frequency channels are summarized in Table 2.1 and visualized in Fig. 2.1, respectively. It is furthermore seen that the 14 channels are separated into 5 band groups, each occupying either 1 GHz or 1.5 GHz of bandwidth. So called “Mode 1” devices are supposed to hop the first three channels, i.e., all channels in band group 1. If we reconsider the frequency ranges released by the regulation authorities in different parts of the world (*cf.* Fig. 1.1) not many of these channels remain if a worldwide device is required.

The currently standardized signal is, as already mentioned, a multiband OFDM (MB-OFDM) signal. The OFDM signal consists of 128 carriers which are modulated with QPSK data symbols. The bandwidth of one OFDM symbol is specified as 528 MHz. A possible hopping sequence and the timings for one UWB OFDM symbol are shown in Fig. 2.2. To

2.1. Standardized High-Speed UWB Signals

Band Group	Band ID	Lower frequency	Center frequency	Upper frequency
1	1	3168 MHz	3432 MHz	3696 MHz
	2	3696 MHz	3960 MHz	4224 MHz
	3	4224 MHz	4488 MHz	4752 MHz
2	4	4752 MHz	5016 MHz	5280 MHz
	5	5280 MHz	5544 MHz	5808 MHz
	6	5808 MHz	6072 MHz	6336 MHz
3	7	6336 MHz	6600 MHz	6864 MHz
	8	6864 MHz	7128 MHz	7392 MHz
	9	7392 MHz	7656 MHz	7920 MHz
4	10	7920 MHz	8184 MHz	8448 MHz
	11	8448 MHz	8712 MHz	8976 MHz
	12	8976 MHz	9240 MHz	9504 MHz
5	13	9504 MHz	9768 MHz	10032 MHz
	14	10032 MHz	10296 MHz	10560 MHz

Table 2.1.: Channel matrix for ECMA-368 standardized UWB communication

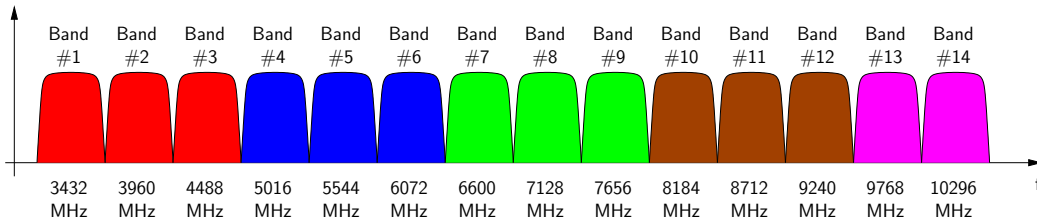


Figure 2.1.: Bandplan for the ECMA-368 standard, with individually colored band groups

make the signal robust to the wireless propagation channel, the OFDM symbol has to be extended by a guard interval (GI) [22, 23]. An additional time gap has to be added in this signaling scheme to allow RF carrier switching.

In Fig. 2.3 the 128 carriers of one OFDM symbol are shown. Generally, the subcarrier which is at the DC value in the complex baseband is modulated by zero to avoid carrier feed through to the output of the RF front-end. Similarly, the carriers at the band edges are nulled out to be able to design an analog front-end filter for the suppression of the mirror images when generating the signal with a DAC. However, nulling just 3 subcarriers is not giving much space between desired and undesired spectral components and might certainly increase the complexity of the analog front-end filter to achieve good signal reconstruction. This problem is again studied in Chapter 3 and a solution to use low-complexity analog filters is introduced and presented. Additionally, some redundancy at the band edges is introduced to combat the effects of the wireless channel. To perform channel estimation and equalization of the received signal, pilot carriers are added in regular distances (*cf.* all the carriers labeled with P_x in Fig. 2.3) which have known data modulation. Due to the known data symbols at the corresponding carriers, many different equalization approaches can be implemented to achieve robustness against the effects of the channel [24].

As mentioned before, the system uses an MB-OFDM signal to transmit data with a

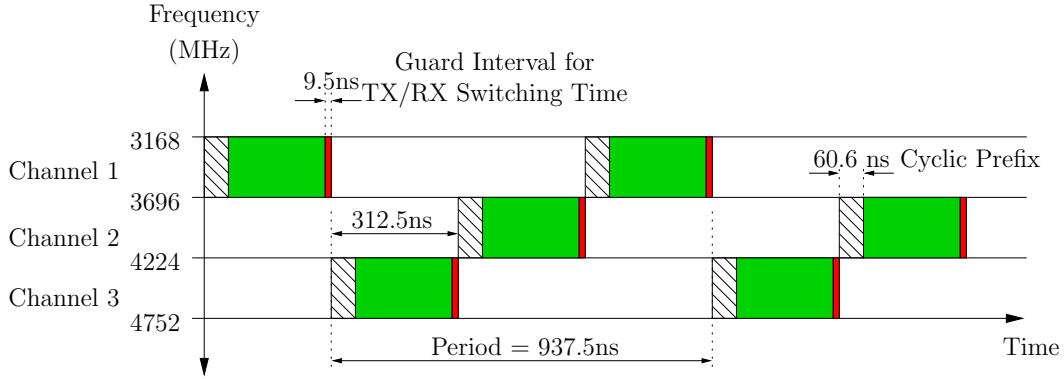


Figure 2.2.: Proposed OFDM Signal for high speed data communication

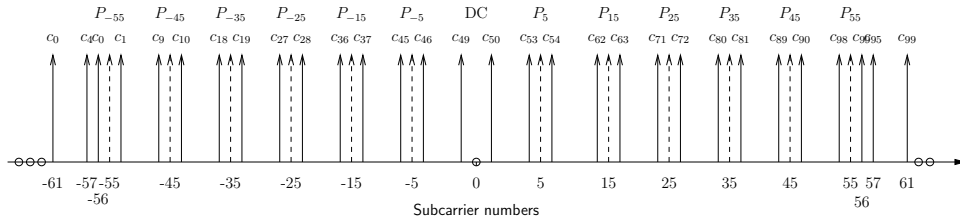


Figure 2.3.: Arrangement of the subcarriers in each subband

signal bandwidth of 528 MHz. This means that for the complex I and Q signal a signal bandwidth of 264 MHz has to be processed. This is generally a non-trivial task on currently available hardware (state-of-the-art FPGAs or DSPs). To meet realtime conditions for signal processing on reconfigurable hardware is tough because it is slower than an implementation on a single-chip solution. Furthermore, if a convolution has to be computed, the maximum (allowable) length of the filter also strongly depends on the number of gates contained in the FPGA (used for multiplication and addition of the input signal with the filter coefficients) or the number of arithmetic logic units (ALUs) in a DSP. We will see that an impulse response of a UWB wireless channel can be very long, thus showing a lot of frequency selectivity. Since the number of taps is limited quite drastically for an FPGA implementation, alternative ways of implementation have to be found. If the signal bandwidth to be processed is below a certain technological limit (here 80 MHz), already optimized structures for the used hardware components can be re-used and a very efficient (in terms of power consumption, technology, ...) architecture can be used to implement the transceivers.

2.2. Modeling in Subbands

As we have already motivated in the beginning, the complexity to compute either the transmitter, receiver, or channel in an FPGA or DSP is too high considering the available technology. For that reason a parallel structure as depicted in Fig. 2.4 is proposed. This parallel architecture separates the input signal $s(t)$, i.e., the UWB MB-OFDM signal, after correct downconversion into subbands. Each of these subbands is then sampled

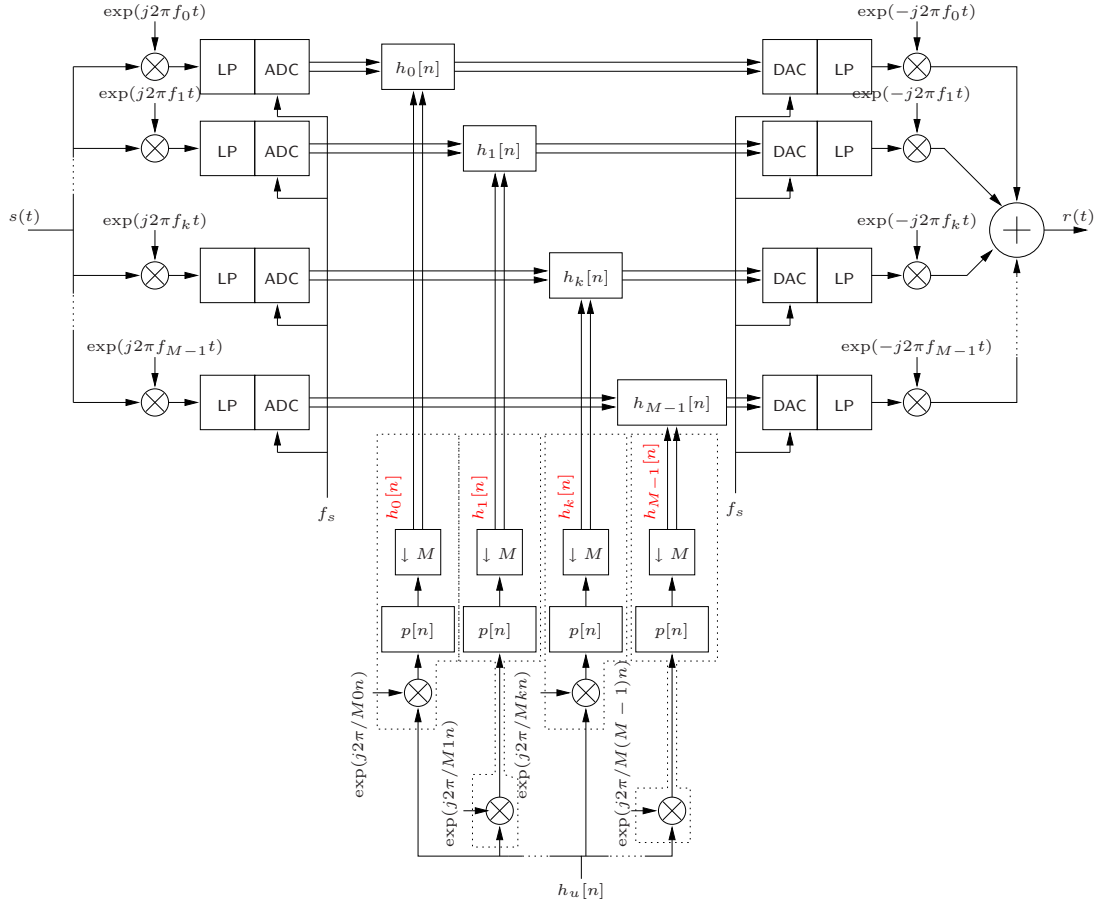


Figure 2.4.: Subband implementation of the channel impulse response

by an Analog-to-Digital Converter (ADC) to perform the computational steps for the convolution with the channel impulse response. At the right hand side of Fig. 2.4 the inverse steps of this signal separation is performed. To represent the convolution of the signals with the channel impulse response, also the wireless propagation channel has to be represented in subbands. This is achieved by a similar mixer and filter stage shown in the lower part of Fig. 2.4. The individual subband filters are computed from a UWB channel impulse response (CIR) $h_u[n]$ defined in the standardization document [4, 16, 17]. This channel impulse response in the subbands is obtained from a specially prepared impulse response and separated into subbands with the prototype filters $p[n]$. The design of these filters and the subband filtering is described in more detail in Section 2.4. After convolution with the subband impulse responses the received signal $r(t)$ is obtained at the output of the system.

Additionally to this parallel mapping of a channel, the signal generation and the receiver operation in the complex baseband are implemented in a parallel way. In the next sections, firstly the parallel transmitter is introduced first. Secondly, the architecture shown in Fig. 2.4 is analyzed analytically and a synthesized CIR is shown for the described parallelization procedure. Finally, the parallel receiver architecture is presented. All the presented architectures are then compared in performance with computer simulations.

2.3. Parallel Transmitter Architecture for UWB OFDM Signals

Since the direct generation of such wideband OFDM signals on FPGA hardware is too complex, a parallel transmitter architecture to generate UWB OFDM signals has been proposed. The modulation in an OFDM signal is done by an inverse discrete Fourier transform (IDFT) or its fast implementation, the inverse fast Fourier transform (IFFT) [25, 26]. This means that for standardized UWB systems [15], each 312.5 ns a new IFFT block has to be computed. This is feasible on a single chip implementation. However, on a DSP or FPGA the implementation complexity would be far too high to achieve a realtime solution. For that reason we propose a parallel approach to accomplish the signal generation with conventional hardware, i.e., state-of-the-art DSPs or FPGAs. This means that the IFFT can be broken up into smaller IFFTs which can be computed at lower sampling rate.

Some related work can be found in the open literature. In [27] a partitioning scheme was used to introduce transmitter diversity. Another use of partitioning the input signal into equisized blocks of data is to reduce the peak-to-average power (PAP) and avoid the effects of nonlinearities in power amplifiers [28, 29]. Thus, for PAP reduction a different signal is generated for transmission, which has less dynamic. The advantage of the proposed approach is, that for each subblock a smaller IDFT/IFFT has to be computed but the overall signal has similar, or ideally the same, characteristics as a conventionally generated one. A similar approach has been sketched already in [30], but there no implementation aspects have been considered.

System Model

The carrier spacing Δ_f of the 128-carrier OFDM signal is determined as

$$\Delta_f = \frac{1}{T_{FFT}} \quad (2.1)$$

where T_{FFT} is the effective duration of the OFDM symbol which is related to the number of used carriers N by $N = B/\Delta_f$, where B is the bandwidth of the signal. For the proposed system the carrier spacing according to (2.1) is obtained as 4.125 MHz. This is one essential parameter of the system which has to be considered when a parallel signal generation is considered.

OFDM Signal

If the OFDM signal is generated at full bandwidth, the time-domain signal $x[n]$ is given by the IDFT (IFFT) as [31]

$$x[n] = \frac{1}{\sqrt{N}} \sum_{k=0}^{N-1} d[k] W_N^{-kn}, \quad (2.2)$$

where $d[k]$ are the data symbols in the frequency domain and W_N is the set of complex exponentials given as

$$W_N = e^{-j(2\pi/N)}. \quad (2.3)$$

2.3. Parallel Transmitter Architecture for UWB OFDM Signals

If we arrange the N samples of the data signal into a vector \mathbf{d} , similarly, the N -point FFT can be expressed as a matrix \mathbf{F}_N where the (n, k) th entry of the matrix is given as $\exp\{j2\pi nk/N\}/\sqrt{N}$. Thus, the N -point IFFT is determined as $\mathbf{F}_N^{-1} = \mathbf{F}_N^H$, where $(\cdot)^H$ denotes conjugate transposition.

With the introduced notation the time-domain signal is expressed as

$$\mathbf{x} = \mathbf{F}_N^H \mathbf{d}. \quad (2.4)$$

If the data is arranged in V disjoint subblocks \mathbf{d}_v where $v = 1 \dots V$, the IDFT can be expressed as

$$\mathbf{x} = \sum_{v=1}^V \mathbf{F}_N^H \mathbf{d}_v. \quad (2.5)$$

The vector \mathbf{d}_v is an $N \times 1$ element long vector of data symbols where only $L = N/V$ symbols are non-zero, i.e.,

$$\mathbf{d}_v = \begin{bmatrix} \mathbf{0}_{(v-1)L \times 1} \\ d[(v-1)L] \\ \vdots \\ d[vL-1] \\ \mathbf{0}_{(N-vL) \times 1} \end{bmatrix}_{N \times 1}. \quad (2.6)$$

Similarly, the data symbols in \mathbf{d}_v can be defined in the “baseband”. Then each signal has to be multiplied with complex exponentials $\mathbf{w}_N^{(i)}$, given by

$$\mathbf{w}_N^{(i)} = \begin{bmatrix} e^{j0} \\ e^{j2\pi i/N} \\ \vdots \\ e^{j2(N-1)\pi i/N} \end{bmatrix}_{N \times 1} \quad (2.7)$$

where $i = (2v-1)L/2$. This leads to new data vectors given as

$$\tilde{\mathbf{d}}_v = \begin{bmatrix} d[(v-1)L + L/2] \\ \vdots \\ d[vL-1] \\ \mathbf{0}_{N-vL \times 1} \\ d[(v-1)L] \\ \vdots \\ d[(v-1)L + L/2 - 1] \end{bmatrix}_{N \times 1}, \quad (2.8)$$

and the IFFT on the data symbols can be expressed as

$$\mathbf{x} = \sum_{v=1}^V \text{diag}\{\mathbf{w}_N^{(i)}\} \mathbf{F}_N^H \tilde{\mathbf{d}}_v. \quad (2.9)$$

The $\text{diag}\{\}$ operator distributes the elements of a vector on the main diagonal of a square matrix. For the sake of clarity the system model of (2.9) is depicted in Fig. 2.5. The input data is partitioned into V blocks $\tilde{\mathbf{d}}_v$ and for each block an IFFT/IDFT is computed.

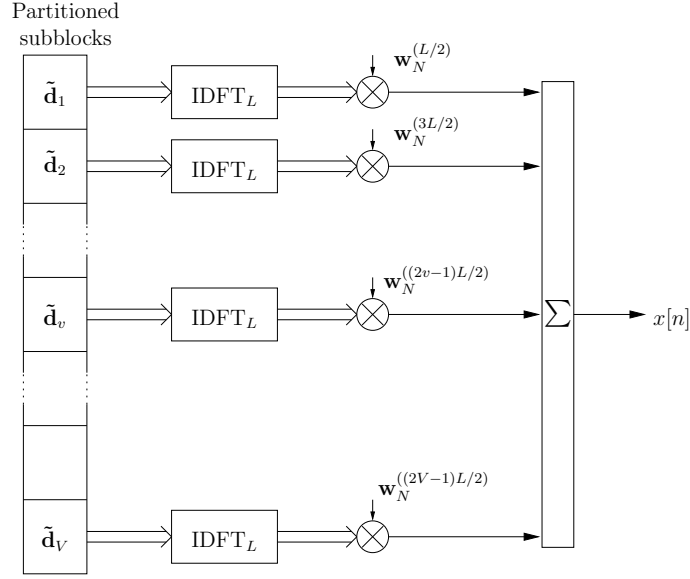


Figure 2.5.: Proposed parallel computation of an OFDM signal.

The goal is to achieve parallel generation of the OFDM signal which is obtained by computing V smaller IFFTs. Theoretically, the size of the IFFT in each subband can be just L points but in this case we would need infinitely steep filters to achieve separation of the bands. To allow for practical filters, some oversampling is introduced, extending the IDFT blocksize to $L' > L$. The additionally introduced carriers ($L' - L$) are not modulated, i.e. they are set to zero. With respect to (2.8) we define a new data vector $\tilde{\mathbf{d}}_v^{(L')}$ as

$$\tilde{\mathbf{d}}_v^{(L')} = \begin{bmatrix} d[(v-1)L + L/2] \\ \vdots \\ d[vL - 1] \\ \mathbf{0}_{L'-L \times 1} \\ d[(v-1)L] \\ \vdots \\ d[(v-1)L + L/2 - 1] \end{bmatrix}_{L' \times 1}. \quad (2.10)$$

Each of the subband signals is now computed separately. After a parallel/serial conversion the signal is converted into the analog domain by Digital-to-Analog Converters (DACs). The transfer-function of the DACs is assumed to be a lowpass transfer function modeled by an impulse response $h_{DAC}[n]$. Thus an approximated signal vector $\hat{\mathbf{x}}$ can be computed as

$$\hat{\mathbf{x}} = \sum_{v=1}^V \text{diag}\{\mathbf{w}_N^{(i)}\} \mathbf{H}_{DAC} \mathbf{F}_{L'}^H \tilde{\mathbf{d}}_v^{(L')} \quad (2.11)$$

where \mathbf{H}_{DAC} is a Toeplitz matrix representing the linear convolution of the OFDM subband signal with the impulse response of the DAC interpolation filter. The upsampling and cutting away of the transients is taken care of in (2.11), such that $\hat{\mathbf{x}}$ is length N .

2.3. Parallel Transmitter Architecture for UWB OFDM Signals

In the following the quality loss due to subband signal generation is expressed analytically. For that reason one has to figure out which effects are still visible after receiving and demodulating the signal in the receiver. Thus, an error vector \mathbf{e} is defined for each subcarrier as

$$\mathbf{e} = \mathbf{d} - \hat{\mathbf{d}} \quad (2.12)$$

where \mathbf{d} is the used data vector and $\hat{\mathbf{d}}$ is the demodulated data vector from the subband-generated signal, respectively. The receiver has to perform an FFT on the block of received data symbols, i.e. $\hat{\mathbf{d}}$ can be expressed as

$$\hat{\mathbf{d}} = \mathbf{F}_N \hat{\mathbf{x}}, \quad (2.13)$$

where we have assumed an ideal channel. Similarly to the steps described for the subband decomposition, the signal $\hat{\mathbf{x}}$ can be expressed as

$$\hat{\mathbf{x}} = \sum_{v=1}^V \text{diag}\{\mathbf{w}_N^{(i)}\} \mathbf{H}_{DAC} \mathbf{F}_{L'}^H \mathbf{S}_v^{(L')} \mathbf{d}, \quad (2.14)$$

where $\mathbf{S}_v^{(L')}$ is a selection and truncation matrix applied on the data vector \mathbf{d} to perform the steps described in (2.6), (2.8), and (2.10). Thus, the error equation can be simplified to

$$\mathbf{e} = \underbrace{\left(\mathbf{I} - \mathbf{F}_N \sum_{v=1}^V \text{diag}\{\mathbf{w}_N^{(i)}\} \mathbf{H}_{DAC} \mathbf{F}_{L'}^H \mathbf{S}_v^{(L')} \right)}_{\mathbf{\Lambda}} \mathbf{d}, \quad (2.15)$$

where \mathbf{I} represents an $N \times N$ identity matrix and $\mathbf{\Lambda}$ is a matrix representing the deterministic distortion errors and the Inter-Carrier Interference (ICI), respectively. The covariance of the error is then given as

$$\mathbf{E}\{\mathbf{e}\mathbf{e}^H\} = \mathbf{E}\{\mathbf{\Lambda}\mathbf{d}\mathbf{d}^H\mathbf{\Lambda}^H\} = \mathbf{\Lambda}\mathbf{\Lambda}^H, \quad (2.16)$$

where it is assumed that the autocorrelation matrix of the data symbols is an identity matrix which holds for the current discussion because of i.i.d. unit-energy data symbols. The diagonal elements of $\mathbf{E}\{\mathbf{e}\mathbf{e}^H\}$ represent the Mean Squared Error (MSE) due to the subband decomposition and the reconstruction filters in the DACs, for each subcarrier. The main diagonal elements of $\mathbf{\Lambda}$ represent a deterministic error which potentially can be compensated in the receiver by a channel estimation algorithm. The off-diagonal elements of $\mathbf{\Lambda}$ stand for the deterministic ICI from one carrier to another.

Cyclic Prefix - Zero Padded Prefix

Generally, an OFDM signal computed by the IFFT has to be extended to be resistant against the multipath propagation channel [16]. This is usually done by a cyclic extension or cyclic prefix (CP) of the signal. The CP is realized by copying C' computed symbols from the end of the time-domain signal to the beginning of the time-domain signal. One recently proposed approach considers substituting a cyclic repetition of the OFDM signal with a sequence of zeros, i.e., zero-padding (ZP) [32]. It has similar computational

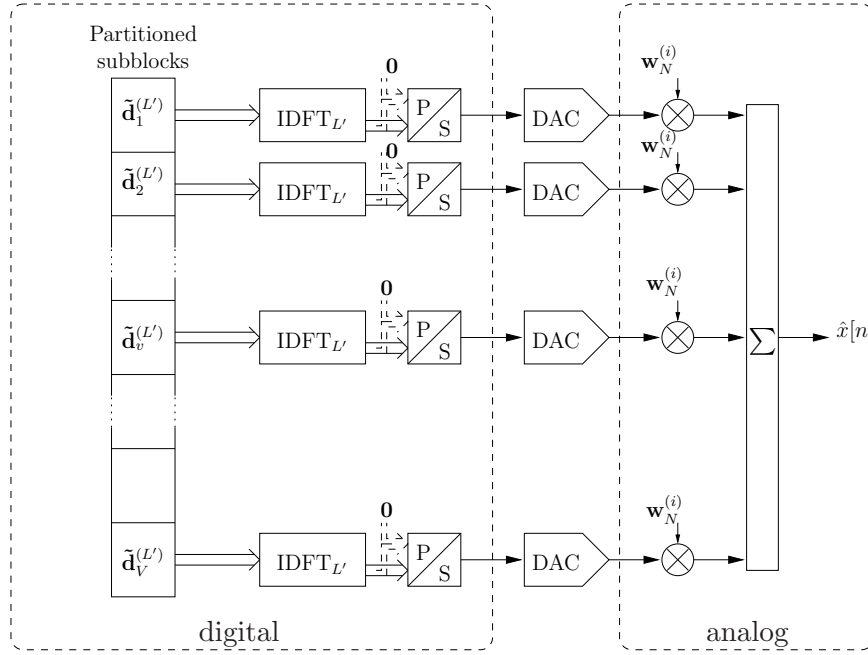


Figure 2.6.: Inserting cyclic prefix/zero-padded prefix for ODFM signal generation

complexity and spectral efficiency as the CP OFDM signal but requires a different algorithm for correct signal demodulation in the receiver. Due to the zeros at the beginning of each symbol, the receiver has to use an overlap-add method (OLA) [31] to correctly demodulate the data symbols. However, by the zero-padded extension the introduced Inter-Symbol Interference (ISI) is eliminated. A resulting channel matrix is then always guaranteed to be invertible, which enables perfect detectability in the absence of noise.

In the proposed scheme the insertion of the CP/ZP can be done very nicely for each subband separately. This is presented in Fig. 2.6. After partitioning the input data into subblocks and computing an IDFT separately, the cyclic extension or zero padding is inserted. The signal is then converted from its parallel set of samples into a serial sequence and is fed into a Digital-to-Analog Converter (DAC). To achieve shifting of the subband to the correct position, complex modulators are used. The proposed transmitter architecture is compared to a conventional transmitter which can handle the huge signal bandwidth. The comparison has been done on a carrier-by-carrier basis by demonstrating the additional error on each subcarrier in the signal spectrum. Furthermore, the signal has been fed into a UWB OFDM receiver and the performance of the parallel architecture has been compared to a conventional signal generator in terms of symbol-error ratio (SER). The simulation environment and the obtained results are discussed in Section 2.6.

2.4. Subband Modeling of the Channel

For the implementation of the response of a wideband propagation channel (*cf.* Fig. 2.4), it is very important to have a bandlimited channel response to be able to separate the wideband signal into subbands. Thus, this subsection's focus is on general aspects of

2.4. Subband Modeling of the Channel

modeling a target transfer function with a filter bank consisting of M filters. Each of the filters in the filter bank should model the transfer characteristics of the UWB channel for $1/M$ -th of frequency range. Generally, such a filter bank is constructed by generating a prototype filter which has lowpass characteristics within the band of interest. Please note that it would also be possible to design bandpass filters but this increases complexity. The transfer function can be arbitrarily specified according to the sampling frequency and the transfer characteristics (passband attenuation, stopband attenuation, ripple in passband, ripple in stopband, ...). However, it is very important to keep the length of the filter rather low, i.e. to keep the implementation complexity low, which is in general proportional to the filter length.

For the modeling of the wireless propagation channel many measurement campaigns have been used to get reliable results for the channel parameters (see [4] and references therein). Four different channel models have been selected and standardized with a set of channel parameters (see App. C for more information of the model). The channel model defines a channel impulse response in a statistical sense, i.e., the expected value of the channel filter taps of the CIR for a specified scenario. Generally, a CIR $h_{ct}(t)$ can be written as a sum of attenuated and time-shifted delta pulses [33, 34, 35], i.e.,

$$h_{ct}(t) = \sum_{i=0}^{N-1} a_i \delta(t - \tau_i), \quad (2.17)$$

where $\{a_i\}$ is the set of path amplitudes and $\{\tau_i\}$ is the set of path delays, respectively. Similarly, the frequency response of the continuous-time impulse response is given by the Fourier transform, i.e.,

$$\mathcal{F}\{h_{ct}(t)\} = H_{ct}(f) = \int_{-\infty}^{\infty} h_{ct}(t) \exp(-j2\pi ft) dt. \quad (2.18)$$

Consecutively, incorporating (2.17) into the frequency-domain representation in (2.18) gives a channel frequency response

$$H_w(f) = \sum_{i=0}^{N-1} a_i \exp(-j2\pi f\tau_i). \quad (2.19)$$

Usually this wideband channel is very frequency selective, and for a model of the channel many coefficients of an equivalent filter response are needed. The bandwidth of the channel is limited to 528 MHz. Furthermore, in the proposed approach (*cf.* Fig. 2.4) the individual processing units are not capable to model the whole frequency range at once because this would need too many taps of an equivalent complex baseband filter [36].

To restrict the bandwidth of the one region related to the interesting band, it has to be windowed from the overall frequency response. Thus the Fourier transform seen in (2.19) is restricted to frequencies in between a lower frequency f_l and a higher frequency f_h .

$$H_{ct}(f) = W(f - f_c) \sum_{i=0}^{N-1} a_i \exp(-j2\pi f\tau_i). \quad (2.20)$$

By applying this window function in the frequency domain, a bandlimitation of the broadband frequency response to a certain bandwidth $B = f_h - f_l$ is achieved because the

window function is zero outside this frequency range. The center frequency f_c can be directly used from the standardized channel definition seen in Table 2.1. For the window functions $W(f)$, one can use well known windows as Tukey or cosine roll-off windows to achieve smooth results in the time-domain. Furthermore, the window function has to be flat within the interesting signal bandwidth, i.e., between f_l and f_h , and should suppress all frequencies outside this band. For the detailed definition of the window $W(f)$ and its exact properties the interested reader is referred to [37]. By restricting the signal bandwidth to the bandwidth of the window, an implicit down-conversion to a complex baseband representation is achieved.

Until now, all processing steps are still in continuous-time domain. To apply DSP the frequency response of the channel impulse response has to be sampled in the frequency domain to obtain a discrete representation. The implicit shifting (modulation) down to complex baseband, denoted in (2.20), is also achieved with a shifting of the frequency band with a complex exponential with frequency f_c . Thus, an equivalent baseband representation is given as,

$$H_u(f) = H_{ct}(f + f_c) = W(f) \sum_{i=0}^{N-1} a_i \exp(-j2\pi f\tau_i) \exp(-j2\pi f_c\tau_i). \quad (2.21)$$

To obtain a discrete-frequency representation of the windowed, down-converted frequency response, the continuous frequency-domain vector $H_u(f)$ has to be sampled. The vector of samples is given as

$$H_u[k] = H_u(kF) \quad (2.22)$$

where F denotes the spacing between points in the frequency domain, i.e., sampling in equidistant frequency increments. A discrete-time representation of the frequency response obtained from the standardized channel model is then obtained by performing the IDFT of the frequency-domain signal [31].

All the processing steps, which have to be done to obtain an impulse response of a wireless broadband channel are summarized in Fig. 2.7. First of all, the continuous-time impulse response defined in the standardized model has to be transformed into the frequency domain. Then the interesting frequency range is masked by a windowing function and shifted down to complex baseband. To obtain a complex time-domain representation of the channel, the IDFT has to be applied on the discrete-frequency sequence. From these processing steps it is seen, that a straight-forward conversion for the channel model is not possible. Such a direct model requires sampling of the channel with $\lesssim 1$ GHz which consumes a lot of power and can not be directly implemented in the DSP hardware.

This well prepared, standardized impulse response has to be implemented with the parallel filter structure shown in Fig. 2.4 to be able to process the UWB signal bandwidth in real-time. The design of filters to achieve sufficient separation and a correct mapping is following in the next subsections

2.4.1. Design of the Filters for Subband Processing

For designing the filter bank it is required to have an overall frequency response which is flat over the entire 528 MHz bandwidth of interest. This is obvious since the UWB transfer function has to be modeled by these subband filters. The filters used for the

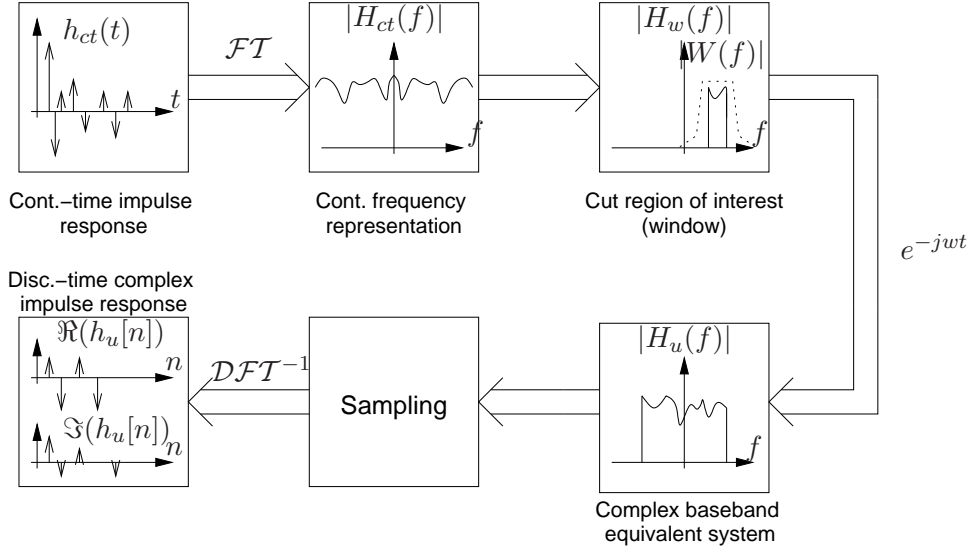


Figure 2.7.: Processing steps to obtain subband representation

filter bank are generally lowpass prototype filters. To obtain good separation between the subbands, it is desired to have filters which have no attenuation in the passband region and infinite attenuation in the stopband regions. However, this leads to the well known rectangular filter (in the frequency-domain) which results in an infinitely long sinc function in the time-domain. Thus realization of such a filter is not possible at all. For realizing the filter bank, some overlapping between the filters has to be allowed which introduces non-idealities in the subbands. For maximally decimated filter banks, which consist of just two filters, the cancellation of the introduced aliasing after downsampling is possible [38]. An extension of the approach to M filters in a filter bank is shown in [39,40] but requires extra computational complexity. Generally, the filter length of a very sharp finite impulse response (FIR) filter is inversely proportional to the transition width [41]. As a consequence, very sharp FIR filters are also very long filters. On the other hand it is desired to use FIR due to their simplicity and properties like linear phase and stability. Thus, implementation complexity stays rather high. One approach to design very steep filters and at the same time just slightly increasing the complexity is shown in [42]. The technique to achieve the steep filters is called *Frequency Response Masking* and is described in more detail in the following subsection.

2.4.2. Frequency Response Masking Filter Design

The Frequency Response Masking (FRM) approach tries to exploit the shrinking of the transition band when interpolating an impulse response of a low complexity filter. Generally, the steps used for creating a very steep transition band filter are depicted in Fig. 2.8.

First, it is assumed that the prototype filter $h_a[n]$ is given as depicted in Fig. 2.8(a) where the transition bandwidth is defined in the passband edge (θ) and the stopband edge (φ). When interpolating the filter with $M - 1$ zeros, M replicas in the frequency domain occur, as depicted in Fig. 2.8(b). Additionally, this Figure shows the complementary filter transfer function with the dashed line, $|H_c(e^{jM\omega})| = 1 - |H_a(e^{jM\omega})|$. This complementary

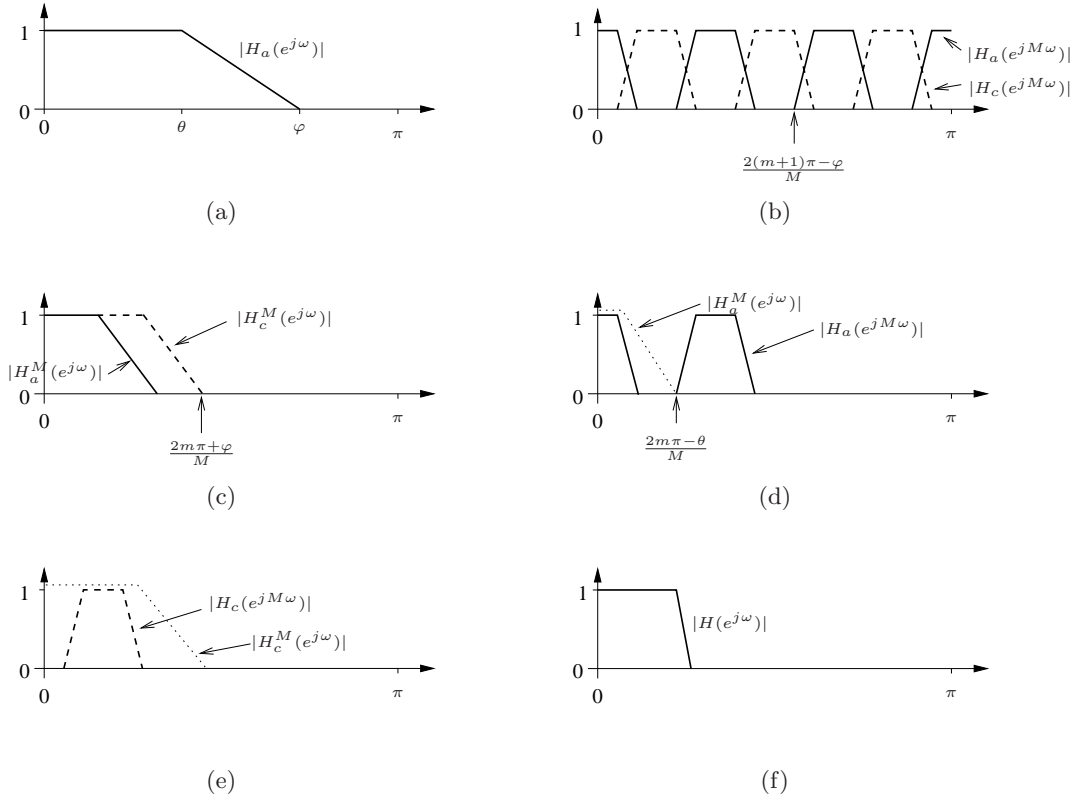


Figure 2.8.: Frequency Response Masking (FRM) technique: (a) Low complexity filter with wide transition band; (b) upsampled version of the filter (solid line) and complementary upsampled filter (dashed line); (c) Low complexity filters for rejecting the interpolation images; (d) Result after rejecting interpolation images; (e) Rejection of images for the interpolated complementary filter; (f) Final, frequency response masked filter with steep transition edge

filter is necessary to achieve a flat frequency response in the passband region. According to the desired needs of the application, the masking filters $h_a^M[n]$ and $h_c^M[n]$ are designed to attenuate the unwanted replicas from the interpolation process (*cf.* Fig. 2.8(c)). Also the masking filters can have a “wide” transition bandwidth and thus relax requirements on the implementation complexity. As one can see in Fig. 2.8(d) and Fig. 2.8(e), the remaining copies of the interpolated filter $h_{Ma}[n]$ and the complementary filter $h_{Mc}[n]$ are very narrow band filters with very narrow transition bandwidths, i.e., steep edges. Adding the remaining parts of the two interpolated filters results in a filter with as steep edges as the interpolated filters, and if the filters are complementary they should add in the passband region to a flat frequency response (*cf.* Fig. 2.8(f)).

2.4.3. Mapping the Transfer Function on the Filterbank

For this specific problem a simplified frequency masking approach to design the prototype filter was used. This is necessary to obtain a baseband equivalent description of the wireless channel in each subband. The use of a complementary filter for designing a flat frequency response in the passband was avoided and a wideband lowpass filter was interpolated. Due to the interpolation very steep edges of the filter, as desired for the application, are obtained. Furthermore, the lowpass filter for the frequency masking approach was designed such that, after interpolation, the bandwidth of the filter is 80 MHz. The steep edge is already achieved with one filter and another lowpass suppresses the periodic images from the interpolation to get a very nice filter with the desired frequency response. For the FRM filter 13 complex coefficients have been used which is reasonable to be computed in realtime on the available technology.

The transfer function of the UWB channel within the 528 MHz of interest is mapped on the response of each subband filter. Each filter models then part of the overall transfer function. Ideally the filterbank response should be flat to not introduce distortion within the modeled transfer function. This modeling process is depicted in Fig. 2.9 where the sum of the subfilters is nearly the same as the original frequency response.

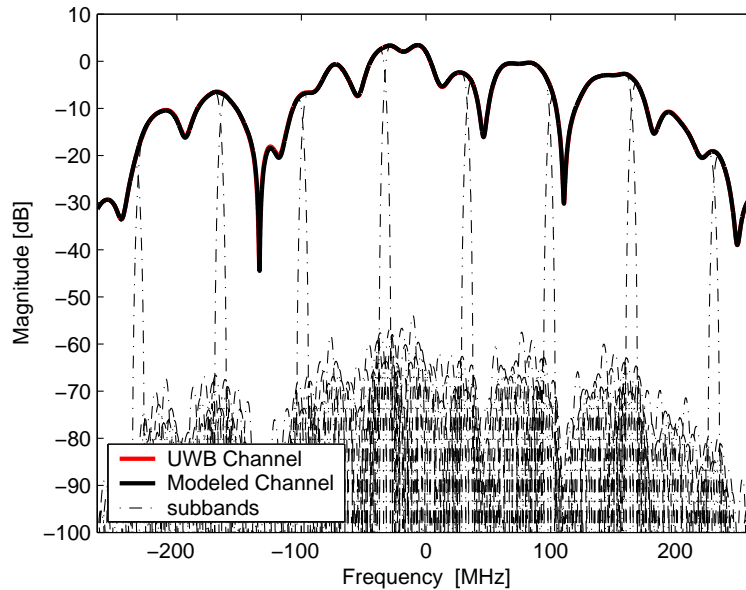


Figure 2.9.: Mapping of the transfer function to the shifted prototypes

Now, each of the filters can be downsampled and used for the individual subband representation of the propagation channel. The downsampled filters are now used as channel responses $h_k[n]$, $k = 0, \dots, M - 1$ as shown in Fig. 2.4.

2.4.4. Synthesizing the UWB Channel

As already seen in Fig. 2.4, the channel response has to be synthesized at the output of the system. In the presented example each of the subbands, which are individually processed in the complex baseband, has to be shifted to its correct position to model the 528 MHz of

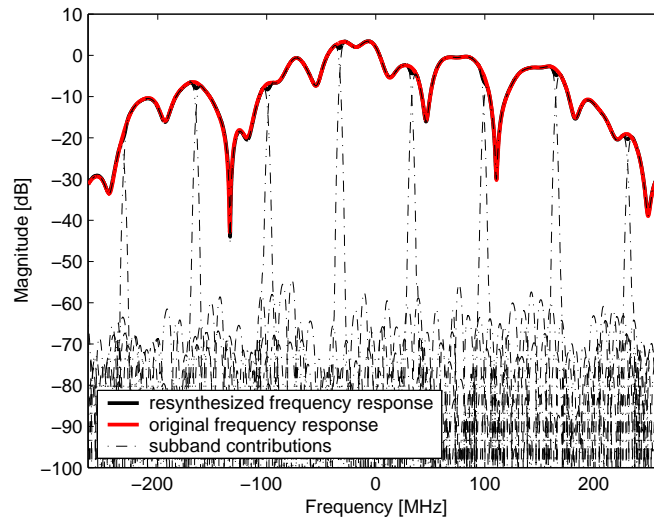


Figure 2.10.: Synthesized frequency response of the UWB channel

bandwidth. This is done in the analog domain in the presented structure. The DACs at the output stage of the synthesis filter bank have to be modeled. Additionally the modulators are assumed to be ideal, i.e., they do not introduce additional distortion when shifting 80 MHz of bandwidth to the correct position in the frequency domain. This assumption is reasonable since modulators can already be built for much higher local oscillator (LO) frequencies and bandwidths that work without problems. For the MATLAB simulations the DAC is represented by an upsampler and a reconstruction filter (interpolator). If we look at the output of the overall system (*cf.* Fig. 2.4), which models our UWB channel transfer function an overall transferfunction as seen in Fig. 2.10 is observed at the output $r(t)$. The overlapping regions of the subband filters show some dips due to the steep-edge filters used, otherwise the two transfer functions perfectly match (*cf.* Fig. 2.10). Please note that each individual filter has been downsampled before and information has been lost during this process.

It is seen in this section that a modeling of the channel in a subband structure is possible but requires a lot of additional hardware to make the system work as desired. First of all two mixer stages have to be implemented, which is a lot of hardware to be integrated and calibrated to achieve a flat frequency response from $s(t)$ to $r(t)$ when the subband filters are not used. Furthermore, the number of coefficients of the subband filters is very low because of the limitation due to processing speed. This clearly diminishes the performance of the system and gives a problems in modeling the channel.

2.5. Parallel Receiver Architecture for Standardized UWB Communication

Similarly to the parallel transmitter architecture, the receiver can be implemented in a parallel manner. One approach for a parallel receiver is shown in [43] where the authors proposed a bank of analog modulators and analog lowpass filters to achieve band separa-

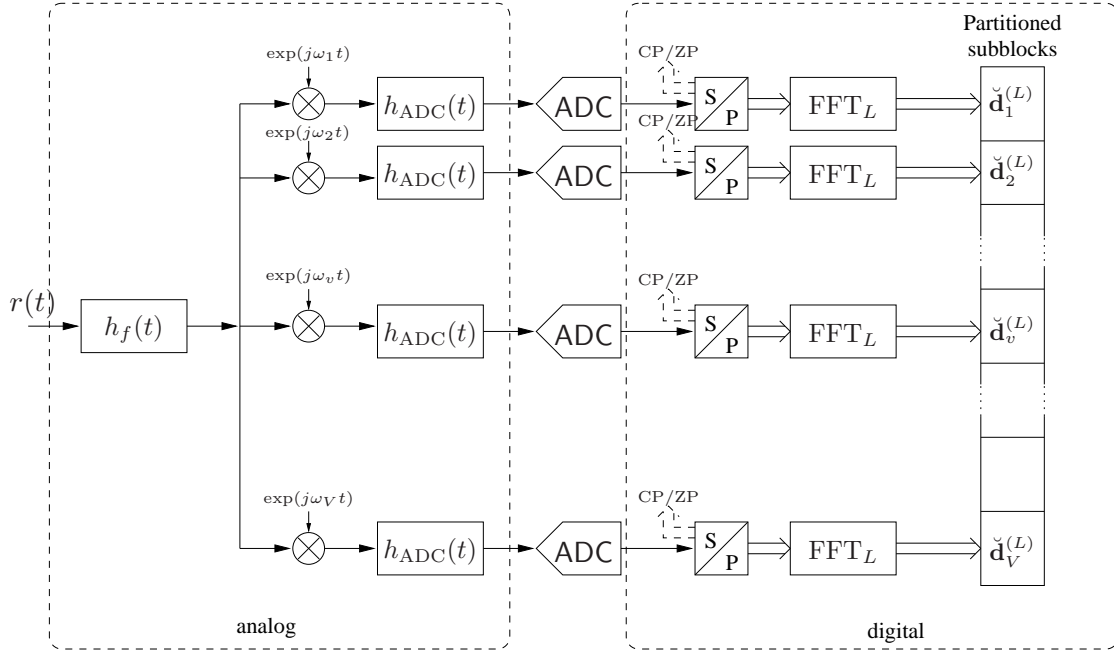


Figure 2.11.: Parallel receiver implementation for standardized high speed UWB communication

tion. If the steepness of the analog frontend filters is high, perfect separation between the subbands is possible. In the previously mentioned reference, 9th-order Butterworth filters are used to achieve good band separation. Additionally, the authors there use digital filters to equalize the distortions occurring in the analog front-end in the digital back-end. This means that for each subband channel a separate digital equalizer has to be computed. Anyhow, equalization has to be performed to combat the effects of the wireless propagation channel and these two equalizers can be combined into one filter. The receiver architecture proposed here is shown in Fig. 2.11. At the receiver input the received signal $r(t)$ is usually captured from the antenna and shifted to the complex baseband by the RF front-end. The signal is then bandlimited to 528 MHz specified with the analog front-end filter $h_f(t)$ and then fed into the modulator bank. Then, as already seen in the transmitter, a modulator bank shifts the band-limited received signal to perform subband analysis. For the Analog-to-Digital Converter (ADC), an analog anti aliasing filter has to be used to achieve subband separation and proper conversion of the signals into the digital domain. The previously added cyclic extension (or zero padded extension) has to be removed from the signal, and a serial to parallel conversion (i.e., a buffering) of one data subblock has to be performed in each channel before a final DFT is performed to obtain the transmitted data. In the receiver, an FFT can be computed because in each branch $L = 2^x$, $x \in \mathbb{Z}$ subcarriers are included and with the previously defined system parameters (128 carriers, separation into $V=2, 4$, and 8 subbands), the computationally efficient DFT can be used.

System Model

A system model for the receiver structure shown in Fig. 2.11 is derived. For the system model, it is assumed that the received signal is an OFDM signal consisting of N carriers which are modulated by data symbols with known modulation format, i.e., BPSK, QPSK, or higher order QAM modulation. Furthermore, it is assumed, that the received signal is a bandlimited signal. With respect to Fig. 2.11, the first analog front-end filter $h_f(t)$ will provide this feature for the receiver. Furthermore, we do not consider any synchronization process of the receiver on the carrier and symbol start from the transmitter. For the processing steps described here, the two systems are assumed to be perfectly synchronized. This is reasonable, since the effect of the parallel structure on the overall performance of the receiver is investigated. Similarly to the transmitter the system is analyzed according to the overall performance and on a carrier-by-carrier basis.

By expressing the essential receiver operation, given by the FFT on a block of samples of the received signal, with the cyclic extension removed, one obtains the data in the frequency domain, i.e.,

$$\hat{d}[k] = \frac{1}{\sqrt{N}} \sum_{n=0}^{N-1} r[n] W_N^{kn}, \quad (2.23)$$

where $\hat{d}[k]$ is the data symbol at each carrier, $r[n]$ is the sampled and synchronized OFDM time-domain signal and W_N^{kn} are the complex exponentials of the subcarriers. The set of complex exponentials W_N is defined in (2.3). Similarly to Section 2.3 the FFT can be expressed in a matrix and vector notation as

$$\hat{\mathbf{d}} = \mathbf{F}_N \mathbf{r}, \quad (2.24)$$

where \mathbf{F}_N is an N point Fourier transform matrix where the (n, k) th entry is given as $\exp(j2\pi nk/N)/\sqrt{N}$, \mathbf{r} is a vector of received samples, and $\hat{\mathbf{d}}$ are the estimates of the transmitted data symbols, respectively. Similarly to the generation process, if the signal would be sampled at Nyquist rate, we could decompose the signal into disjunct blocks of samples from the received signal and compute the FFT on each subblock. In the previously introduced matrix notation we then get,

$$\hat{\mathbf{d}}_v = \sum_{v=1}^V \mathbf{F}_N \text{diag}\{\mathbf{w}_N^{(i)}\} \mathbf{H}_{ADC} \mathbf{r}, \quad (2.25)$$

where $\hat{\mathbf{d}}_v$ has similar structure as \mathbf{d}_v in (2.6) and each vector is N elements long and consists of $L = N/V$ data symbols and $N - L$ zeros. The front-end filters $h_{ADC}(t)$ are represented by the matrix \mathbf{H}_{ADC} where the bandlimitation has implicitly been assumed. Otherwise the response of $h_f(t)$ can be included into \mathbf{H}_{ADC} to get a combined response. The vector $\mathbf{w}_N^{(i)}$ represents the shifting in the frequency domain and is similarly defined as in (2.7). As already elaborated in the generation part, the size of the FFT computed in each branch can be reduced. Please note that each FFT computed in the receiver has length L and if proper filtering can be achieved in the continuous time domain, no oversampling is necessary as for the signal generation where the DAC cannot be used up to its theoretical limit.

If we define the length of the CP/ZP with C in each subband, the CP/ZP has a length of $C' = C/V$ which has to be stripped for the FFT computation. Thus the samples obtained after filtering and decimation collected in a vector are given as

$$\check{\mathbf{r}}_v = \left[\begin{array}{c} \mathbf{r}_{CP} \\ \check{\mathbf{r}}_v \end{array} \right]_{L+C' \times 1}, \quad (2.26)$$

where with the stripping of the CP/ZP \mathbf{r}_v with dimensions $L \times 1$ is obtained. Each data symbol can now be demodulated by performing the FFT on the block \mathbf{r}_v and the estimated data symbols $\check{\mathbf{d}}_v^{(L)}$ in each block are obtained. Similarly as for the transmitter structure the performance of this receiver structure has been benchmarked with computer simulations shown in the next section. By obtaining similar equations as for the transmitter, it is expected to see similar effects in the performance results. For the additional MSE on each carrier the error is expected to be higher due to cutting of the sidelobes of the analog front-end filters and slight overlapping of the frequency subbands. Furthermore, this additional error will result in an error floor in terms of symbol-error ratio (SER) due to these non-idealities.

2.6. Simulation Results

To obtain performance results for the proposed structure computer simulations have been carried out. One thing to consider throughout the simulations is that each of the blocks of data has to be processed with some oversampling because also realistic ADCs and DACs cannot be used up to half of the sampling frequency. The anti-aliasing filter in front of the ADC ($h_{ADC}(t)$) in the receiver was chosen to sufficiently suppress the bandwidth from adjacent channels in the parallel structure (app. 40 dB). The interpolation filter in the DAC ($h_{DAC}(t)$) is assumed to be a lowpass filter with a transition bandwidth from $0.4f_s$ to $0.6f_s$, f_s denoting the subband sampling frequency. Modeling the transfer function of the internal oversampling with these characteristics is very well described in numerous data sheets [44, 45].

For the computer simulations we do not consider any particularities of the proposed UWB signal structure (asserting pilot tones and introducing redundancy at the band edges) except the nulling of the DC component. This enables us to observe each carrier separately and to see the effects of combining the subband generated signals. The carriers of the OFDM signal are modulated by randomly generated QPSK data symbols.

For the subband decomposition, different numbers of blocks ($V=2, 4$, and 8) have been used to generate a signal. Similarly, a signal $x[n]$ according to the specifications of the UWB standard document is generated by computing an 128 IFFT and compared to the subband signal. To benchmark the performance of the two signals after receiving, both signals have been demodulated by a full-rate OFDM receiver. Furthermore, perfect synchronization between transmitter and receiver is assumed. The conventional OFDM receiver chops the CP/ZP and performs an FFT on the data vector $\hat{\mathbf{x}}$, yielding the estimated data vector $\hat{\mathbf{d}}$. After demodulating the data each data symbol is compared to the original QPSK constellation point in the frequency domain and the distance is defined as an error measure as in (2.12). Thus, the error is computed as the difference from the resulting constellation point to the desired constellation point after demodulation. This

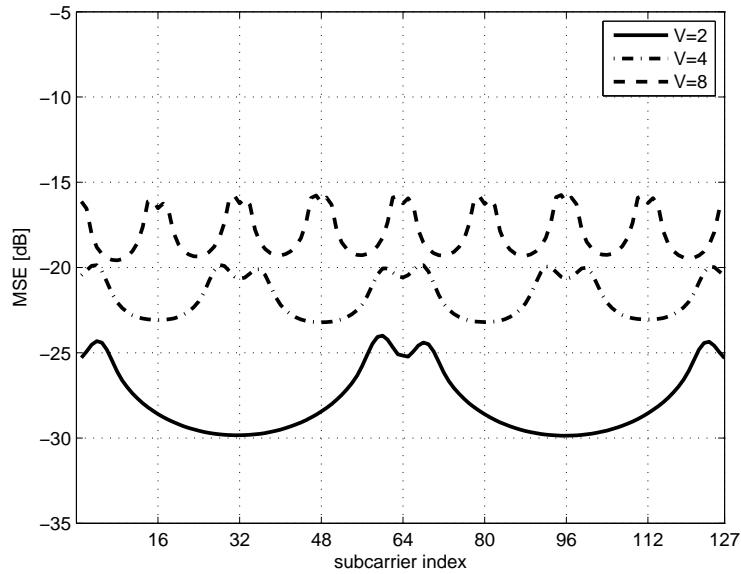


Figure 2.12.: Additional MSE due to subband signal generation CP

error measure is defined for each subcarrier $k = 1, \dots, N - 1$ (excluding the DC carrier). The error should clearly represent first of all the effect of the reconstruction filters within the DACs and secondly the signal truncation of $\hat{\mathbf{x}}$. To demonstrate the additional decrease when implementing the OFDM system in parallel, the mean squared error (MSE), i.e. $E\{|e[k]|^2\}$ has been plotted on a logarithmic scale in Fig. 2.12, for each subcarrier.

It is seen very clearly, that for all different numbers of subbands V , the carriers on the borders of each subband are distorted more than the carriers in the centers of the subbands. For the case of $V=2$, the additional distortion is very low compared to the other approaches for carriers within the subband. Since there are just two closely arranged bands in the frequency domain the introduced distortion is very small compared to a case where 4 or 8 bands are overlapping. For $V=4$ and $V=8$ subbands, the mean squared error still has this regular structure where the band edges become visible but the MSE is generally higher due to more contributions from the other subbands (*cf.* (2.15)). Similar results are achieved when instead of a cyclic prefix a zero-padded prefix is used (*cf.* Fig. 2.13).

Furthermore, the effect of this additional distortion in terms of SER over an additive white Gaussian noise (AWGN) channel (*cf.* Fig. 2.14) is visualized. A conventionally generated OFDM signal is compared to an OFDM signal generated with the proposed method. The signal is sent over an AWGN channel and received by a conventional OFDM receiver which omits either cyclic or zero-padded extensions and performs an FFT on the buffered received signal. The subband decomposition is considered as an inherently present systematic error which diminishes the performance in terms of SER. Furthermore, the parallel receiver architecture has been implemented and evaluated. Generally, four cases to be evaluated are possible with the two switches offering two methods. However, the most interesting ones are when the signal is generated in subbands, how the full-rate receiver performs compared to the receiver performance when the signal is generated at

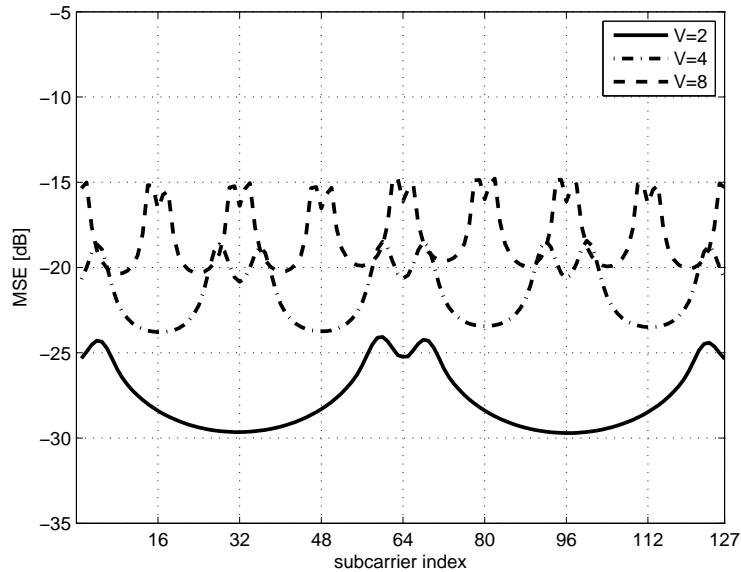


Figure 2.13.: Additional MSE due to subband signal generation ZP

full rate. Another interesting setup is to benchmark how the parallel receiver performs when it receives a signal generated at full rate. These two scenarios are compared in this thesis.

In Fig. 2.15 the SER for the subband generated signals are shown. It is assumed that a cyclic extension of 32 samples (as proposed in [18]) is used. For the case of $V=2$ subbands the best performance results in terms of SER are achieved. This is obvious since the additional error has the lowest power for that case and the effects are similar as adding another Gaussian noise variable. For the two other cases ($V=\{4,8\}$) the average power of the introduced distortion is bigger, thus resulting in worse SER performance. However, the signal which was generated in 4 or 8 subbands might still be used since the uncoded SER plots are shown here. Further error correction codes have to be applied anyway to be resistant to the UWB propagation channel.

Similar observations are found if the signals with zero-padded prefix are compared. Again the subband decomposition with $V=2$ bands results in the minimum average error (*cf.* Fig. 2.16).

As already shown for the transmitter structure, similar computer simulations are performed to verify the performance of the receiver structure. For the structure $V=2, 4,$ and 8 subbands are used in the receiver unit to parallelize the processing. Similarly as for the transmitter, a complex Gaussian channel which truly shows the additional influence of the parallel structure on the individual subcarriers was used. The two previously defined error measures have been used here again. First of all the additional MSE over each subcarrier is visualized in Fig. 2.17 and Fig. 2.18, respectively.

There is almost no difference visible between a cyclic extension and a zero padded prefix. One other interesting fact is that the subband structure is nicely visible for $V=4$ and 8 subbands. For $V=2$ subbands the additional error spreads almost equally over the whole

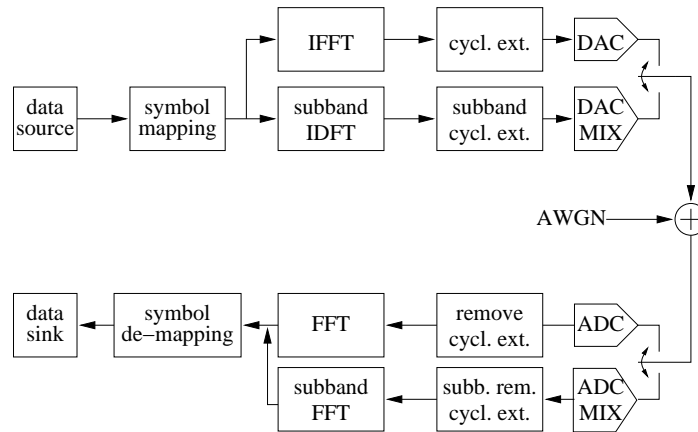


Figure 2.14.: Comparison of conventionally generated signal with subband generated signal

number of subcarriers. The high peaks at the subband edges for $V=4$, and 8 are due to the analog anti-aliasing filters which have to separate the bands sufficiently and thus suppress part of the subband information.

Similarly, the effect of the subband architecture was shown according to the additional BER caused by non-idealities in the architecture. It is seen that with two subbands almost no additional distortion is encountered. To provide a signal for receiver testing, a conventionally generated signal has to be used. Thus, the effect of the transmitter is not visible here in the additional error plots. For the higher-order subbands, the additional error at the band edges is seen in Fig. 2.17 and Fig. 2.18, which results in a bit error floor as seen in Fig. 2.19 and Fig. 2.20, respectively. To combat this effect, an equalizer for each subband can be used. This equalizer has been applied already in [43] and can be optimized according to the minimum mean square error criterion [46].

2.7. Conclusions

In this chapter a way to parallelize the elements of a standardized UWB communication system according to [15] in the frequency domain has been presented. The mapping of the wideband wireless communication system for transmitter, channel, and receiver was demonstrated. The parallel implementation with a hybrid continuous-time/discrete-time filterbank to achieve separation between the subbands has to be used to be able to implement the wideband transceiver.

Typically, the OFDM signal generation is done with a single chip solution where it is possible to handle such large bandwidths. The proposed system offers an alternative signal generation scheme with low-complexity and low-cost hardware, by using several processing units at the same time. Due to the generation of the subband signals and stacking the spectra, overlapping of the different frequency contents occurs. To be able to convolve the transmitted signal with the respective subband responses, the channel has to be analyzed and prepared with the subband channel responses. This is achieved by digital pre-processing of the frequency response filters by frequency response masked prototype filters which achieve very steep transition band edges with only a dozen coefficients. The

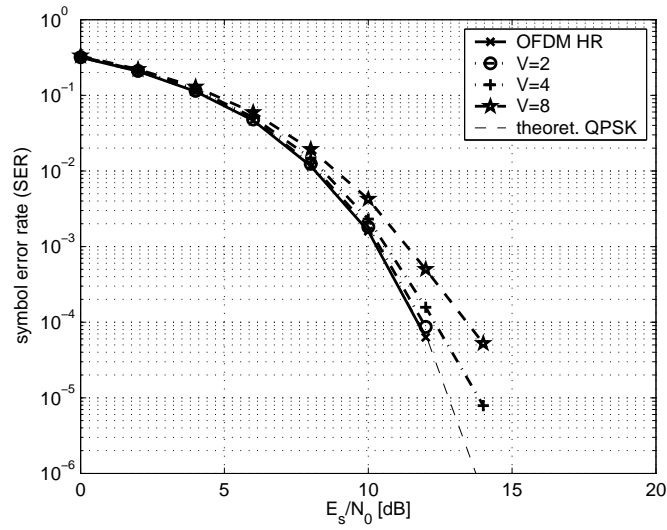


Figure 2.15.: Comparison of OFDM signals with CP

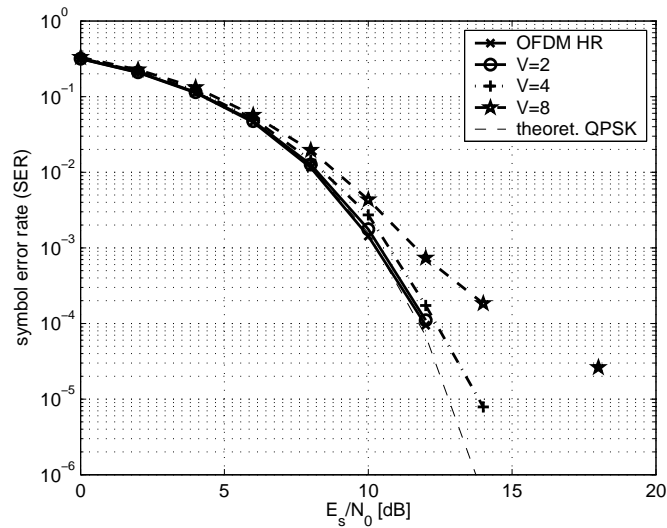


Figure 2.16.: Comparison of OFDM signals with ZP

frequency responses of the standardized channel model are then modeled in a parallel way and the overall modeling in the subbands achieves similar performance as the modeling with a single band. Furthermore, a parallelization of the receiver is possible.

The effect of this overlapping is visualized as an MSE on a carrier-by-carrier basis. It is seen clearly that the subcarriers at the band edges are more distorted than others. Additionally, the distortion effect in terms of SER has been visualized. Clearly, a relation between high error peaks and erroneous symbols is visible. Similar performance degradation as for the transmitter can be observed in the receiver. Clearly, at the band edges the additional error due to the finite slope of the analog front-end filters is visible in the result. An SER degradation can be observed in the subband architecture. The occurring

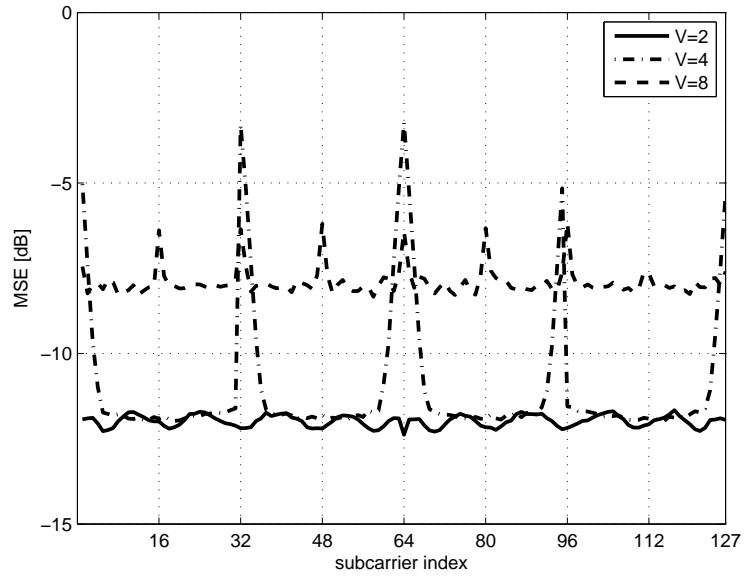


Figure 2.17.: MSE for subcarriers after parallel receiver CP

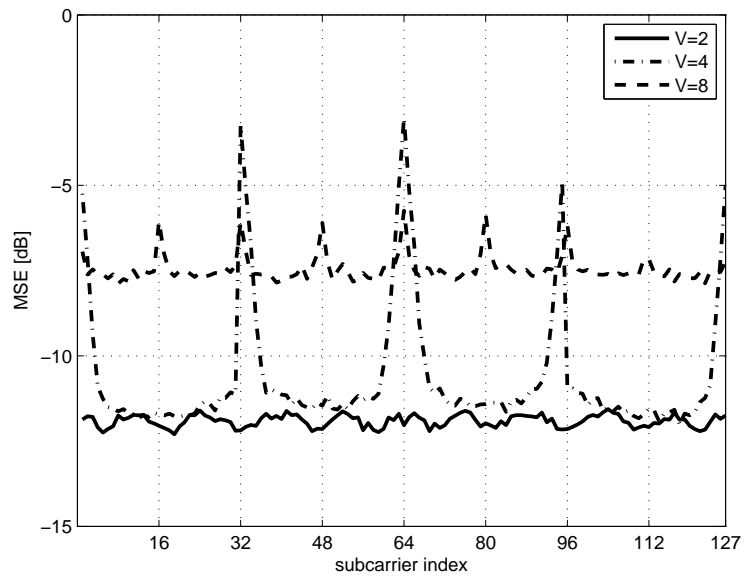


Figure 2.18.: MSE for subcarriers after parallel receiver ZP

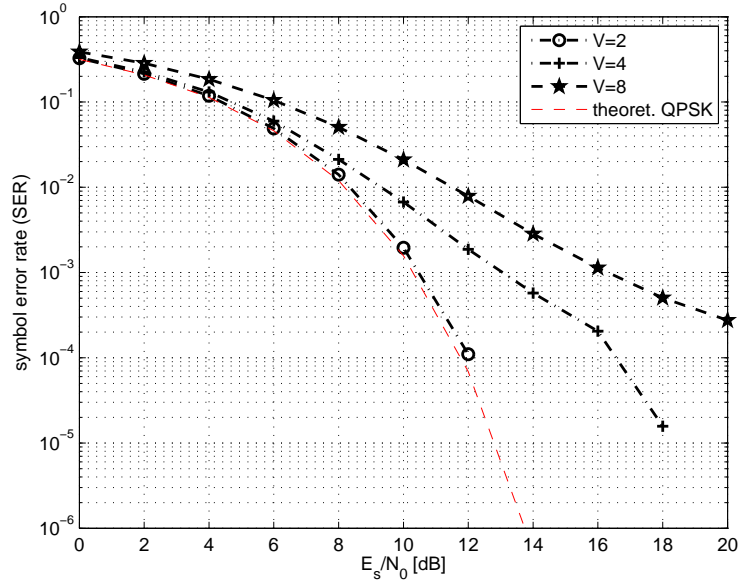


Figure 2.19.: Simulation results for parallel receiver architecture and OFDM using CP in terms of BER

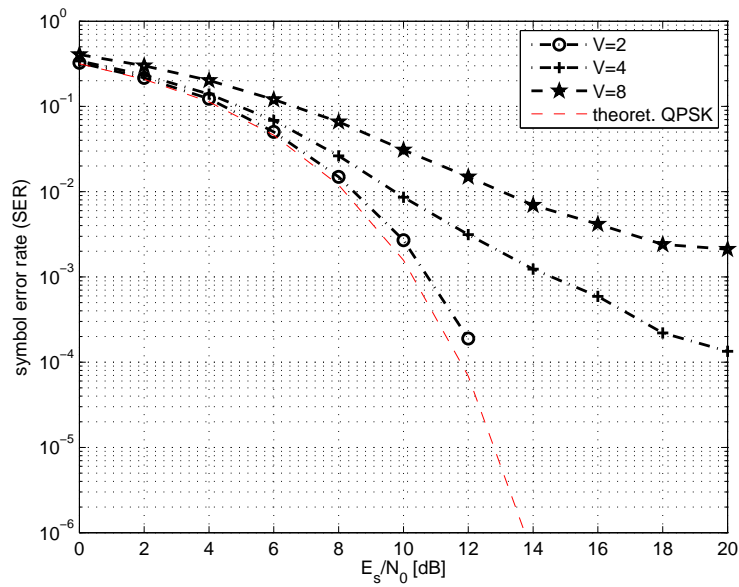


Figure 2.20.: Simulation results for parallel receiver architecture and OFDM using ZP in terms of BER

interference can be taken care of with an equalizer adapted during a training or calibration period. Such an equalizer has to be used anyhow if the degradation of the signal

due to a wireless propagation channel is considered to recover the transmitted data. One advantage of OFDM is that each carrier can be equalized in amplitude and phase by a single complex coefficient. However, this only works as long as the channel delay spread is shorter than the guard interval. If the channel spread is longer than the guard interval, ISI occurs which has to be equalized with an equalizer filter response, i.e. employing more than a single coefficient. Furthermore, OFDM is sensitive to carrier offsets where the orthogonality between the carriers gets lost. This inter-carrier interference (ICI) can be combated by the cyclic extension such that in one symbol all subcarriers have an integer number of sine waves to preserve orthogonality.

Pulse-Based UWB Communication

For high speed UWB communication systems a conventional OFDM signaling scheme has been extended to current technological limits. This helped on the one hand in realizing different implementations in a short, predictable time because experience in designing OFDM chips (like used in WLAN) is already available in many companies. This is, however, completely contradictory to the original idea of UWB, i.e., using very wideband signals (short pulses) and exploit the frequency diversity of the signals when they are received. It is also questionable whether the OFDM transceivers can be built in order to fulfill low-power constraints. One second advantage of the UWB technology is that, due to its high bandwidth, a high positioning accuracy can be achieved. In a positioning system there are several possibilities to achieve accurate estimates of the current position of simple tags or advanced stations in space which can be tracked due to the fine time resolution of UWB signals. For details about positioning algorithms we want to refer the interested reader to [47, 8] and the references therein. Combining these perspectives and requirements and keeping current technological limits in mind, the IEEE has released a standardized communication scheme recently [6] which will be analyzed in this chapter. First an easy way to achieve broadband, universal signal generation, is presented. Furthermore, if mismatches in the presented structure occur, we can find a way to digitally pre-distort the signals so that a compensation of these effects is achieved in the analog domain. In the end an analysis of receiver structures for the standardized scheme is presented, and a comparison of different receiver architectures according to their performance in a single-user and in a multi-user scenario is shown¹.

3.1. Introduction

An alternative to the extension of already existing communication systems to make them “Ultra” Wideband as presented in Chapter 2, is to use very narrow pulses, which also occupy a very broad spectrum. Unlicensed signal transmission is allowed according to the authorities in the frequency range from 3.1 to 10.6 GHz. However, this very liberal opening

¹The sections about Time-Interleaved Digital-to-Analog Converters and the proposed compensation approach in the TIDAC structure have been published and submitted by the author to international conferences [10, 48].

of the “ether” is only available in the USA. Conversely, the European Commission followed much more conservative guidelines to propose a regulation directive for the EU member states [2] but it is up to national governments to implement the directive, where most of the member states are currently still belated. Only the UK and its respective regulation authority OFCOM has implemented the directive in its current form. Generally the spectral emission limit already defined by the FCC in the US was set to the electromagnetic compatibility bound (EMC) of a power spectral density (PSD) of -41.25 dBm/MHz [1].

As already mentioned, as an alternative to a wideband extension of a conventional wireless system, very short pulses can be transmitted. To comply with spectral regulations many different pulse shapes can be used, which by their shape can be made to fit the spectral emission mask [49]. What can be done additionally is to shift the pulses by mixing them towards higher frequencies. However, the direct and easy baseband transmission is not possible anymore when using a carrier to shift the signal spectrum. Also from a low-power perspective an additional RF mixer consumes a lot of power which is usually not desired.

Also the IEEE recognized the great potential of pulse based Ultra Wide-Band signaling for communication and positioning applications. Thus, it formed the IEEE 802.15 Task Group 4a to define an alternative PHY and MAC for wireless personal area networks (WPANs). The main task was to develop an alternative PHY providing simultaneous communication and high precision ranging with low power and system scalability. These endeavors in defining a new PHY for the new technology succeeded in Sept. 2007 in an addendum to the current standardization document [6]. Therein, standardized UWB pulses have been specified, which have a root raised cosine (RRC) pulse shape. The RRC pulse shape is mathematically defined as

$$x(t) = \begin{cases} \frac{1}{\sqrt{T}} \cdot \frac{\sin(\pi(1-\beta)t/T) + (4\beta t/T) \cos(\pi(1+\beta)t/T)}{(\pi t/T)(1-(4\beta t/T)^2)} & t \neq 0, t \neq \pm T/(4\beta) \\ \frac{1}{\sqrt{T}} \left(1 - \beta + \frac{4\beta}{\pi}\right) & t = 0 \\ \frac{\beta}{\sqrt{2T}} ((1 + 2/\pi) \sin(\pi/4\beta) + (1 - 2/\pi) \cos(\pi/4\beta)) & t = \pm T/(4\beta) \end{cases}, \quad (3.1)$$

where β is a roll-off factor defined as 0.6, and T is the pulse width. Beside the pulse-based signaling employing wideband pulses, several different other signals have been standardized in the current document. One method to generate wideband signals is to drive an active circuitry into non-fading nonlinear behavior and let it generate chaotic waveforms which are noise-like signals occupying a wide bandwidth [50]. Furthermore, the generation of chirped signals is also possible to get wideband signals. There the frequency is continuously swept over a certain frequency range. Here chirping slopes of 500 MHz/2.5 ns are used to generate the pulses. Furthermore, another optional waveform are continuous spectrum (CS) pulses which are reference pulses with adjusted group delay. Generally, the pulse shape used in the standard is a reference pulse shape meaning that actually any pulse shape can be used in a standardized IEEE 802.15.4a communication system which has a certain correlation with this reference pulse [6]. The bandwidths for these standardized reference pulses are defined as 499.2 MHz and the whole frequency range from the FCC was densely packed with neighboring channels. On top of these “narrow” channels there are a few channels with app. 1.3 GHz which have intentionally overlapping frequency ranges, such that devices implementing different signal bandwidths can also communicate with each other and can capture sufficient energy from each other.

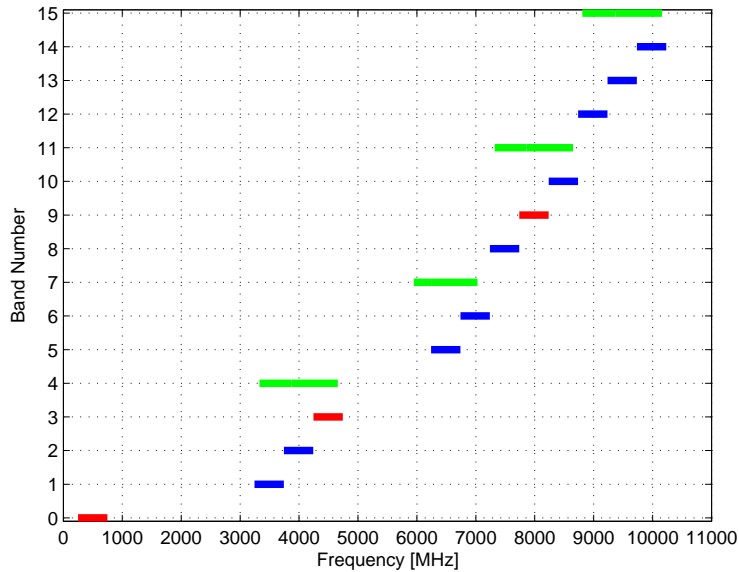


Figure 3.1.: Mandatory (red) and optional bands (blue: 499.2 MHz, green: >1 GHz) defined within the IEEE 802.15.4a standard

As one can see from the previous consideration it is very essential for a simulation environment to support all these different standardized pulse shapes and waveforms. Generally, positioning systems are designed for special operation environments which usually depend on the application scenario. In each of these scenarios, different positioning accuracy may be required. Furthermore, different features are required for each of these situations. Thus, individual systems which comply with emission rules are and will be developed. Additionally, requirements like low-power consumption, robustness to narrow-band interferers, and robustness against multipath propagation in harsh environments may have influence on the system design and on the selection of the system parameters like pulse shape, i.e., bandwidth, and signaling scheme, ... For that reason, also non standardized pulse shapes are interesting for several communication and positioning systems which might be developed in the future. In these new systems, higher bandwidths than defined in this channelized structure (*cf.* Fig. 3.1) are of interest to exploit the full diversity of the UWB signals. Furthermore, an adaptation to the environment (e.g., adapting to mutual antenna coupling) is only possible with a flexible pulse generation circuitry.

Due to these design challenges, the most general way to design such a flexible signal generator is to use a Digital-to-Analog Converter (DAC). The DAC operates with a certain clock frequency f_s which determines the maximum signal bandwidth the DAC is able to generate [31]. On the other hand, the DAC can generate an arbitrary waveform which is bandlimited by $f_s/2$, i.e., half the sampling frequency. However, a DAC which is able to generate a 7.5 GHz broadband signal would then require a sampling frequency of ≥ 15 GHz which is not feasible. Currently DACs generating GHz of signal bandwidth are available already on the market (see e.g. [51]). Another challenge for nowadays data converters is

to provide sufficiently high resolution to provide high Signal to Noise Ratio (SNR) for the generated signals [52]. If we consider the integration of the converter on a System on Chip (SoC) we also have to take power consumption and area into consideration. Generally, a tradeoff between all these system parameters has to be found for the application. It is recognized that the integration density of digital circuits grows much faster than the one of analog circuits, which results in an increasing gap between analog and digital circuits in terms of speed, area, and power consumption [53]. Fortunately, we can use digital signal processing to overcome the analog impairments of data converters [54]. One approach of extending the limitations of current DACs is shown in this thesis. By using multiple DACs one can extend the bandwidth of the analog signals generated by the architecture. To achieve this, some digital preprocessing has to be done in the digital domain and a clock phase shift has to be generated to achieve a time-interleaved generation of the DAC samples. Both components add complexity to the overall system but are relatively easy to realize. An equivalence of the proposed structure and a converter running at a higher sampling rate is shown in Section 3.2. By using multiple converters, also mismatches between these converters can be considered. One solution to compensate for timing offsets in a such a multiple converter system is shown in Section 3.3. On the receiver side, the generated signals have to be decoded by a proper receiver architecture. To evaluate the performance of the standardized IEEE 802.15.4a scheme, we propose three receiver architectures and compare them in Section 3.4.2

3.2. Flexible Generation of UWB Signals

In this work we focus on time-interleaved DACs (TIDACs) which consist of M DACs operating at low sampling rate. Each of the DACs is used with a phase-shifted clock, which results in time-shifted contributions to the output signal. The main advantage of the TIDAC is that due to the phase-shifted signals, the output signal seems to be generated at a higher sampling rate, given that the settling time of the individual DACs is high.

For the TIDAC, the clock generation adds more implementation complexity. However, this additional effort remains low because only a multiphase clock generator has to be used to clock the different DACs. For the two-channel case, this can be easily done by using differential signals. The additional complexity for the clock generation offers flexibility in pulse shape adaptation and generation which is needed in a demonstration environment. Using a TIDAC on a mobile device may consume more chip area than using a single DAC at the M -times higher speed but offers relaxed conditions for the individual converters which can then be optimized.

The TIDAC proposed in this thesis distinguishes itself from previous works as follows. The authors in [55] consider a time-interleaved scheme that consists of two DACs that are alternately switched on, i.e., either the first or the second DAC contributes to the output signal. An improvement for the output signal is achieved by mapping the data words with a return to zero (RTZ) code which helps avoiding glitches in the output signal [56]. However, this RTZ coding is not applicable to our structure because the output signal combination in our scheme is always the sum of the contributions of the individual DACs in the TIDAC.

Another approach using TIDACs is shown in [57], where the DACs are operated in a

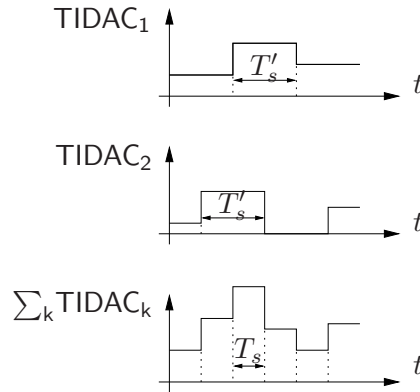


Figure 3.2.: Comparison of high rate DAC and TIDAC structure ($M = 2$; $T'_s = 2T_s$)

time-interleaved manner to achieve a signal with less distortions due to aliasing effects. The interleaving structure generates samples of the output signal with four DACs operating in parallel. At the output the signal is summed up and due to the overlapping of different samples an “averaging” effect is achieved and a similar signal is generated at the output. This scheme is depicted for a two-channel TIDAC in Fig. 3.2. The individual signals from the DACs are phase-shifted and overall output of the TIDAC is shown in the lowest picture.

The approach discussed in this chapter uses a similar structure with time-interleaved DACs, but uses a precoding scheme that allows to generate exactly the same signal on an M -times higher signal processing rate than the clock rate of a single DAC in the TIDAC. This enables to generate oversampled signals and allows low-complexity analog filters. Accordingly, the signals for UWB systems are generated by interleaving two or more DACs, where the precoding is done on an FPGA.

3.2.1. System Model

In the following section, a system model for the TIDAC is derived. When a signal is generated by a single DAC, each sample value applied to the digital inputs is converted into a voltage/current corresponding to its binary representation, and held over the sampling period T_s . This holding function is usually called zero-order hold (ZOH) function and simplifies the physical realization of a DAC which would have to generate δ -pulses filtered by an ideal lowpass filter. Thus, signals up to half the sampling frequency f_s , i.e., $f_s/2 = 1/2T_s$ can be generated with this converter. All other frequencies in the output spectrum are caused by the discrete-to-continuous time conversion, and are attenuated by the ZOH of the DAC. Conversely, if a signal as shown in Fig. 3.2 for the two-channel case, is generated with the TIDAC, not only one DAC is contributing to one sampling interval, but generally M DACs are contributing in one sampling interval T_s . Thus, in the time-domain the difference from the sum of all currently contributing samples to the new output value has to be computed to achieve correct signal representation for the next value to generate with one of the DACs in the TIDAC. Similarly, the spectral components occurring at frequencies around half the sampling frequency, are minimized by phase shifted versions of the same signal.

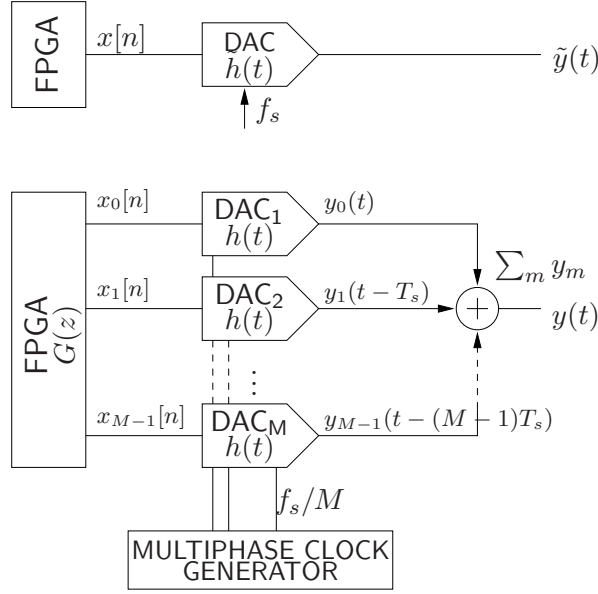


Figure 3.3.: Comparison of (a) high rate DAC and (b) TIDAC on system level

We are comparing the proposed structure to a single-channel DAC that runs on an M -times higher sample rate. Thus we assume that we have M channels in parallel in the time-interleaved structure. Each of these converters is characterized by the impulse response of the ZOH $h_k(t) = h(t)$ as shown in Fig. 3.3. In contrast, the single channel DAC has an M -times higher sampling frequency and an M times shorter ZOH response $\tilde{h}(t)$.

For a mathematical description we first describe the output signal $\tilde{y}(t)$ of the single-channel DAC at high sampling rate T_s . The DAC can be characterized with its ZOH response as

$$\tilde{h}(t) = \begin{cases} 1 & 0 < t \leq T_s \\ 0 & \text{otherwise} \end{cases}, \quad (3.2)$$

where one can show, that the frequency domain representation is given as [31]

$$\tilde{H}(j\Omega) = e^{-j\Omega T_s/2} \frac{\sin(\Omega T_s/2)}{\Omega/2}. \quad (3.3)$$

The generated signal spectrum $\tilde{Y}(j\Omega)$ is computed by the multiplication of the periodic, discrete-time spectrum of the signal $x[n]$ with the frequency-domain representation of the ZOH function. If we generate a sinusoidal signal with a frequency f_0 with a DAC that operates at a sampling frequency f_s we get sinc-weighted copies at frequencies $kf_s \pm f_0$, $k = 1, 2, \dots$ due to the ZOH.

Contrary, the output $y(t)$ of the TIDAC structure is the sum of the M parallel DACs $y_m(t)$

$$y(t) = \sum_{m=0}^{M-1} y_m(t - mT_s), \quad (3.4)$$

3.2. Flexible Generation of UWB Signals

where $y_m(t - mT_s)$ is the converted signal for each of the branches (*cf.* Fig. 3.3), i.e., the time-shifted, overlapping outputs of the DACs. The overall response for the TIDAC structure with prefiltering is

$$y(t) = \sum_{k=-\infty}^{\infty} \sum_{m=0}^{M-1} \left((x[kM + m] * g[kM + m]) \times \delta(t - kMT_s - mT_s) \right) * h(t), \quad (3.5)$$

where $x[kM + m]$ is the discrete-time signal, $g[m]$ is the precoding filter, $\delta(t)$ is the Dirac delta function, $h(t)$ is the reconstruction filter for each of the DACs (i.e., the ZOH), and $*$ denotes convolution. For the sake of simplicity, the filter $h(t)$ is assumed to be the same for each DAC. For the precoding of the signal we generally need an IIR filter of $M - 1$ taps since we have to account for all currently contributing M DACs and have to compute the new value to generate for the m -th DAC in the TIDAC. Thus only the additional difference to achieve the desired value in the converter array has to be computed. This filter operation can be described by an input/output relation as $y[n] = x[n] - y[n - 1] - \dots - y[n - M + 1]$, which is given in the frequency domain as the transfer function of a filter

$$G(z) = \frac{1}{\sum_{m=0}^{M-1} z^{-m}}. \quad (3.6)$$

We see that this filter has M poles in its frequency domain representation. For a practical implementation of this filter, an FIR approximation can be used. The continuous-time representation of the zero-order hold for one DAC is given by

$$h(t) = \begin{cases} 1 & 0 < t \leq MT_s \\ 0 & \text{otherwise} \end{cases}, \quad (3.7)$$

where MT_s is the sampling time of one single DAC in the TIDAC. Thus the frequency domain description of the output filter of one channel is

$$H(j\Omega) = \frac{1}{-j\Omega} (e^{-jM\Omega T_s} - 1), \quad (3.8)$$

which is again a sinc function as in (3.3) but at the lower sampling rate.

With these assumptions, the time-domain expression of (3.5) can be expressed in the frequency domain as

$$Y(j\Omega) = \frac{1}{T_s} \sum_{k=-\infty}^{\infty} \sum_{m=0}^{M-1} X_m \left(j \left(\Omega - k \frac{2\pi}{T_s} \right) \right) \times G \left(j \left(\Omega - k \frac{2\pi}{T_s} \right) \right) H(j\Omega), \quad (3.9)$$

where $X_m(j\Omega - 2k\pi/T_s)$ is the spectrum in the m -th channel, and $G(j\Omega) = G(e^{j\Omega T_s})$ is the filter operation performed in the digital domain. The filter responses are equivalent as long as the frequency remains below half the sampling frequency of the DAC at high rate.

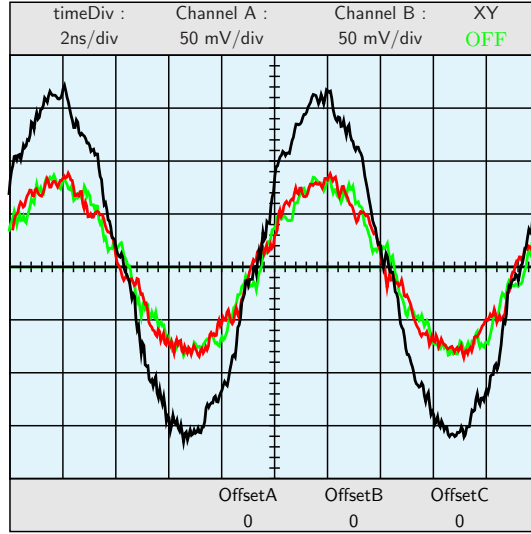


Figure 3.4.: Scope screen photo for time-interleaved sinusoids, red: TIDAC channel 1, green: TIDAC channel 2 (both with differential encoding $G(z)$), black: sum of the TIDAC structure providing the desired signal

The filter operation computed for signal generation in the discrete-time domain, is compensated by the combining stage, i. e., the simple adder, in the continuous-time domain. The resulting signal spectrum of a TIDAC structure should be the same as the one for a DAC, which operates at an M -times higher rate, i.e., the transfer functions $G(j\Omega)$ and $H(j\Omega)$ in (3.9) should compensate. For the output spectrum of the TIDAC structure, we get with (3.6) and (3.8)

$$Y(j\Omega) = \frac{1}{T_s} \sum_{k=-\infty}^{\infty} X \left(j \left(\Omega - k \frac{2\pi}{T_s} \right) \right) \times \frac{1}{\sum_{m=0}^{M-1} e^{-jm\Omega T_s} - j\Omega} \frac{1}{e^{-jM\Omega T_s} - 1}, \quad (3.10)$$

which should, if our assumption is correct, be equivalent to the spectrum $\tilde{Y}(j\Omega)$ which is given at the high sampling rate as

$$\tilde{Y}(j\Omega) = \frac{1}{T_s} \sum_{k=-\infty}^{\infty} X \left(j \left(\Omega - k \frac{2\pi}{T_s} \right) \right) \tilde{H}(j\Omega), \quad (3.11)$$

where $\tilde{H}(j\Omega)$ is given in (3.3). Thus, the two transfer functions $G(j\Omega)$ and $H(j\Omega)$ have to combine to $\tilde{H}(j\Omega)$, i.e.,

$$\begin{aligned} Y(j\Omega) &= \frac{1}{T_s} \sum_{k=-\infty}^{\infty} X \left(j \left(\Omega - k \frac{2\pi}{T_s} \right) \right) \times \frac{1}{\sum_{m=0}^{M-1} e^{-jm\Omega T_s} - j\Omega} \frac{1}{e^{-jM\Omega T_s} - 1} \\ &\stackrel{!}{=} \frac{1}{T_s} \sum_{k=-\infty}^{\infty} X \left(j \left(\Omega - k \frac{2\pi}{T_s} \right) \right) \times \frac{1}{-j\Omega} (e^{-j\Omega T_s} - 1) = \tilde{Y}(j\Omega). \end{aligned} \quad (3.12)$$

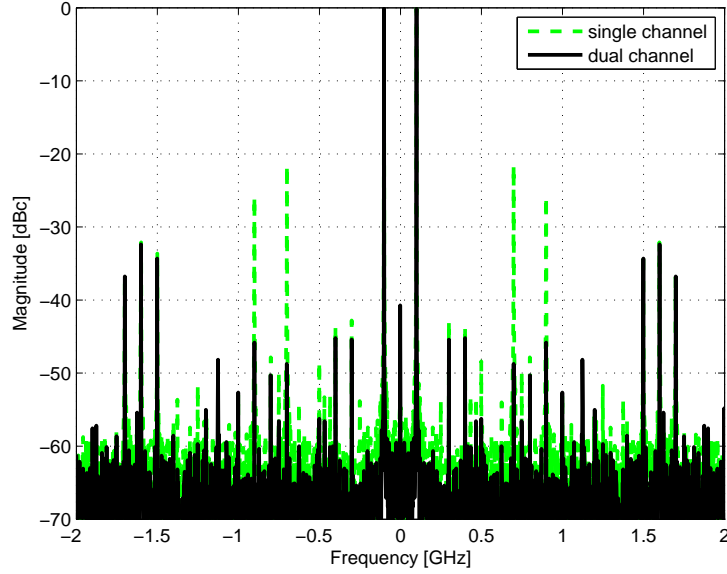


Figure 3.5.: Spectra for time interleaved sinusoid generation

By using geometric series we can simplify (3.10) to

$$\begin{aligned}
 Y(j\Omega) &= \frac{1}{T_s} \sum_{k=-\infty}^{\infty} X\left(j\left(\Omega - k\frac{2\pi}{T_s}\right)\right) \times \frac{1}{-j\Omega} \frac{1 - e^{-j\Omega T_s}}{1 - e^{-jM\Omega T_s}} (e^{-jM\Omega T_s} - 1) \\
 &= \frac{1}{T_s} \sum_{k=-\infty}^{\infty} X\left(j\left(\Omega - k\frac{2\pi}{T_s}\right)\right) \times \frac{1}{-j\Omega} (e^{-j\Omega T_s} - 1) \equiv \tilde{Y}(j\Omega)
 \end{aligned} \tag{3.13}$$

which proves our assumption that the two spectra are equal. Thus by digital precoding of the signal, the time-interleaved DAC produces the same signal as a DAC operating at an M -times higher rate by simply adding the signals at the outputs of the DACs. The computational complexity for the digital part of the transmitter is only slightly increased since the precoding is a rather simple filter operation. For communication signals with a limited signal alphabet, an alternative way to achieve similar results would be to store the waveforms and use lookup tables for signal generation. The method proposed with the precoding filter $G(z)$ has one essential drawback. Basically, $G(z)$ is an infinite impulse response (IIR) filter which has $M - 1$ poles in the z -plane. However, for the two-channel case the pole of $G(z)$ is exactly at $fs/2$ of the high rate. Thus at these frequencies the amplification of the noise is very high, but these frequencies anyway damped by analog filters. These spectral peaks occurring at these frequencies can be observed in Fig. 3.5 and Fig. 3.7 at 1.6 GHz and in Fig. 3.8 at 1.056 GHz.

3.2.2. Hardware Implementation

To show the results of our proposed architecture for UWB signal generation, we have realized a time-interleaved DAC on hardware. A Xilinx Virtex 4 evaluation board [58]

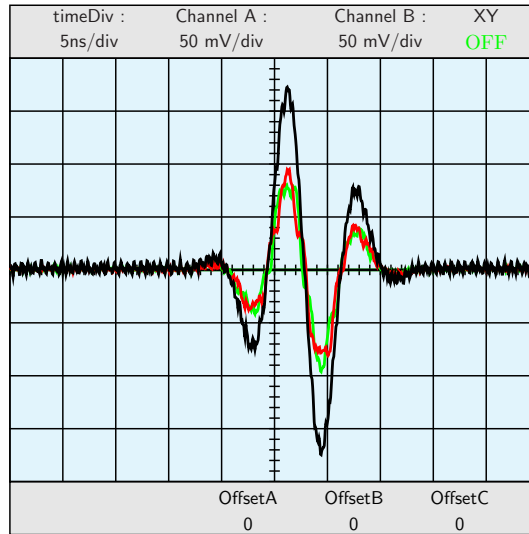


Figure 3.6.: Scope screen photo for time-interleaved UWB pulses, red: TIDAC channel 1, green: TIDAC channel 2 (both with differential encoding $G(z)$), black: sum of the TIDAC structure providing the desired signal

was programmed to generate the data sequence. For the Digital-to-Analog conversion we used two AD9734 high-speed DACs from Analog Devices [51] which can generate signals at conversion rates of up to 1.2 GSa/s. During our experiments we used a clock f_s of 800 MHz corresponding to the speed grade of the FPGA on the evaluation board. The data signals from the FPGA are differential LVDS signals which are fed into the DACs with a trace length and impedance-matched adapter board. The clock was generated by a Stanford Research Systems CG635 clock generator [59], which provides a stable differential clock up to 2 GHz. The differential outputs from the clock generator were used to extract synchronous, 180 degrees phase shifted clock signals for the two DACs.

The signals presented here were captured using an Agilent 54855A Infiniium Scope, which operates at 20 GSa/s and has an analog bandwidth of 6 GHz. This is necessary in order to capture the sinc-weighted periodic repetitions of the spectra due to the zero-order hold function of the DACs. Due to the limited space here, we focus on the presentation of three examples for the TIDAC signal generation approach. The first one is a sinusoidal wave which has a frequency of 100 MHz. The differences of the samples are computed once and are then fed into the DACs. Since the sinusoid is a periodic wave, nothing has to be computed anymore and the samples can be read out forever. In Fig. 3.4 a scope screenshot of the two interleaved sinusoids is shown. Furthermore, the added signal, which was generated over a simple power combiner, is shown here as well.

In Fig. 3.5 the corresponding signal spectra are shown. The signal energies are normalized to 0 dB for visualization. For the single-channel DAC we see the sinc-weighted mirror images of the sinusoid in the spectrum. The next periodic repetition of the signal is already at double the sampling frequency, which is in our case at 1.6 GHz. If we use two DACs in interleaved mode, the spectral components at $f_s \pm f_0$ (i.e., $800 \text{ MHz} \pm 100 \text{ MHz}$) vanish and a similar behavior for a signal with twice the sampling frequency is seen in the

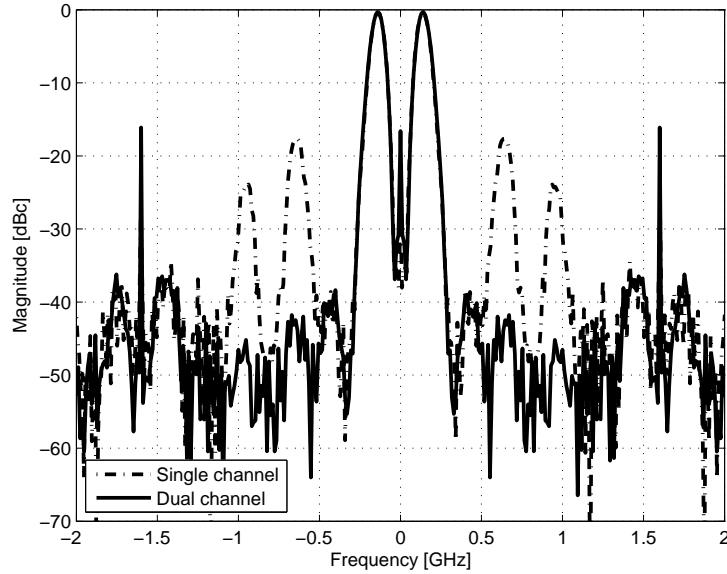


Figure 3.7.: Spectra for time interleaved fifth-order Gaussian pulses

spectrum. In our application a reduction of about 30 dB of these signal components is possible as our generated signal bandwidth is rather low. However, the mirror images for the combined signal are at $2f_s \pm f_0$ (i.e., $1.6 \text{ GHz} \pm 100 \text{ MHz}$). These copies are easily filtered by a low-complexity filter.

As a second example we used a fifth-order Gaussian UWB pulse to show that also broadband signal generation is possible with this structure. The pulse shape in the time domain is given as

$$w(t) = A \left(\frac{t^5}{\sqrt{2\pi}\sigma^{11}} + 10 \frac{t^3}{\sqrt{2\pi}\sigma^9} - 15 \frac{t}{\sqrt{2\pi}\sigma^7} \right) e^{\left(\frac{-t^2}{2\sigma^2}\right)}, \quad (3.14)$$

where σ is a width parameter of the pulse and was set to $\sigma = 5.1 \cdot 10^{-9}$. The polynomial coefficients in (3.14) are originating from the derivation of the conventional Gaussian bell shape. A fifth-order Gaussian is used because it fits the regulation requirements defined by the FCC [1]. Again, a scope screenshot of the differentially encoded signals and the sum of the signals is shown in Fig. 3.6. We see that each of the pulses already contains the shape of the resulting pulse. By time-shifted overlapping of the pulses all the interim values of a DAC running at the high clock rate are produced. Furthermore, the duration of the ZOH is halved. The spectra shown in Fig. 3.7 show also a good reduction of the mirror images around the sampling frequency.

As a third and last example the generation of a standardized OFDM signal with the TIDAC structure is shown. As specified in [15], the standardized MB-OFDM UWB signal consists of 128 carriers, where each of them, in the most general form, is modulated by QPSK data symbols. The DC and a few carriers at the band edges are nulled out to allow the design of analog filters for image rejection when the signal is generated via a DAC. The sampling rate of the signal is 528 MHz which results in a sub-carrier spacing of 4.125 MHz.

The bandwidth considering the occupied carriers is 503.25 MHz. If the DAC generates the I and Q component at a sampling rate of 528 MHz the spectrum of the generated signal will only have a very narrow region around half of the sampling frequency in which an analog front-end filter has to reject the mirror images caused by the periodic repetitions of the spectra. This makes the analog filter design not trivial. Furthermore, if the DAC is used up to half the sampling frequency, the sinc weighting of the desired signal is also visible and carriers close to half the sampling frequency are attenuated more than carriers at low frequencies. A generated I-phase signal of a standardized MB-OFDM UWB signal is shown in Fig. 3.8, where the previously described effects for a DAC operating at 528 MHz are clearly visible. Additionally, the spectrum of an OFDM signal, which was generated using the TIDAC structure is shown. It is clearly visible that simple filtering in the analog domain is possible since the mirrored images are shifted towards higher frequencies.

3.3. Compensation of Timing Offsets in TIDAC Structures

As seen in the previous section, we can generate arbitrary signals with DACs. By using signal processing in the digital domain, we can furthermore achieve that multiple DACs working in a converter array perform similarly as a DAC converter at a much higher conversion rate. Up to this point we have assumed that the M zero-order hold functions $h_m(t)$, of the DACs, employed in the converter array, are the same for all DACs. Now, the timing offsets between different converters within the TIDAC are considered in the model. In particular, an investigation of the compensation of distortions due to periodic nonuniform holding signals as illustrated in Fig. 3.9 is shown. The individual sample instants deviate by $r_m T_s$ from the ideal time instants nT_s , where T_s is the nominal sampling period of the DAC and r_m are M -periodic relative timing offsets. So the time index n is running from

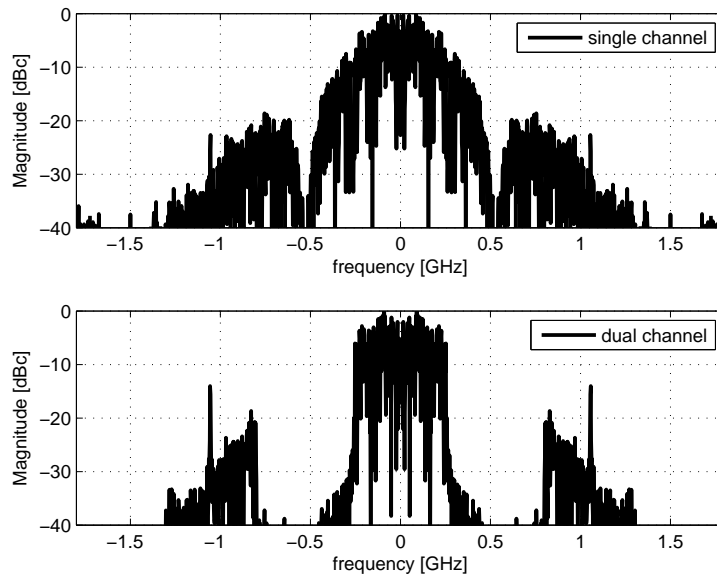


Figure 3.8.: Spectra for time interleaved OFDM

3.3. Compensation of Timing Offsets in TIDAC Structures

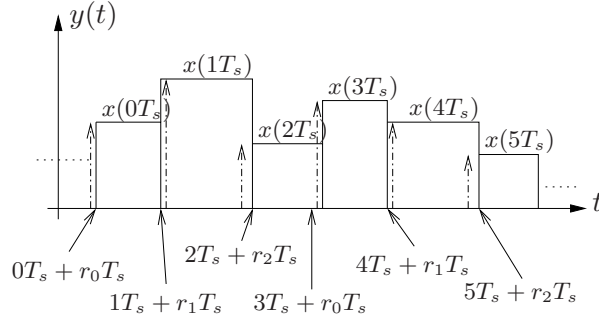


Figure 3.9.: Periodic nonuniform holding signal with period $M=3$. The dash-dotted arrows indicate the ideal sampling instants nT_s . The solid lines are the periodically shifted sampling instants $nT_s + r_m T_s$ that lead to the nonuniform holding signal.

$-\infty, \dots, \infty$ whereas the sample index within one period of mismatches $m = 0, \dots, M - 1$ which can be expressed as $m = n \bmod M$, \bmod denoting the modulo operator. Beside the typical $\sin(x)/x$ -shaped output spectrum, such holding signals introduce additional distortions reducing the DAC performance [60]. Furthermore, such a behavior is found in DACs driven by clock signals with deterministic jitter [61] and in time-interleaved DACs with timing mismatches [62, 63, 10].

To compensate the distortions caused by the nonuniform holding signals the design of a time-varying filter is presented. For the derivations and the filter design the relative timing offsets r_m are assumed to be known. Furthermore, no analog reconstruction filter which attenuates all out-of-band signal energy including the additional distortions of the nonuniform holding signals is considered.

3.3.1. System Model

The ZOH output of a DAC can be mathematically represented by an impulse train modulator $\sum_{n=-\infty}^{\infty} x(nT_s)\delta(t - nT_s)$, where $x(nT_s) = x[n]$, followed by a low-pass filter $h(t)$ [31]. The symbol T_s is the nominal sampling period and the hold time of the ZOH. In the uniform case, the impulse response of the low-pass filter $h(t)$ is one for the time T_s and zero for all other times. Contrary, in the periodic nonuniform case, the hold time T_s of the ZOH changes periodically over time as illustrated in Fig. 3.9. To be specific, for each nominal time instant nT_s we have a relative time offset of $r_m T_s$ resulting in a hold time of $(1 + r_{m+1} - r_m)T_s$. Mathematically, we can represent periodic nonuniform holding signals as [60, 64]

$$y(t) = \sum_{m=0}^{M-1} \sum_{n=-\infty}^{\infty} x((nM + m)T_s)h_m(t - (nM + m + r_m)T_s) \quad (3.15)$$

where the impulse responses of the low-pass filters are given by

$$h_m(t) = u(t) - u(t - (1 + r_{m+1} - r_m)T_s). \quad (3.16)$$

The relative timing offsets r_m are periodic with M , i.e., $r_m = r_{m+M}$ for all m . Applying the continuous-time Fourier transform (CTFT) to (3.15), we obtain [60]

$$Y(j\Omega) = \frac{1}{T_s} \sum_{k=-\infty}^{\infty} \check{H}_k(j\Omega) X \left(j \left(\Omega - k \frac{2\pi}{MT_s} \right) \right) \quad (3.17)$$

with

$$\check{H}_k(j\Omega) = \frac{1}{M} \sum_{m=0}^{M-1} H_m(j\Omega) e^{-jkm\frac{2\pi}{M}} \quad (3.18)$$

and

$$H_m(j\Omega) = \frac{2 \sin(\Omega(1 + r_{m+1} - r_m)\frac{T_s}{2})}{\Omega} e^{-j\Omega(1+r_{m+1}+r_m)\frac{T_s}{2}}. \quad (3.19)$$

Beside the well-known $\sin(x)/x$ shaped output spectrum, we have $M - 1$ additional mismatch spectra in the output. A comprehensive analysis of the impact on the signal-to-noise ratio is given in [60].

3.3.2. Proposed Compensation Filters

To compensate for the mismatch spectra, an M -periodic time-varying filter $g_n[l]$, which relates the input $\hat{x}[n]$ to the output $x[n]$ is used. For the two channel case, this problem can be solved in a matrix notation and the proposed pre-distortion filters can be expressed in frequency-domain as

$$G_0(e^{j\omega}) = \frac{2H_1(e^{j(\omega+\pi)})}{H_1(e^{j\omega})H_0(e^{j(\omega+\pi)}) + H_0(e^{j\omega})H_1(e^{j(\omega+\pi)})} e^{-j\omega\Delta}, \quad (3.20)$$

and

$$G_1(e^{j\omega}) = \frac{2H_0(e^{j(\omega+\pi)})}{H_1(e^{j\omega})H_0(e^{j(\omega+\pi)}) + H_0(e^{j\omega})H_1(e^{j(\omega+\pi)})} e^{-j\omega\Delta}, \quad (3.21)$$

where $G_1(e^{j\omega})$ and $G_2(e^{j\omega})$ are the compensation filters and $H_0(e^{j\omega})$ and $H_1(e^{j\omega})$ are the transfer functions of the ZOHs used in the structure. These final results have been presented in [48] with a detailed derivation and have been included in this thesis in Appendix E.

Measurement Results

For the already presented TIDAC, the compensation filters have been included in the signal generation path and mismatches have been compensated. For the presented measurements we have generated a single sinusoid with a frequency of 300 MHz and have identified the timing offsets as $r_0 = 0$ and $r_1 = 0.12$. With the identified timing offsets a filter has been designed according to (E.21) that compensates the digital signal as depicted in Fig. E.1(a). The digitally compensated and converted signal has been measured again with the high-speed sampling scope. The results of the measurements are shown in Fig. 3.10. The mirror images at 500 MHz have been reduced by about 20 dB. Due to uncertainties (i.e., the resolution of the scope) in the timing offset measurements, a better reduction has not been possible.

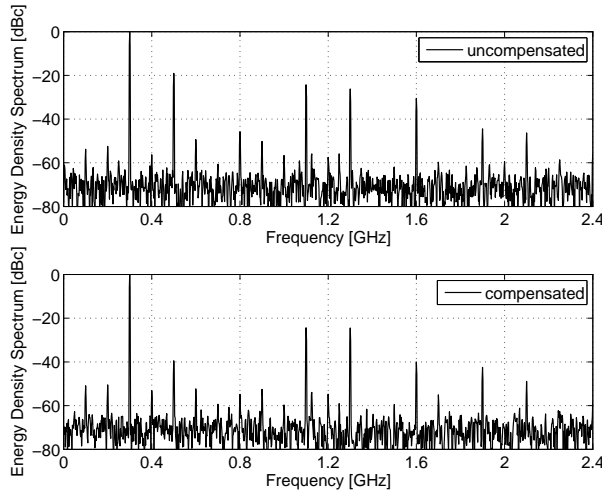


Figure 3.10.: Measurements for the uncompensated and the precompensated sinusoid with $f = 300$ MHz and sampling rate $f_s = 1600$ MS/s.

3.3.3. Timing Offset Identification

In the preceding discussion we have assumed that the timing offsets are known. In practice, we have to determine them from measurements. Since the identification of timing offsets will be a separate work of significant effort, we will only point out some principle approaches. To determine the timing offset we need an additional analog-to-digital converter (ADC) to observe the output. By observing the output of the DAC for special input signals, one can use (3.17)-(3.19) to identify the timing offset similar as it has been done for time-interleaved ADCs [65]. However, the accuracy requirements on the calibration signals seem to be challenging. For the case of two-periodic time-varying holding signals we can exploit the Farrow structure [66] for the filter design of $G_n(e^{j\omega})$. The impulse response of such filters can be changed by a single parameter, i.e., the timing offset, without redesigning the filter. This filter structure allows to adaptively find the timing offsets by minimizing the out-of-band energy without a calibration signal.

3.4. Standardized IEEE 802.15.4a Receiver Architectures

As we have seen in the two previous sections, the universal generation of UWB signals is a challenging task and can be achieved with a TIDAC to allow for low-complexity analog front-end circuitry. As already mentioned, any pulse which complies with the spectral masks specified by the regulation authorities (*cf.* Fig. 1.1) and has a certain similarity with a reference pulse defined in the standard can be used for a standardized system. The requirements identified for this standardized system were to provide localization of devices with accuracies below 1 m and simultaneously allow low-rate data transmission over the same physical link. In 2007, the IEEE 802.15 working group, and specifically the task group 4a, finalized their standardization document about an alternative UWB PHY and MAC layer [6]. One of the signaling schemes defined in the IEEE802.15.4a standard

considers transmitting data symbols by transmitting bursts of very short pulses. These pulses are combined in a burst consisting, for the mandatory data rates of a standardized device, of 16 pulses. The 3 dB bandwidth of UWB pulses is 499.2 MHz. The inverse of this bandwidth defines the chip time T_c which is app. 2 ns. Pulses which can be used for a standardized scheme are defined with respect to their correlation properties to a well-defined reference pulse. This reference pulse is a root raised cosine pulse as defined already in (3.1). In the beginning of this section we want to summarize the signaling scheme defined in the standardization document [6]. We will see that the standard employs a time division multiple access (TDMA) signaling scheme where the signals are modulated in amplitude and position. This allows two different kinds of receivers, namely coherent and non-coherent receivers, where both types can detect the bit encoded in the position but the other bit encoded in the polarity is only a meaningful information for coherent receivers. We will see three different types of receivers, one coherent and two non-coherent ones, which have similar implementation complexity. We compare these receivers in single and multi-user communication scenarios. The three receivers are compared according to their bit error ratio (BER) performance in these environments.

3.4.1. Standardized Signaling Scheme

As already mentioned, the standardized IEEE802.15.4a signal consists of broadband pulses with a bandwidth of 499.2 MHz. To be precise, for the mandatory data rate of 1 Mbps, 16 pulses are combined to a burst of pulses which are sent consecutively. These pulses are then pseudorandomly flipped in their sign to achieve spectral smoothing. For the optional data rates defined in the standard, also other burst lengths are defined. We refer the interested reader to [6] and focus on the mandatory systems in this work. Furthermore, these pulses are modulated with binary phase shift keying (BPSK) and with pulse position (PPM). To be specific, the whole burst of pulses is modulated in position, thus the modulation is called burst position modulation (BPM). For that reason, a signaling frame has been defined in the standard which is shown in Fig. 3.11. One can see quickly that such a data symbol consists of two slots where data pulses can occur (labeled with “possible burst positions”). After one of these regions where a device is able to transmit data, two guard intervals have been included into the frames. This keeps the interference of the UWB systems to other existing systems low and allows to design power efficient devices which can switch off certain parts of the receiver during these idle times. In each of these possible burst position frames, there are 8 (mandatory) subslots where one of these bursts can be placed in a pseudo-random manner. The hopping sequence is derived from a linear feedback shift register (LFSR) which also determines the polarity code for the pulses within a burst.

The transmitted signal $x_k(t)$ can be expressed for one symbol k by

$$x_k(t) = (1 - 2g_1(k)) \sum_{n=1}^{N_{cpb}} (1 - 2b_n(k)) p(t - g_0(k)T_{BPM} - h(k)T_{burst} - nT_c), \quad (3.22)$$

where $g_0(k)$ and $g_1(k)$ are the two data bits, $b_n(k)$ is the pseudo random, time-varying code for pulse polarities, $h(k)$ is the hopping sequence within the possible burst positions, and $p(t)$ is the transmitted pulse shape, respectively. N_{cpb} is the number of chips per

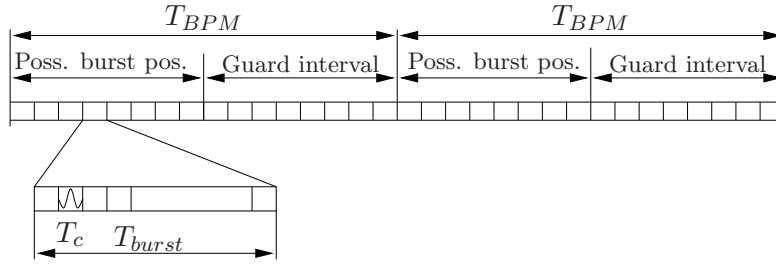


Figure 3.11.: Framing structure of one data symbol in the IEEE802.15.4a standard

#Burst pos. per symbol	#Hop bursts	#Chips per burst	#Chips per symbol	Burst duration	Symbol duration
N_{burst}	N_{hop}	N_{cpb}	-	T_{burst}	T_{sym}
				ns	ns
32	8	16	512	32.05	1025.64

Table 3.1.: Summary of symbol timing for mandatory data rate in IEEE802.15.4a

burst and $T_{burst} = N_{cpb}T_c$, i.e., an integer multiple of the chip time T_c . Please note that the transmitted pulse shape has to fulfill certain correlation requirements to the reference pulse shape defined in (3.1) [6]. For the mandatory symbol rate of 1 Mbps we have summarized the timing parameters for one symbol in Table 3.1.

3.4.2. Receiver Architectures

In this subsection we want to focus on three receiver structures which, we think, are feasible for receiving standardized UWB signals from an implementation point of view. There are many other receivers possible but most of them cannot be considered as low complexity receivers. Due to the special structure of the transmitted signal, coherent receivers are able to detect both bits ($g_0(k)$ and $g_1(k)$) encoded in the transmitted signal. Non-coherent receivers are only able to detect whether the received energy is either in the first or second part of the transmitted symbol. On the other hand the receiver circuitry is much simpler for non-coherent receivers because a complex channel estimation can be omitted. In the following we want to consider three different receivers, namely a Rake receiver (coherent), an energy detector (ED) and a modified transmitted reference (TR) receiver. From the implementation point of view, the complexity of an All-Rake receiver is much higher than the one of the non-coherent receivers but if the number of fingers is set to a very small value, the implementation complexity is reasonable and the comparison to the non-coherent receivers makes sense.

One-finger Rake Receiver

Generally, UWB signals are spread in time when they are propagated over a wireless multipath propagation channel. For a UWB channel, the channel impulse response can be quite dense if we consider a harsh environment with a lot of multipath components (see Appendix C). Time-shifted and attenuated replicas of the transmitted signal $x_k(t)$ will

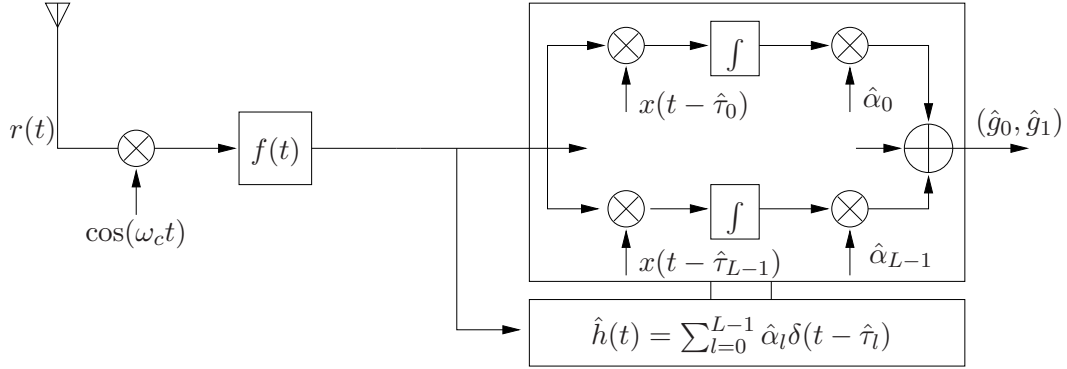


Figure 3.12.: Rake Receiver for UWB signals

arrive over time. The channel impulse response can be described in the most general case as

$$h(t) = \sum_{l=0}^{L-1} \alpha_l \delta(t - \tau_l), \quad (3.23)$$

where α_l denotes the path gains, τ_l denotes the delays of the multipath components and δ is the Dirac delta function, respectively. For modeling of the channel impulse response, a finite number of paths L are taken into consideration. An A-Rake (All-Rake) receiver would now (as depicted in Fig. 3.12) perform channel estimation, i.e., obtain a correlation template $\hat{h}(t)$ and correlate each arrived multipath component with a matched time-shifted and attenuated copy of a locally generated transmitted signal taking into consideration the pseudorandom spreading sequence $b_n(k)$. The outputs of each correlator can then be combined (usually in a maximum ratio combining (MRC) sense) to give the decision statistic for the transmitted data symbol (in our specific case the data pair (\hat{g}_0, \hat{g}_1)).

To be able to capture all the energy of the transmitted signal, for each distinct multipath component (MPC) of the wireless propagation channel one such correlator branch as depicted in Fig. 3.12 is necessary. If all MPCs are used the Rake receiver is called an *optimal* receiver because all the energy from the transmitted signal is collected at the receiver side. Corresponding to its superior performance, one drawback of a conventional Rake receiver is that its implementation complexity is huge. Firstly, channel estimation has to be done to have sets of gains and delays to correlate with, which might not be easy. Secondly, for each estimated multipath component a correlator has to be used with an accurate time shifted version of the pulse shape and an accurate path gain. If the number of multipath components is big, which is usually the case for UWB channels, L is in the order of hundreds which is not feasible. One could think of a reduced number of fingers by selecting just a few strongest path for the rake receiver which is usually then called S-Rake (Selective Rake) receiver [67, 68]. However, current literature still reports numbers of 40 to 60 fingers to achieve reasonable performance.

In our further considerations the Rake receiver should serve as a reference for the non-coherent schemes proposed afterwards. For that reason, a Rake employing only **one** finger is used. This seems, from an implementation point of view as a low-complexity scheme and allows comparison to the other proposed receivers in this section.

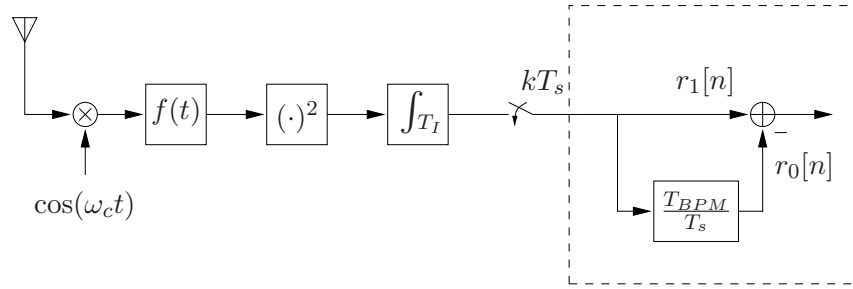


Figure 3.13.: Energy Detector for standardized UWB communication

Energy Detector

The second receiver under investigation is a very simple receiver. An energy detector [69, 70] is probably the most simple solution to achieve non-coherent detection of the information bits $g_0(k)$ contained in the standardized signal stream for UWB devices. As depicted in Fig. 3.13, after downconversion of the signal and filtering of out-of-band signals by $f(t)$, the signal is fed into a square-law device. From an implementation point of view this circuitry can be very easily realized by a (Schottky) diode. The output of the square-law device is then fed into an integrator, where the energy content is accumulated over the integration interval T_I . The integration interval is set to the burst time, to be able to distinguish the energy contents in the individual slots from the proposed TDMA scheme. The integrator is realized in a very simple way by loading a capacitor and having a parallel switch to dump the integrator. One could also think of sampling the output at higher rate, i.e., decreasing T_s but this requires a more complex ADC in the backend of the receiver. If we assume signal energy is just contained in either half of the overall symbol, one could use a fixed delay of time T_{BPM}/T_s in the digital domain to compare the hopping slots in the two halves, i.e., comparing the variables $r_0[n]$ and $r_1[n]$ in the digital domain (cf. Fig. 3.13).

Transmitted Reference Receivers

Transmitted reference (TR) signaling has been proposed already in the 1960s for wideband data transmission [71]. The idea behind this signaling scheme is that two pulses are transmitted. One of them is a reference pulse and performs channel estimation and the other one is modulated by data. Because of the short duration between the two pulses, they encounter the same channel and can be correlated easily by an autocorrelation receiver. Additionally to the BPSK modulation modifying the sign of the pulses, a second data bit could be encoded in the pulse position. However, if we stick to the standardized scheme, this pulse position modulation is not possible since one burst has constant distance between the pulses (app. 2 ns). As proposed by different authors, a BPSK modulation of the transmitted data can also be done if the pulse polarities of the transmitted pulses are encoded differentially [72, 11, 73] to cite just a few. Since this polarity code is also fixed within the standardized transmission, this is not possible within the boundaries of IEEE 802.15.4a. Furthermore, the number of pulses for the transmitted reference scheme is far too high in that case. If a frame-differential scheme like in [74] is considered, this would

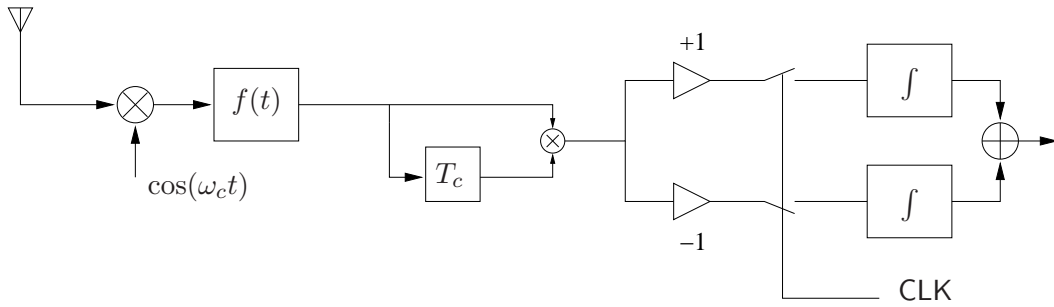


Figure 3.14.: Newly proposed TR receiver

require 15 delays to correlate each pulse pair which is, from an implementation point of view far too complex. Manufacturing a delay-line of 2 ns for a bandwidth of 500 MHz is feasible, 15 of them are an overkill and would consume a lot of chip area. Furthermore, the delays should have different length. If each second pulse is considered to be a reference pulse (like in [75]) the number of integrators would reduce and a chain of delays can be used. However, 15 delay lines are not feasible and since the symbol polarity is not encoded differentially, the extra effort of spending more delays does not help to detect the symbol amplitudes as in the frame-differential TR scheme. Thus, the conventional idea of using a TR scheme is simply not realizable for standardized IEEE 802.15.4a communication systems. There are mainly two reasons for that, i.e., (a) the channel's delay spread is much larger than the pulse separation, causing severe inter-pulse interference (IPI) and (b) the number of delay lines would be too high to implement it on a chip.

After this first analysis of the signaling scheme, using transmitted reference for standardized UWB schemes is ruled out. However, we have found a solution which might work very well, is just slightly more complex than a plain energy detector and should have superior performance to the energy detector when operating in a multiple user scenario. The proposed receiver is depicted in Fig. 3.14. It represents a compromise between the complexity of a Rake receiver where many fingers have to be used and the very simple scheme of an energy detector which will suffer in an introduced MUI scenario when symbols are spread into other possible burst position slots by the channel. Furthermore, the implementation complexity of that receiver stays bounded and all components are realizable.

The idea behind the newly proposed receiver is to exploit the fact, that all pulses are just separated by the same chip time T_c which is app. 2 ns. In that case, the implementation complexity drops from 15 delay lines to one single delay line of 2 ns which can be implemented quite accurately. By delaying the symbol by just one chip time, the symbol should be mostly correlated with itself except for a remaining spreading code. Since the spreading codes defined in the standardization document [6] are pseudorandom but fixed the despreading can be precomputed. In the receiver, these polarities are available and are used for switching the polarities of the multipliers output. The precomputed despreading sequence is computed as follows. The symbol is encoded with the polarity vector $\mathbf{b}[n] = [b_0, b_1, \dots, b_{N_{cpb}-1}]$. This vector has to be extended and shifted to be able to compute the despreading vector, i.e.,

$$[\mathbf{b}[n], 0] \odot [0, \mathbf{b}[n]] = [0, b_1 b_0, b_2 b_1, \dots, 0], \quad (3.24)$$

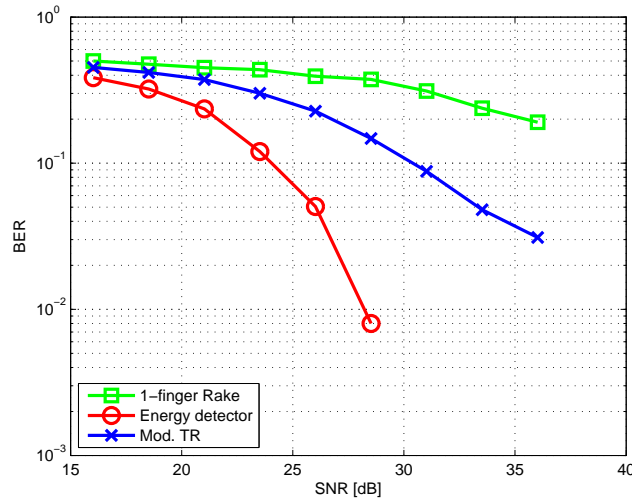


Figure 3.15.: Comparison single user communication LOS

which gives a vector containing zeros and plus/minus ones, the symbol \odot denotes element-wise multiplication. To despread the signal it is passed through multipliers (+1/-1) before it is integrated. Since the output of the mixer is generally a differential signal, we get these two signals from the mixer for free. Now we just have to use the switches which should alternately (according to the despreading sequence) switch between the two integrators. This means, that either one of the integrators is cumulating energy. In the end, these two outputs can be summed up and provide a decision variable for a detector. It is expected that this novel modified TR receiver architecture shows superior performance over the ED in a multiuser scenario because not all the code information is lost in the square-law device and despreading can be done with respect to a specific user.

3.4.3. Receiver Comparison

To compare the performance of the different receivers computer simulations for single-user and multi-user environments have been carried out. Furthermore LOS and NLOS environments are distinguished. For that reason we used measured UWB channel impulse responses from a measurement campaign carried out at the Swiss Federal Institute of Technology in Zurich, where impulse responses in a Lobby were measured [76]. In these measurement data, LOS and NLOS channel responses were provided in the frequency domain and have been transformed into time-domain for further processing. For the simulation of the performance, the standardized framing structure has been implemented in MATLAB and the performance for single user and multiple user scenarios has been evaluated. In the first scenario a single user case with a LOS channel has been evaluated. One can imagine this scenario to appear in a sensor network environment, where simple tags have to be identified. One can see (*cf.* Fig. 3.15) that the simple energy detector performs best in this environment. However, the performance of the modified TR is also reasonable in high SNR regions. For the definition of the SNR, a similar approach as

shown in [69] was used. The received energy E_r of the data symbol is given as

$$E_r = E_t \int (x(t) * h(t))^2 dt, \quad (3.25)$$

where E_t is the energy of the transmitted pulse, $x(t)$ is the transmitted burst, and $h(t)$ is the channel impulse response, respectively. The $*$ operator represents the linear convolution of the two signals. Furthermore, a path gain is defined as $\alpha^2 = E_r/E_t = \int [x(t) * h(t)]^2 dt$ and for the simulations normalized channel impulse responses have been used, i.e., $\bar{h}(t) = h(t)/\alpha$. The noise is generated from a zero-mean Gaussian noise process with a two-sided PSD of $N_0/2$.

One problem with the one-finger rake receiver is its high sensitivity to synchronization. If the receiver is not accurately synchronized to the maximum path (and only this one is used for the studied receiver) of the channel the performance quickly degrades. To make the receiver performance independent of the channel estimation, which has to be performed in a real receiver, the (strongest path of the) channel is assumed to be known for the simulations.

In the NLOS scenario (Fig. 3.16) we see a similar performance of the two non-coherent receivers. This is clear, when we remember how these two receivers work in detail. They actually try to collect all the energy which is spread from the transmitted signal over all different multipaths occurring in the channel. If all the energy can be collected properly, the performance of the system in LOS and NLOS channels in terms of BER is the same. The already mentioned synchronization issue for these receivers is affecting the performance much more in NLOS scenarios. The performance of the 1-finger rake receiver is really poor due to the missing strong component to synchronize. Also the power of the second strongest path in the NLOS case is much lower than in the LOS case which is reducing the SNR.

For the multi-user (MU) scenario we have set up the same TDMA framing structure as described in the standard, see Table 3.1. By using a pseudorandom number, the selection

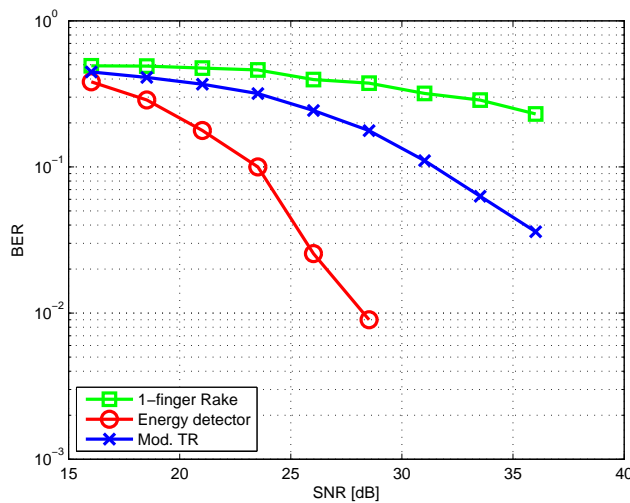


Figure 3.16.: Comparison single user communication NLOS

3.4. Standardized IEEE 802.15.4a Receiver Architectures

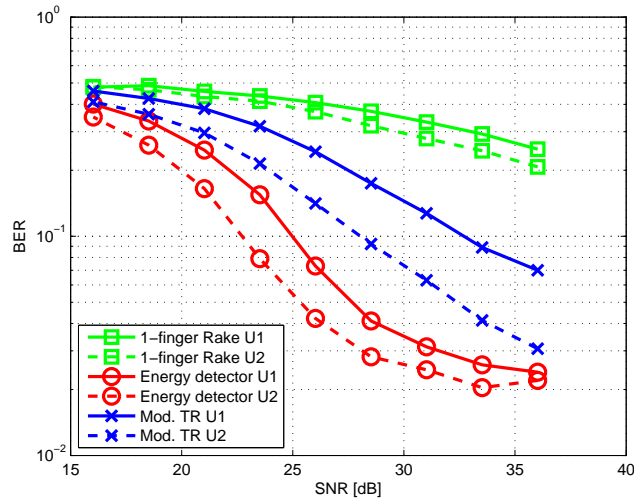


Figure 3.17.: Comparison dual user communication LOS

of the hopping position is done, and it is assured that no timeslot is filled twice in an MU scenario. As one can see by looking at the simulation results depicted in Fig. 3.17, the simple energy detector suffers in MU environments because no selection of the user in the physical layer can be done. Thus simple comparison of the two signal halves is not enough to detect the data. This results in a flattening of the BER curves (similarly visible for the LOS and NLOS case, *cf.* Fig. 3.17 and Fig. 3.18, respectively) which is not present at high SNR for the modified TR receiver. For the rake receiver, this MU interference from the other transmitter has generally no influence on the performance because due to the estimation of the channel, the two transmitters can be distinguished

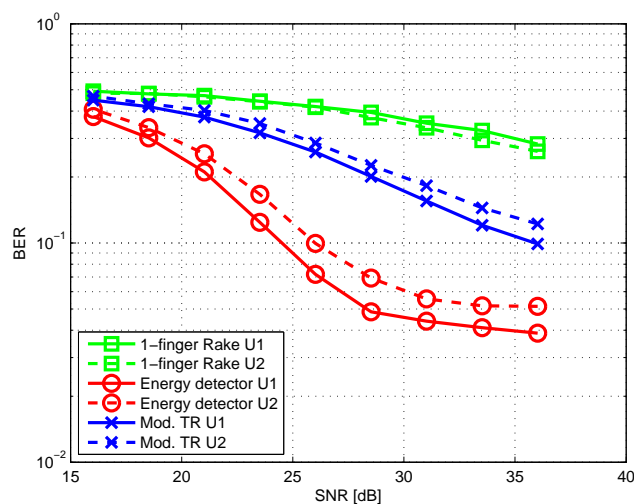


Figure 3.18.: Comparison dual user communication NLOS

and the crosscorrelation of the templates with the received signal from the second user is low. However, still the performance of a one-finger rake on the energy in the first path which is very low considering that much energy is contained in the multipath components.

In a single-user environment, it is seen that the very simple energy detector can achieve the expected results of better performance when increasing the SNR. However, if multiple users are transmitting in this TDMA scheme, the interference results in a BER floor for the ED. Now, the advantage of the modified TR receiver is present when we look at the BER results. Due to the despreading of the pulse polarity code in the receiver, it is still possible to achieve a good performance for high SNR regions. The two users can, with this simple switching method, be distinguished properly and the performance of the new receiver is reasonable at high SNRs and no BER floor is observed.

3.5. Conclusions

In this chapter we have discussed some of the challenges occurring when designing pulse based UWB radios. Generally, many different pulse shapes can be used in UWB communication systems. Thus, using a DAC to generate the desired pulses is one way to have a flexible pulse generator. One challenge in using a single DAC for signal generation is certainly, that the bandwidth of that DAC is limited. This limitation can be overcome by using multiple converters in an array, each of them operating with a phase shifted clock signal. On one hand this extends the bandwidth of the DAC or allows for simple analog filtering at the front-ends. This converter array, called TIDAC, has been used for UWB signal generation. To generate the signals properly, a differential encoding of DAC outputs has to be done. This can be achieved by computing a filter in the digital domain, i.e. modifying the equations for conventional signal generation. The equivalence of the TIDAC and a DAC running at a higher clock rate in time and frequency domain have been demonstrated analytically and with measurements. Compared to the single-channel case, a reduction of mirror images occurring at $f_s/2$ by about 30 dB has been achieved for both narrow band signals and wideband signals. This relaxes the requirements of the analog interpolation filter dramatically, provided that the settling time of the DACs is high enough.

In a first step we have assumed that all the converters in the array are described by the same transfer function. If timing offsets between the converters occur, a time-varying filter can be used to compensate for these mismatches. The occurring distortions are assumed to be M -periodic, and degrade the performance of the converter array. The mismatch spectra can be expressed analytically, and when the mismatches are known, compensation filters for an M -channel TIDAC converter array can be designed. We have presented the design procedure for a two-periodic time-varying compensation filter and have shown a simulation example that reduces the in-band distortions by about 31 dB. As the simulations have further shown, the out-of-band energy is slightly increased by the compensation filter, which will not be an issue in most applications. Nevertheless, the out-of-band behavior of the compensation filter can be incorporated in future filter designs. For our considerations, we have assumed that the timing offsets are known and are time-invariant, but in practice they will change over time and the compensation filter has to be adjusted to the time-varying behavior of the mismatches. Therefore, the filter

design has to be extended to allow for time-varying timing offsets.

Finally, also the receiver side has been investigated. Possible receiver structures for standardized UWB low data rate communication and positioning systems [6] have been presented. It is seen that, from an implementation complexity point of view, an energy detector offers the most simple solution. On the other hand, the MU performance of the ED is not very good and a novel modified TR receiver has been proposed for the standardized, pulse based UWB communication scheme. With slightly increased complexity for the modified TR scheme, a superior MU performance can be achieved whereas the ED does not consider the additional information contained in the spreading code. A very simple rake receiver has been compared in this study too, but due to relying on a single path, reliable synchronization, and the loss of energy due to the multipath environment, the rake receivers a bad choice for a low-complexity and low-cost implementation.

Chapter 3. Pulse-Based UWB Communication

Equalization for Nonlinear Receiver Front-Ends

In this chapter we will review one very specific UWB communication system. It is basically an extension of the conventional pulse-based transmitted reference idea proposed already in the 1960's and generalized in 2002 [77] when UWB got the boost because of the regulation authorities' release of the spectrum in the US [1]. As already seen in Section 3.4, the simple receivers which can be used for the standardized pulse based UWB scheme can also be used for TR signaling. One big advantage of correlation receivers is their easy implementation. Conversely, these receiver architectures have one main drawback, namely that they employ nonlinear devices to be able to restore the original signal. This introduces new challenges for the signal processing algorithms in the receivers and requires digital enhancement of the effects occurring in the continuous-time domain.

This digital enhancement of the analog front-end of the receiver will be the main scientific contribution of this chapter. In the beginning we will briefly review the results from [11], with respect to the used signaling scheme and the used receiver structure. Furthermore, a nonlinear equivalent system model can be derived from the studied communication system which will be briefly discussed in this section. The overall system can be modeled as a second-order Volterra system when high data rates are used, i.e., a nonlinear system with fading memory. The nonlinear distortion can be equalized by means of digital signal processing which will be elaborated in the following sections¹.

4.1. Introduction

It was shown in Section 3.4 that receivers for pulse-based UWB communication can be implemented with a few simple components. If we reconsider the ED, we have also seen that this is achieved with a simple squaring device (i.e., a nonlinearity). Also if we consider the transmitted-reference signaling schemes as described in [77, 11, 72, 79] and the corresponding autocorrelation receiver architectures, we see that the essential receiver operation is nonlinear. As discussed in Sect. 3.4, the idea of transmitted-reference signaling is to transmit pairs of pulses. The first pulse is an unmodulated reference pulse and serves as a template for the second transmitted pulse. The second pulse, i.e., the data pulse, is then modulated either in polarity or in delay. So for each transmitted bit, one such

¹Main parts of this chapter are taken from a journal contribution submitted by the author [78].

pulse doublet (frame) has to be transmitted. Since the separation between these pulses is usually small ($\sim 2 - 30$ ns) both pulses encounter the same distortion on the channel, and the reference pulse is thus a perfect template to measure the similarity to the transmitted data pulse (i.e., determining the correlation). Thus, the receiver operates directly in base-band and receives the signal with a broadband antenna. This received signal $\hat{r}(t)$ is then fed into a pulse-pair correlator which consists of a delay line, matched to the distance of the pulses in the transmitted signal, and a multiplier performing the multiplication of the received signal with a time-shifted copy of itself. Afterwards, the signal of the multiplier is cumulated (integrated) over a certain time T_I , to capture sufficient multipath energy from the transmitted pulses. This integration time is usually found by trading cumulation of signal energy and cumulation of noise [80]. The output of such a correlator is then sampled and digital post-processing can be done in a DSP or FPGA chip. The digital part of the receiver can then also achieve synchronization of the receiver to the transmitter and within a feedback loop, the integrator delays are adjusted dynamically. One main advantage of this architecture is that in the receiver no channel estimation has to be performed.

One main drawback of the conventional transmitted-reference signaling scheme is, that only each second transmitted pulse contains new information. To support multi-user separation and increase robustness to interference, generally one such data symbol does not consist of a single pulse pair, only. Multiple pulse-pairs normally comprise one data symbol. This also means, that half of the transmitted symbol energy is already spent for the reference pulses. One solution to this loss of energy is to use each pulse in a data symbol as a reference and as a data pulse [72]. Additionally, the information bit can be differentially encoded into this pulse stream, meaning the current pulse polarity depends on the polarity of the previous pulse and the current data symbol. One such autocorrelation receiver for N_{cr} pulses composing one symbol is depicted in Fig. 4.1. The received signal is fed into a bank of correlators where each correlator has a matched time delay \tilde{D}_j , $j = 0, \dots, N_{cr}$ which is matched to the pulse delays in the transmitted pulse stream. Each pulse pair thus requires one correlator and the outputs of these correlators are then sampled at Nyquist rate. The digital signal processing used in the back-end can then get rid of nonlinear distortions in the received data symbols (one topic addressed in this thesis), narrow band interference (NBI) [12], and multi-user interference (MUI) [81,13]. Reduction of the nonlinear distortion can also be achieved by using oversampling in the receiver front-end. This was extensively studied in [79].

When increasing the data rate, the distance between these pulses becomes smaller. This is on the one hand desired because then the correlation of the channel's responses to the pulses is very high and requires short delay lines which can be implemented. On the other hand closely-spaced pulses, which are spread over the channel in delay, are also interfering with each other and are diminishing the performance of the system. Anyhow, there is high interest to find algorithms to reconstruct this information in a cheap way. Thus, the problems occurring with nonlinearities in the analog domain are compensated for by means of nonlinear digital signal processing which offers a cheap and flexible way to combat these distortions.

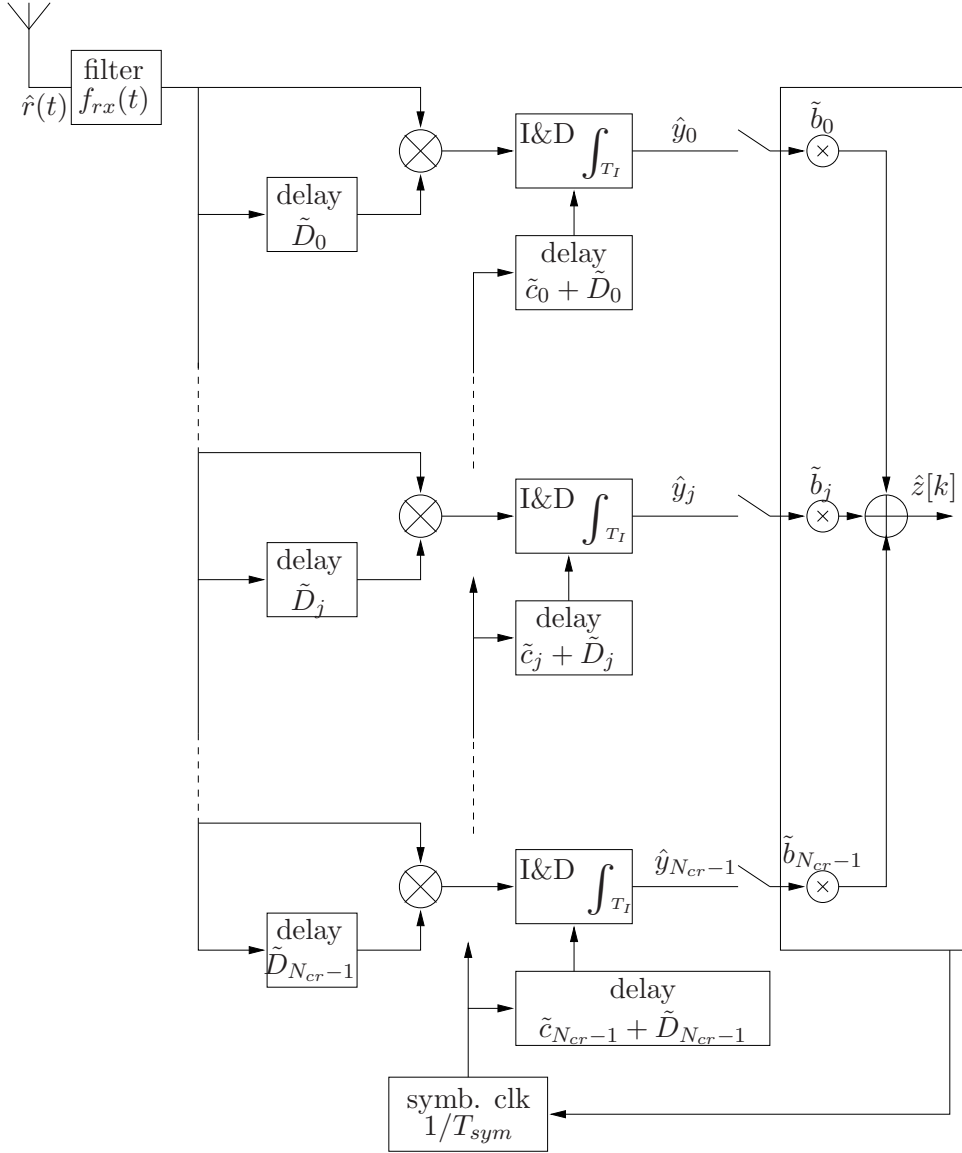


Figure 4.1.: Frame-differential receiver front-end

4.2. Equivalent Nonlinear System Model

The receiver front-end for such a non-coherent pulse based UWB receiver shows nonlinear behavior. Thus, if we assume that the system outputs are observed in the discrete-time domain, a system model can be derived, which contains system parameters of the receiver front-end, the wireless propagation channel, and the signaling scheme. The multipliers of the receiver front-end are easily identified as the source of the nonlinear behavior of the system. Such a nonlinear source can have a rather complicated function to describe its input-output relation. Generally, this function can be known exactly by an analytical expression or can be approximated by means of Taylor series, neural networks [82], and many other modeling approaches. The nonlinear equivalent system model we are going

to use in our further considerations also models the effects of the wireless propagation channel. This channel can, in its most general form, be described by a continuous-time impulse response $h_c(t)$ collecting all multipath components. If the channel's memory is included in the model, one can develop equivalent nonlinear fading memory systems and use Volterra models to describe their input-output behavior [83], [84]. This approach is used in many applications for nonlinear system description. Examples of nonlinear Volterra system modeling are presented in [85] where nonlinear magnetic recording channels are modeled, in [86] where nonlinear digital satellite channels are modeled, and [11] where the authors have shown that nonlinear Volterra modeling is also possible for non-coherent Ultra Wide-Band (UWB) receiver front-ends. Many more applications can be found where Volterra modeling is successfully applied, see e.g. [87, 88, 89].

4.2.1. Volterra Models

In this thesis, we extend the conventional linear MMSE equalizer to nonlinear, second-order Volterra systems. Generally, nonlinear fading-memory systems are described by a set of kernels, i.e., characterizing the nonlinear input-output behavior of the system. The output of a discrete-time, q -th-order time-invariant Volterra system with input $d[k]$ is given by

$$\begin{aligned}
 z[k] = & h_0 + \sum_{n_1=0}^{N_1-1} h_1[n_1]d[k-n_1] \\
 & + \sum_{n_1=0}^{N_2-1} \sum_{n_2=0}^{N_2-1} h_2[n_1, n_2]d[k-n_1]d[k-n_2] \\
 & + \dots + \sum_{n_1=0}^{N_q-1} \dots \sum_{n_q=0}^{N_q-1} h_q[n_1, \dots, n_q] \prod_{i=1}^q d[k-n_i]
 \end{aligned} \tag{4.1}$$

where h_0 and h_1 represent the bias and linear part, respectively. All higher-order kernels are given as $h_i, i = 2, \dots, q$. Each of the multidimensional objects h_i has, in its most general form, independent memory depths $N_i, i = 1, \dots, q$. The data sequence $d[k]$ represents data symbols with an arbitrary modulation format.

4.2.2. Simplified Nonlinear System Model

As seen in (4.1), the output of a fading-memory nonlinear system can be considered as a generalization of the linear convolution. This extension is obtained by including nonlinear terms in this convolution, i.e., by using all product terms for different time lags up to a certain memory depth. For the special case of a second-order system, i.e., $h_q = 0, \forall q > 2$, we can write the output of the Volterra system in a matrix-vector form as

$$z[k] = h_0 + \mathbf{h}_1^T \mathbf{d}[k] + \mathbf{d}^T[k] \mathbf{H}_2 \mathbf{d}[k] + n[k], \tag{4.2}$$

where $n[k]$ is the additive noise, $\mathbf{d}[k] = [d[k], d[k-1], \dots, d[k-L+1]]^T$ is a vector containing the L data symbols, and where the scalar h_0 , the $L \times 1$ vector \mathbf{h}_1 , and the $L \times L$ upper triangular matrix \mathbf{H}_2 are the zeroth-, first- and second-order kernels of the

4.3. Nonlinear Equalization for Second-Order Volterra Systems

channel, respectively. With respect to (4.1), the memory depth of the nonlinear system is defined as $L = \max(N_1, N_2)$. We make the following assumptions in this work:

- A1)** The data symbols $d[k]$ are binary antipodal, i.e., $d[k] \in \{\pm c\}$, with $c \in \mathbb{R}$ and $\pm c$ is equiprobable such that $\mathbb{E}\{d[k]\}=0$.
- A2)** The noise is i.i.d. Gaussian with zero-mean and variance σ_n^2 .

The derivations in this thesis can also be done without the i.i.d. assumption. However, the covariance matrices introduced later on will not be scaled identity matrices anymore. The squared elements of $\mathbf{d}[k]$ are given as $d^2[k] = c^2$, $\forall k$, and thus the main diagonal of the second-order kernel \mathbf{H}_2 can be included into the bias term h_0 which simplifies (4.2).

For our further considerations, we assume that the bias term is not contained in the system and we define

$$y[k] = z[k] - h_0 = \mathbf{h}_1^T \mathbf{d}[k] + \mathbf{d}^T[k] \mathbf{H}_2 \mathbf{d}[k] + n[k], \quad (4.3)$$

as the received sequence without the bias h_0 which can easily be obtained by averaging.

Since we want to write the second-order kernel as a linear function of the crossterms, we introduce the operator \boxtimes , which is a modified Kronecker product that only takes the unique half of the crossterms into account. We can then rewrite $y[k]$ as

$$y[k] = \mathbf{h}_1^T \mathbf{d}[k] + \mathbf{h}_2^T (\mathbf{d}[k] \boxtimes \mathbf{d}[k]) + n[k], \quad (4.4)$$

where \mathbf{h}_2 is an appropriate modification of \mathbf{H}_2 , omitting also the main diagonal elements since they have been collected in the bias term. For a vector $\mathbf{b} = [b_1, b_2, \dots, b_K]^T$, we define the reduced Kronecker product $\mathbf{b} \boxtimes \mathbf{b}$ as $\mathbf{b} \boxtimes \mathbf{b} = [b_1 b_2, b_2 b_3, \dots, b_{K-1} b_K, b_1 b_3, \dots, b_{K-2} b_K, \dots, b_1 b_{K-1}, b_2 b_K, b_1 b_K]^T$.

4.3. Nonlinear Equalization for Second-Order Volterra Systems

To recover the originally transmitted information, an equalizer has to be used to combat the distortion effects of the channel. For strictly linear systems, many different equalization strategies may be used. The most commonly known are Zero-Forcing (ZF) equalizers, Minimum Mean Squared Error (MMSE) equalizers, Maximum Likelihood (ML) equalizers, and Minimum Bit Error Rate (MBER) equalizers [90]. For linear Finite Impulse Response (FIR) channels the definition of an exact inverse is given by replacing all the zeros of the channel transfer function by poles, thus leading to Infinite Impulse Response (IIR) filters. A minimum-phase requirement on the channel is thus implicitly assumed to be able to create a stable and causal ZF equalizer [31]. Any occurring noise in the overall system is amplified by a possible gain of the ZF equalizer, making it less usefull for many implementations.

Another possibility to compute an equalizer is to minimize the mean squared error over a block of data symbols. Usually the error is then defined as the difference between the originally transmitted data symbols and the estimated data symbols, i.e., the received data symbols processed by an equalizer. Thus, the formulation of the overall system is necessary, i.e., the combined response of the channel and the equalizer. For purely linear systems, the MMSE equalizer is easily derived and can be found in textbooks [91], [36].

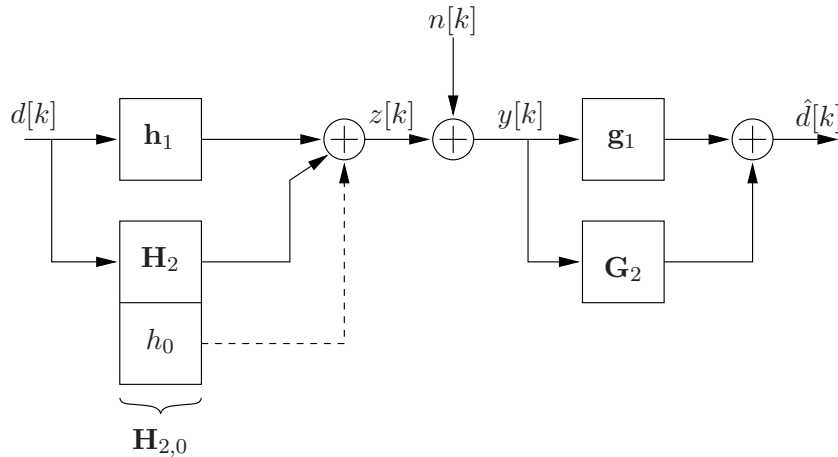


Figure 4.2.: Equivalent system model and proposed nonlinear equalization.

Generally, an equalizer for a nonlinear Volterra system can be computed exactly as a recursive Volterra system as shown in [92]. However, due to the recursive structure, the inverse system may encounter stability problems when applying signals with low SNR [93]. Conversely to the exact inverse, a ZF Volterra equalizer can be found by expressing the cascade of the Volterra channel and Volterra equalizer in terms of the orders of the input signal and equating equal exponents. This is conventionally known as the p -th-order inverse of nonlinear systems [94]. Up to an order of p all the nonlinear kernels of the cascade are forced to be zero. By introducing a nonlinear equalizer, higher-order terms (larger than p) occur in the cascade, which are nonzero and are assumed to be small such that their influence is negligible. However, exact inverses as well as p -th-order inverses require that the first-order kernel of the channel is minimum-phase because an exact inverse of the linear part is needed.

In [95], linear equalizers are proposed to achieve equalization of a nonlinear Volterra system. Such an equalizer requires oversampling at the receiver front-end increasing the complexity significantly. Still, it has been applied successfully to oversampled nonlinear receiver front-ends in [96]. In other works, the equalization problem has been formulated as a fixed-point problem [97, 98] where a solution for the equalizer is found iteratively. This is possible as long as the mapping between the iteration steps is contractive. An effective implementation of an adaptive equalizer in the frequency-domain is found in [99] where fast block convolution algorithms are used to combat Inter-Symbol Interference (ISI). In [100] a nonlinear Least Squares (LS) equalizer is found for IIR nonlinear systems and the authors in [101] propose an iterative method with a nonlinear predictor.

In this thesis an exact expression for an MMSE equalizer of a second-order Volterra system is proposed. The filter structure is shown in Fig. 4.2. As we will see in the next subsection, the receiver front-end and the channel can be modeled as a second-order Volterra system, with kernels $\{\mathbf{h}_i\}$. This nonlinear equivalent system model can then be equalized by another second-order Volterra model $\{\mathbf{g}_i\}$ where the coefficient calculation is described in this chapter. Generally, just the linear coefficients of such an equalizer are computed. We extend the linear MMSE equalizer by incorporating a nonlinear channel model and find an exact expression for the MMSE equalizer. Furthermore we extend the

MSE formulation to second-order Volterra cases and try to express a new second-order Volterra equalizer, which is supposed to improve the performance further. Additionally, the obtained results are compared with their least mean squares (LMS) counterparts, which should ideally achieve similar results.

Equalizer Model

We can now define an equalizer that is applied to the received signal $y[k]$. For a first-order Volterra or linear equalizer the estimated data sequence $\hat{d}[k]$ becomes

$$\hat{d}[k] = \mathbf{g}_1^T \mathbf{y}[k], \quad (4.5)$$

where $\mathbf{y}[k] = [y[k], y[k-1], \dots, y[k-L_e+1]]^T$, and where the $L_e \times 1$ vector \mathbf{g}_1 represents the linear equalizer coefficients. Applying a second-order Volterra equalizer to $y[k]$, we obtain

$$\hat{d}[k] = \mathbf{g}_1^T \mathbf{y}[k] + \mathbf{y}^T[k] \mathbf{G}_2 \mathbf{y}[k], \quad (4.6)$$

where the $L_e \times L_e$ matrix \mathbf{G}_2 represents the second-order kernel of the Volterra equalizer. Note that there is no zeroth-order kernel in both cases, since we already removed the bias from the channel model.

As we did for the channel, we can rewrite $\hat{d}[k]$ as

$$\hat{d}[k] = \mathbf{g}_1^T \mathbf{y}[k] + \mathbf{g}_2^T (\mathbf{y}[k] \boxtimes \mathbf{y}[k]), \quad (4.7)$$

where \mathbf{g}_2 is an appropriate modification of \mathbf{G}_2 .

4.4. MMSE Volterra Filters

In this section we derive linear and nonlinear equalizers for the nonlinear channel model.

4.4.1. First-Order Equalizer

First of all, let us assume that the second-order kernel \mathbf{g}_2 is zero and that we only focus on the first-order kernel \mathbf{g}_1 . We then have to derive an expression for $\mathbf{y}[k]$ as a function of \mathbf{h}_1 and \mathbf{h}_2 . To this end, let us rewrite the L_e elements of the input samples for the equalizer $y[k-l]$ as

$$y[k-l] = \mathbf{h}_{1,l}^T \mathbf{d}_x[k] + \mathbf{h}_{2,l}^T (\mathbf{d}_x[k] \boxtimes \mathbf{d}_x[k]) + n[k-l], \quad (4.8)$$

where the extended data vector is given by $\mathbf{d}_x[k] = [d[k], d[k-1], \dots, d[k-L-L_e+2]]^T$ and where the channel vectors $\mathbf{h}_{1,l}$ and $\mathbf{h}_{2,l}$ are appropriate extensions of \mathbf{h}_1 and \mathbf{h}_2 which depend on $l = 0, 1, \dots, L_e - 1$, respectively.

In short, we can thus write

$$y[k-l] = \mathbf{f}_l^T \mathbf{s}[k] + n[k-l], \quad (4.9)$$

where $\mathbf{f}_l = [\mathbf{h}_{1,l}^T, \mathbf{h}_{2,l}^T]^T$ and $\mathbf{s}[k] = [\mathbf{d}_x^T[k], (\mathbf{d}_x[k] \boxtimes \mathbf{d}_x[k])^T]^T$. Both vectors, \mathbf{f}_l and $\mathbf{s}[k]$ are having the dimension $(\varepsilon + \eta) \times 1$, where $\varepsilon = L_e + L - 1$ denotes the length of the linear terms, and $\eta = \sum_{\alpha=2}^L (L_e + L - \alpha)$ denotes the length of the nonlinear product terms.

It is then easy to see that we can write $\mathbf{y}[k]$ as

$$\mathbf{y}[k] = \mathbf{F}\mathbf{s}[k] + \mathbf{n}[k], \quad (4.10)$$

where $\mathbf{n}[k]$ is similarly defined as $\mathbf{y}[k]$, and where \mathbf{F} is a structured matrix containing the entries of each \mathbf{f}_l , i.e. $\mathbf{F} = [\mathbf{f}_0, \mathbf{f}_1, \dots, \mathbf{f}_{L_e-1}]^\top$. The explicit structure of the channel matrix is given by

$$\mathbf{F} = \begin{bmatrix} h_1[0] & 0 & \cdots & 0 \\ h_1[1] & h_1[0] & \cdots & 0 \\ \vdots & \ddots & \ddots & \vdots \\ 0 & \cdots & h_1[L-1] & h_1[L-2] \\ 0 & \cdots & 0 & h_1[L-1] \\ \hline h_2[0,1] & 0 & \cdots & 0 \\ h_2[1,2] & h_2[0,1] & \cdots & 0 \\ \vdots & \ddots & \ddots & \vdots \\ 0 & \cdots & h_2[L-1, L-2] & h_2[L-2, L-3] \\ 0 & \cdots & 0 & h_2[L-1, L-2] \\ \hline h_2[0,2] & 0 & \cdots & 0 \\ h_2[1,3] & h_2[0,2] & \cdots & 0 \\ \vdots & \ddots & \ddots & \vdots \\ 0 & \cdots & h_2[L-1, L-3] & h_2[L-2, L-4] \\ 0 & \cdots & 0 & h_2[L-1, L-3] \\ \hline \vdots & \ddots & \ddots & \vdots \\ \hline h_2[L-1, L-1] & 0 & \cdots & 0 \\ 0 & h_2[L-1, L-1] & \cdots & 0 \\ \vdots & \ddots & \ddots & \vdots \\ 0 & \cdots & 0 & h_2[L-1, L-1] \end{bmatrix}^{\top}, \quad (4.11)$$

where $h_1[k]$ is the $(k+1)$ -th entry of the first-order kernel \mathbf{h}_1 , and $h_2[k, l]$ is the $(k+1, l+1)$ -th entry of the second-order kernel \mathbf{H}_2 , as used in (4.1). Finally, the matrix \mathbf{F} is of dimension $(\varepsilon + \eta) \times L_e$. For the linear terms it has the conventional Toeplitz structure and for the nonlinear terms it has a Toeplitz structure built from off-diagonals of the second-order kernel.

For finding an equalizer, we can minimize the cost function $\mathcal{J} = \mathbf{E}\{(d[k] - \hat{d}[k])^2\}$. By incorporating the linear part of (4.7) and solving for the MMSE equalizer $\hat{\mathbf{g}}_1$ we obtain

$$\hat{\mathbf{g}}_1 = (\mathbf{F}\mathbf{R}_s\mathbf{F}^\top + \mathbf{R}_n)^{-1}\mathbf{F}\mathbf{R}_s\mathbf{e}_{\delta+1}, \quad (4.12)$$

where $\mathbf{R}_s = \mathbf{E}\{\mathbf{s}[k]\mathbf{s}^\top[k]\}$, $\mathbf{e}_{\delta+1}$ is a unit column vector with a “1” in position $\delta+1$, with δ the delay of the equalizer, and \mathbf{R}_n is the autocorrelation matrix of the noise. Under assumption A2, the noise correlation matrix can be written as $\mathbf{R}_n = \sigma_n^2\mathbf{I}_{L_e}$. Further,

under assumption A1, we can also define the structure of the autocorrelation matrix \mathbf{R}_s as

$$\mathbf{R}_s = \begin{bmatrix} c^2 \mathbf{I}_\varepsilon & \mathbf{0} \\ \mathbf{0}^\top & c^4 \mathbf{I}_\eta \end{bmatrix}. \quad (4.13)$$

The indices in the subscript of the identity matrices denote the size of the corresponding matrices, i.e. ε for the linear samples and η for the nonlinear samples, respectively. The final result in (4.12) is similar to the conventional purely linear equalizer and it can be viewed as a generalization of this MMSE equation. With our assumptions A1 and A2, the correlation matrices can be computed with the method shown in Appendix D.2. It is only questionable whether this linear solution shows good performance. This may be true for weakly nonlinear systems only.

4.4.2. Second-Order Equalizer

What if we do not assume that the second-order kernel \mathbf{g}_2 is zero? We then have to look for an additional expression of $\mathbf{y}[k] \boxtimes \mathbf{y}[k]$ as a function of \mathbf{h}_1 and \mathbf{h}_2 .

In general, we can write that

$$\begin{aligned} \mathbf{y}[k] \boxtimes \mathbf{y}[k] &= \mathbf{S}(\mathbf{y}[k] \otimes \mathbf{y}[k]) \\ &= \mathbf{S}[(\mathbf{F}\mathbf{s}[k] + \mathbf{n}[k]) \otimes (\mathbf{F}\mathbf{s}[k] + \mathbf{n}[k])] \\ &= \mathbf{S}(\mathbf{F} \otimes \mathbf{F})(\mathbf{s}[k] \otimes \mathbf{s}[k]) \\ &\quad + \mathbf{S}(\mathbf{F} \otimes \mathbf{I})(\mathbf{s}[k] \otimes \mathbf{n}[k]) \\ &\quad + \mathbf{S}(\mathbf{I} \otimes \mathbf{F})(\mathbf{n}[k] \otimes \mathbf{s}[k]) \\ &\quad + \mathbf{S}(\mathbf{n}[k] \otimes \mathbf{n}[k]), \end{aligned} \quad (4.14)$$

where \mathbf{S} is a selection matrix that transforms the Kronecker product \otimes into the modified Kronecker product \boxtimes . Considering now that a commutation of the Kronecker product is achieved by multiplying it by a permutation matrix \mathbf{P} (see Appendix D.1), we can rewrite (4.14) as

$$\begin{aligned} \mathbf{y}[k] \boxtimes \mathbf{y}[k] &= \mathbf{S}(\mathbf{y}[k] \otimes \mathbf{y}[k]) \\ &= \mathbf{S}(\mathbf{F} \otimes \mathbf{F})(\mathbf{s}[k] \otimes \mathbf{s}[k]) \\ &\quad + \mathbf{S}[(\mathbf{F} \otimes \mathbf{I}) + (\mathbf{I} \otimes \mathbf{F})\mathbf{P}](\mathbf{s}[k] \otimes \mathbf{n}[k]) \\ &\quad + (\mathbf{n}[k] \boxtimes \mathbf{n}[k]), \end{aligned} \quad (4.15)$$

The output of the second-order equalizer can be written as

$$\hat{d}[k] = \mathbf{g}_{1,2}^\top \mathbf{w}[k], \quad (4.16)$$

where $\mathbf{g}_{1,2} = [\mathbf{g}_1^\top, \mathbf{g}_2^\top]^\top$ and $\mathbf{w}[k] = [\mathbf{y}^\top[k], (\mathbf{y}[k] \boxtimes \mathbf{y}[k])^\top]^\top$.

We can now write $\mathbf{w}[k]$ as

$$\mathbf{w}[k] = \mathbf{Q}\mathbf{r}[k] + \mathbf{U}(\mathbf{s}[k] \otimes \mathbf{n}[k]) + \mathbf{m}[k], \quad (4.17)$$

where $\mathbf{m}[k] = [\mathbf{n}^\top[k], (\mathbf{n}[k] \boxtimes \mathbf{n}[k])^\top]^\top$, i.e., $\mathbf{m}[k]$ is similarly defined as $\mathbf{w}[k]$, $\mathbf{r}[k] = [\mathbf{s}^\top[k], (\mathbf{s}[k] \otimes \mathbf{s}[k])^\top]^\top$, and $\mathbf{U} = [\mathbf{0}^\top, [\mathbf{S}[(\mathbf{F} \otimes \mathbf{I}) + (\mathbf{I} \otimes \mathbf{F})\mathbf{P}]]^\top]^\top$. The big channel matrix \mathbf{Q} containing all products up to fourth order is given as

$$\mathbf{Q} = \begin{bmatrix} \mathbf{F} & \mathbf{0} \\ \mathbf{0} & \mathbf{S}(\mathbf{F} \otimes \mathbf{F}) \end{bmatrix}.$$

Now there is no correlation between the useful term $\mathbf{r}[k]$ and the noise terms $\mathbf{s}[k] \otimes \mathbf{n}[k]$ and $\mathbf{m}[k]$, since we've used the reduced Kronecker notations and zero-mean properties for $\mathbf{s}[k]$ and $\mathbf{m}[k]$, respectively.

To make things more clear, the final equation for $\mathbf{w}[k]$ is rewritten in a matrix form in (4.18).

$$\begin{aligned} \begin{bmatrix} \mathbf{y}[k] \\ \mathbf{y}[k] \boxtimes \mathbf{y}[k] \end{bmatrix} &= \begin{bmatrix} \mathbf{F} & \mathbf{0} \\ \mathbf{0} & \mathbf{S}(\mathbf{F} \otimes \mathbf{F}) \end{bmatrix} \begin{bmatrix} \mathbf{s}[k] \\ \mathbf{s}[k] \otimes \mathbf{s}[k] \end{bmatrix} \\ &+ \begin{bmatrix} \mathbf{0} \\ \mathbf{S}[(\mathbf{F} \otimes \mathbf{I}) + (\mathbf{I} \otimes \mathbf{F})\mathbf{P}] \end{bmatrix} [\mathbf{s}[k] \otimes \mathbf{n}[k]] + \begin{bmatrix} \mathbf{n}[k] \\ \mathbf{n}[k] \boxtimes \mathbf{n}[k] \end{bmatrix} \end{aligned} \quad (4.18)$$

The formula for the MMSE expression for $\mathbf{g}_{1,2}$ is now easily derived. Let us define the correlation matrices as

$$\mathbf{R}_r = \mathbf{E}\{\mathbf{r}[k]\mathbf{r}^\top[k]\}, \quad (4.19)$$

$$\mathbf{R}_{s,n} = \mathbf{E}\{[(\mathbf{s}[k] \otimes \mathbf{n}[k])][(\mathbf{s}[k] \otimes \mathbf{n}[k])]^\top\}, \quad (4.20)$$

and

$$\mathbf{R}_m = \mathbf{E}\{\mathbf{m}[k]\mathbf{m}^\top[k]\}. \quad (4.21)$$

One can show that the correlation between the data vector $\mathbf{r}[k]$ and the noise vector $\mathbf{n}[k]$ is zero since the assumption that data and noise are uncorrelated even holds for this modified data and noise vector. But this property only holds as long as we assume that the second-order kernels of the channel and the equalizer have zeros on the main diagonal.

With these assumptions we can use the same cost function as before to minimize. The parameters for the optimal equalizer are computed as

$$\hat{\mathbf{g}}_{1,2} = (\mathbf{Q}\mathbf{R}_r\mathbf{Q}^\top + \mathbf{U}\mathbf{R}_{s,n}\mathbf{U}^\top + \mathbf{R}_m)^{-1}\mathbf{Q}\mathbf{R}_r\mathbf{e}_{\delta+1}. \quad (4.22)$$

The correlation matrix \mathbf{R}_r is not easy to describe in an analytical way. We know that the very first part is given by a diagonal matrix $c^2\mathbf{I}$ because these elements describe the correlation between the purely linear symbols. The rest of the matrix represents different terms of correlation in the linear and nonlinear data parts. Due to the modified Kronecker notation used, a simplification of the correlation matrix is a very challenging task. However, we give a detailed description on how to describe the correlation matrix in Appendix D.2, which can be used for any correlation matrix used in this work, i.e. also for $\mathbf{R}_{s,n}$ and \mathbf{R}_m .

4.4.3. Adaptive Volterra Filters

As a comparison the effects of the newly derived equalizers (4.12) and (4.22) w.r.t. an adaptive equalizer solution is shown. For that purpose an extension to the conventional linear LMS adaptive algorithm [102] was used. These nonlinear extensions are needed to adapt the second-order kernel of the nonlinear LMS equalizer during training [103]. The modified LMS updating equations are obtained as

$$\mathbf{g}_1[k] = \mathbf{g}_1[k-1] + \mu_1 \mathbf{y}[k] e[k], \quad (4.23)$$

for the first-order kernel and as

$$\mathbf{g}_2[k] = \mathbf{g}_2[k-1] + \mu_2 (\mathbf{y}[k] \boxtimes \mathbf{y}[k]) e[k], \quad (4.24)$$

for the second-order kernel, with $e[k]$ denoting the error signal which is given as $e[k] = d[k - \delta] - \hat{d}[k]$ during the training phase.

4.4.4. Simulation Results

In this section we compare the linear (4.12) and nonlinear (4.22) equalizer. For that purpose we have used the nonlinear second-order equivalent system model derived in [11], which is a model for a frame-differential (FD) transmitted-reference (TR) UWB autocorrelation receiver (AcR) front-end. It describes the inter-symbol interference due to a time-dispersive multipath channel for the nonlinear AcR. The authors also derive an exact expression for the noise variance at the output of the receiver, given a certain double-sided noise spectral density $N_0/2$ at the receiver input. As a first approximation (which turned out to be a reasonable assumption for many scenarios), the noise is assumed to be a zero-mean i.i.d. Gaussian random process with a fixed variance σ_n^2 depending on the receiver parameters. Furthermore, the FD-TR-UWB scheme uses BPSK signaling to transmit data and thus fits into our framework defined in (4.4).

To compute the equalizer coefficients according to (4.12) and (4.22) it is necessary to determine the autocorrelation matrix of the data vectors $\mathbf{s}[k]$ and $\mathbf{r}[k]$. The autocorrelation matrix for $\mathbf{s}[k]$ is shown in (4.13) and is a scaled identity matrix with dimension $2L^2 - L$ if we assume that L is the number of channel taps and equalizer taps (i.e., $L_e = L$). The construction of $\mathbf{r}[k]$ is more complex and if we again take the same length for the channel and the equalizer, we get a huge autocorrelation matrix \mathbf{R}_r , of dimension $(4L^4 - 4L^3 + 3L^2 - L)/2$. We see that this size is mostly determined by the fourth-order term and brings an enormous increase in the size of the autocorrelation matrix.

To achieve reasonable simulation times and matrix sizes, a simplification of the nonlinear equivalent system model coefficients has been investigated first. For an RMS delay spread of the channel impulse response of $\tau_{\text{rms}}=10$ ns the authors in [11] propose an equivalent nonlinear system model with 17 linear coefficients and $(17 \times 16)/2$ second-order kernel coefficients at a data rate of 125 Mbps (i.e., a symbol time of 8 ns) to achieve sufficient model accuracy. For estimating the huge correlation matrix \mathbf{R}_r of the data when setting the equalizer length equal to the channel length, this complexity has to be reduced. For that reason a comparison of the equivalent system model to a truncated version of itself has been done first. The quantity we have compared to achieve similar system behavior is the data averaged Bit Error Rate (BER). Moreover, the quantiles of the two results

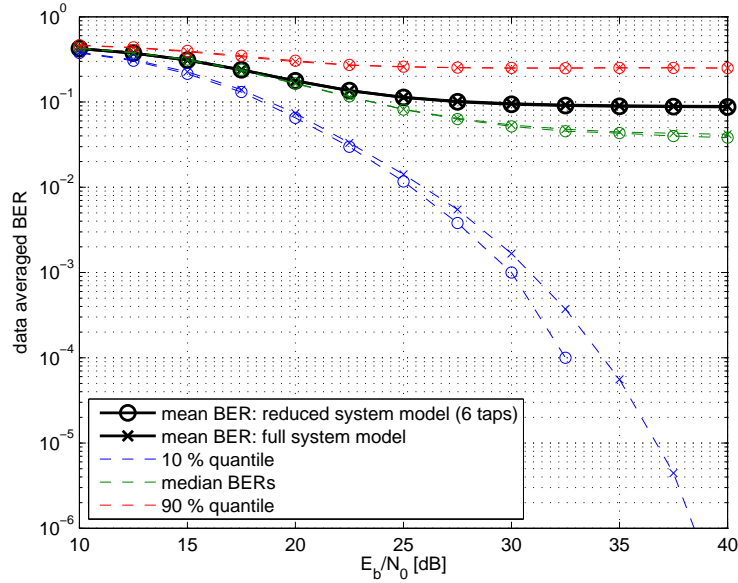


Figure 4.3.: Comparison of reduced equivalent system model performance with full system model performance; determined by averaging over 1000 different equivalent system models.

are compared and analyzed by simulation. It has been seen already in [11] that the RMS value of the equivalent nonlinear system model coefficients is rather low when deviating from the desired data symbol. This means that the overall contribution of the terms with high distance to the desired symbol is small or even negligible. A sophisticated analysis of this behavior is also found in [79].

For an equivalent truncated system model of 6 taps (i.e., 6 taps for the linear kernel and $(6 \times 5)/2$ taps for the second-order nonlinear kernel), the performance results in terms of BER are shown in Fig. 4.3. For these results, a conventional threshold detector has been used, which decides on the sign of the sampled output signal without equalization. It is seen, that the results for the 90-percent quantile, mean, and median of the data-averaged BER are practically the same for the truncated system. For the 10-percent quantile a minor deviation from the full system model is visible. For that reason, a truncated version of the nonlinear equivalent system model is used to keep the complexity low and to allow estimation of the autocorrelation matrix of the data. If we consider that the perfect equalizer (ZF) would have an infinite number of taps (IIR), the truncation to $L_e = L = 6$ taps is rather crude. An increase to 12 taps for the equalizer length L_e has shown to deliver good results. With the specified lengths of channel and equalizer the autocorrelation matrix was constructed according to Appendix D.2, and then used for all the computations since it remains constant.

To benchmark the performance, an adaptive nonlinear filter has been used with (4.23) and (4.24) as update equations. The length of the adaptive filter was also set to $L_e = 12$ to have similar computational cost. For the stepsize of the algorithm we used constant

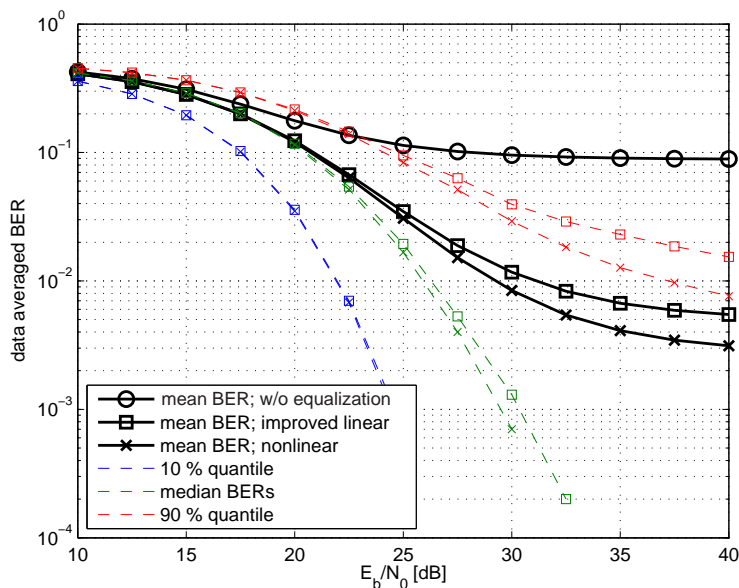


Figure 4.4.: Comparison of MMSE equalizers; linear and second-order equalizer performance analyzed over 800 different equivalent system models.

and exponentially decaying stepsizes. With a constant stepsize the adaptive algorithm has problems to achieve a high performance solution for the inverse of the system. With an exponentially decaying stepsize a high performance is observed, which is very similar to the performance of our proposed nonlinear equalizer. The comparison of the analytical equalizer computations is shown in Fig. 4.4 where again, the mean, median, 10%, and 90% quantiles are shown for the achieved equalizer performance. It is clearly visible that the nonlinear equalizer outperforms the linear equalizer. This comes, however, at the cost of an increased complexity.

The results of the adaptive equalizer are shown in Fig. 4.5. It is seen clearly, that a similar performance can be achieved by these equalizers. However, the estimation of the equalizer coefficients has to be performed with training sequences. For our equivalent nonlinear system model, a few tenthousand training symbols are needed to achieve good convergence of the coefficients of the nonlinear adaptive equalizer. A “converged solution” is achieved when using an exponentially decaying stepsize parameter in (4.24). With this decaying stepsize parameter also the convergence speed is influenced which is also one of the reasons why we need a lot of training data to find a good nonlinear equalizer.

We furthermore compared the output of the receiver front-end without equalization, with the improved linear equalizer, and with the nonlinear equalizer. The sequences of data symbols is depicted in Fig. 4.6 for an SNR of 40 dB to keep possible mistakes due to noise small. To allow a comparison to the originally transmitted data sequence we have depicted the data symbols with squares in each subplot. Furthermore, the equalized data symbols are shown either with a ‘x’ for an incorrectly detected data symbol or a ‘o’ for a correctly detected symbol. One can see that especially at data symbol changes (from +1 to -1 and vice versa) the nonlinear equalizer achieves better performance due to its nonlinear dynamics.

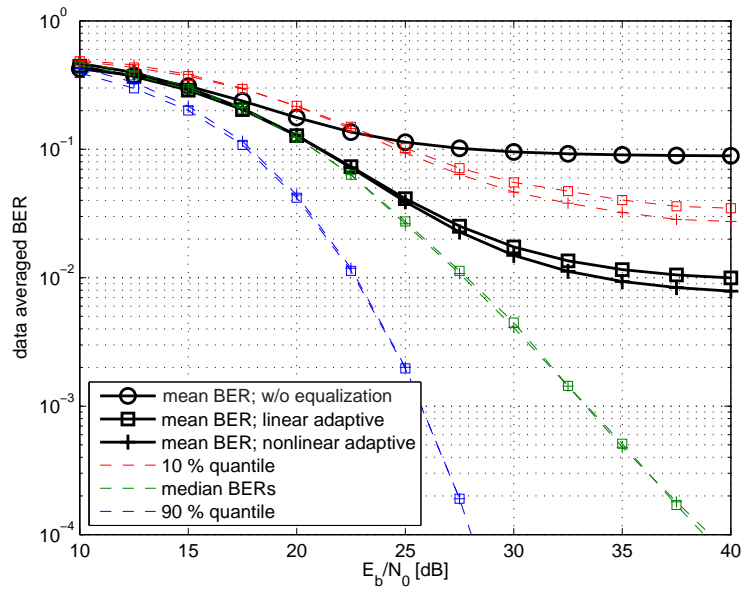


Figure 4.5.: Comparison of adaptive equalizers with 50000 training symbols and exponentially decreasing stepsize; Performance evaluated by averaging over 800 equivalent system models.

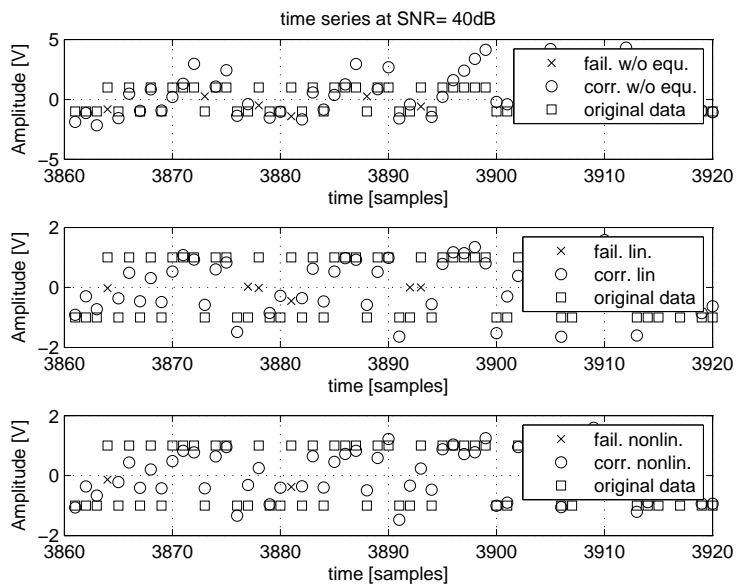


Figure 4.6.: Time series of distorted data symbols, data symbols after the linear equalizer, and data symbols after nonlinear equalizer.

4.5. Conclusions

In this chapter a non-coherent receiver front-end was presented which offers a cheap and low-complexity solution to receive pulsed UWB signals. The simplicity of the front-end is however traded for a nonlinear system behavior. Incorporating the effects of the wireless propagation channel into the system model we can find a Volterra model to be appropriate to describe the system's nonlinear dynamical behavior. For such a non-coherent UWB receiver front-end, the model is of second order, i.e., a second-order Volterra system.

For the nonlinear second-order Volterra model, a novel equalization approach has been developed. First a novel linear equalizer has been derived, which considers a nonlinear Volterra structure of the channel. The achieved results for this computation are similar to the results in [14], but are formulated more generally. We have also seen that the equivalent system model can be truncated without losing model accuracy in terms of BER. Furthermore, a novel second-order Volterra equalizer was designed by explicitly solving the MMSE problem for the tandem connection of two second-order Volterra systems. Compared to the p -th order inverse shown in [94], the noise in the system has been considered in the shown approach. Furthermore, the linear term is not required to be minimum phase, i.e., to be invertible, in the proposed approach.

The performance of the novel equalizer is compared to a similarly structured adaptive equalizer, which shows that similar performance can be achieved with both approaches. However, the optimal solution is found with our expressions in one computational step when the coefficients of the nonlinear model are available. An adaptive algorithm with exponentially decaying stepsize takes prohibitively long to approach that optimum.

Conclusion and Outlook

In this thesis novel implementation approaches for standardized and non-standardized UWB systems have been presented. The discussed UWB systems offer the potential for high-speed communication systems and for providing exact positioning and tracking capabilities.

From the discussions in Chapter 2, it is clear that the direct implementation of transceiver architectures on state-of-the-art DSP hardware is a very challenging task. Processing at Nyquist sampling rate is simply not feasible and requires a technological breakthrough to achieve a direct implementation of the transceiver algorithms. Thus alternatives have to be found for transceiver and channel model implementations. In this thesis the parallelization in frequency-domain of the transceiver algorithms for a wideband OFDM system is shown. This can be achieved by employing hybrid filterbanks for signal separation and subband signal processing. Similarly, the channel response can be modeled on a parallel filter architecture which has several implementation challenges when steep filters are needed.

A model with frequency-response masked filters has been achieved and demonstrated in this thesis. Still, a slight overlapping of the subbands has to be allowed to model the overall behavior without gaps in the frequency-domain. The effect of this overlapping is visualized as an MSE on a carrier-by-carrier basis. It is seen that the subcarriers at the band edges are more distorted than others. Additionally, the distortion effect has been visualized in terms of SER. Clearly, a relation between high error peaks and the degradation in SER is visible. Similar performance degradation as for the transmitter can be observed in the receiver. At the band edges the additional error due to the finite slope of the analog front-end filters is visible. An SER degradation can be observed in the subband architecture which limits the uncoded SER to flatten out at an error floor of 10^{-3} for 8 subbands and 10^{-4} for 4 subbands. The occurring interference can be taken care of with an equalizer adapted during a training or calibration period. Such an equalizer has to be used anyhow if the degradation of the signal due to a wireless propagation channel is considered to recover the transmitted data. Since the introduced distortions in the front-ends are linear distortions, a linear equalizer should be used to enhance the system performance. The resulting subband models should be analyzed in more detail as further research. An optimization of such a structure with respect to system parameters

and certain propagation environments is another topic for further research.

Another possibility of generating wideband signals is to generate short pulses. These signals are advantageous for short-range communication and positioning applications because transmitters and receivers can be built with low power and low complexity. A flexible signal generator employing DACs has to be used when effects as flexible pulse shape generation, equalization of distortions in the front-end, adaptation to environments, generation of impulse responses for simulation environments, generation of MB-OFDM signals, etc. are desired with one single structure. Current technological limits restrict the bandwidth to be generated with a single DAC to a few hundred MHz. Thus, a converter array, where multiple DACs operate in a time-interleaved structure is proposed in this thesis. With these converter arrays, signals of higher bandwidth can be generated. The architecture also enables an oversampled generation of UWB signals, hence low-complexity analog filters can be used due to the shifting of the spectral replicas to higher frequencies. The converters in this structure are assumed to be perfectly matched in time, such that no additional mismatch spectra occur. The performance of the converter structure has been verified with simulations and measurements and a reduction of the first spectral mirror image component by 30 dB has been possible for narrow and wideband signals.

If mismatches between the converters are considered, a compensation structure in the digital back-end of the signal generator can be developed. This compensation strategy for mismatches has been demonstrated and verified with measurements. It is possible to reduce the mismatch spectra by app. 20 dB with the proposed compensation approach. The compensation structure assumed that the timing offsets for the TIDAC structure are known. However, in a practical application the offsets have to be identified continuously and an adaptive tuning of the parameters of the compensation filters has to be done. This can be done very effectively with a Farrow filter, where the shape of the compensation filter depends on one steering parameter, which can be directly related to the timing offset (assuming a two-channel case).

For the pulse-based signaling scheme standardized by the IEEE 802.15.4a task group, three low-complexity receiver architectures have been investigated and compared. First of all, a Rake receiver has been evaluated in its performance for the standardized signal. It has been demonstrated that the performance strongly depends on the synchronization of the receiver. Furthermore it improves with the number of fingers used. However, an increase of fingers also means an increase of complexity, which prohibits a high number of fingers to be implemented. From an implementation complexity point of view, an energy detector offers the most simple solution. On the other hand, the MU performance of the ED is not very good. Therefore a novel modified TR receiver has been proposed for the standardized, pulse-based UWB communication scheme considering the additional information contained in the spreading code. With slightly increased complexity for the modified TR scheme, a superior MU performance can be achieved. The comparison has been carried out with computer simulations. Strategies to combat the MUI or signal processing algorithms to have a robust receiver when NBI is present are topics for further research.
















It has been observed that these simple non-coherent receivers can be modeled by fading memory nonlinear systems, i.e., Volterra systems. This means, for very high data rates, the inter-symbol interference for such receivers is fully described with a nonlinear system model. It was shown in [104] that in a high data-rate system this nonlinear distortion is

considerably high. Thus, if such a receiver is used, a sophisticated equalizer has to be used to recover the transmitted data symbols. An optimal MMSE nonlinear equalizer is derived in this thesis. The novel equalizer perfectly demonstrates that an adaptive LMS filter solution can achieve the same performance only asymptotically, i.e., after infinite time. The computation for the novel equalizer is done in one single step, but it assumes that the linear and nonlinear system parameters of the equivalent system model are known. The equalizer structure improves the uncoded BER floor by a factor of 20, if the output signal is sampled at symbol rate. An interesting question is how a similarly-optimized equalizer performs on a multichannel Volterra system as described in [79], when the output of the front-end is oversampled.

Chapter 5. Conclusion and Outlook

UWB Chipsets

In the following table all the available single chip implementations of the current WiMedia and ECMA-368 standard are collected. There is also one manufacturer which does not stick to the standard but distributes first reference designs. Furthermore, some manufacturers have already Wireless USB hubs on the market where it is questionable if they will ship these products for testing to Europe. Also these products are included in this list.

Manufacturer	Chip Name	WiMedia, ECMA-368	PHY	MAC	Datasheet	Website	Comment
Alereon Inc.	AS4000	yes	yes	yes			chip family
Alereon Inc.	AS5000	yes	yes	yes			first worldwide chip
Artimi	RTMI-150 UWB MAC	yes	no	yes			MAC only
Focus en- hancements	TT-1013	yes	yes	yes	N/A		System on a chip
General Atomics	ASPEN 2000-006	no	yes	yes			Spectral Keying, proprietary
Intel	Wireless UWB Link 1480	yes	no	yes			MAC only
NEC	μ PD720170, μ PD720180	yes	no	yes			MAC only
NXP	ISP3582	yes	yes	yes			single chip solution
Realtek	RTU7010	yes	no	yes	N/A		PHY only

Appendix A. UWB Chipsets

Realtek	RTU7010	yes	no	yes	N/A		PHY only
Realtek	RTU7105	yes	yes	yes	N/A		single chip solution
Sigma Designs Inc.	Windeo	yes	yes	yes			dual chip solution
Staccato Communications Inc.	SC3501	yes	no	yes	N/A		MAC only
Staccato Communications Inc.	SC3502	yes	yes	yes	N/A		
Staccato Communications Inc.	SC3503	yes	yes	yes	N/A		
Wipro-NewLogic	-	yes	no	yes			MAC IP Core
Wiquest Communications Inc.	WQST110, WQST101	yes	yes	yes			dual chip solution*
Wisair Inc.	WSR601	yes	yes	yes			single chip solution
Wisair Inc.	WSR531, WSR502	yes	yes	yes			dual chip solution

Table A.1.: Overview of standardized chip solutions, (*WUSB hub as a prototype)

UWB Demonstrator

Within this thesis work, two UWB demonstrators have been built. Both of them consist mostly of off-the-shelf hardware which allows easy construction of the transmitting devices. In this appendix one of these demonstrators which enables to transmit wideband pulses over the wireless propagation channel is presented. The other demonstrator tries to simulate the effects of the channel on an FPGA board. The demonstration system was built to show the performance of pulse-based UWB systems surviving in a multipath propagation environment. However, building a receiver is a quite complicated task for broadband systems with off-the-shelf components. Thus, the receiver was simulated by sampling the received signals after the channel with a sampling scope, able to resolve 6 GHz of bandwidth. To propagate the signals in free space, antennas are needed to match the impedance of the circuitry to the impedance of free space. Major contributions to the hardware development have been done by one diploma thesis student [105] and a project student [106] which are fully acknowledged.

B.1. FPGA Hardware

As mentioned before, the demonstrator was used to generate a pulse-based UWB signal. According to the standard for the pulse based UWB PHY [6], pulses modulated in amplitude have to be generated. Furthermore, long silence periods have to be generated. To smoothen the transmitted spectrum, the pulses transmitted with the demonstrator are hopped in time. The modulation scheme used for the pulses is a frame-differential scheme as described in [11]. The transmitted pulses have been generated with a Xilinx Virtex 2 Pro FPGA programmed with VHDL. To generate short pulses, required for the broad signal spectrum, high speed digital differential outputs of an FPGA have been used. With this technology (called Rocket I/O) it is possible to generate serial data streams with up to 3.25 Gbps. The signal levels driven by these high speed outputs are standardized according to the Low Voltage Differential Signaling (LVDS) standard [107] which was developed to achieve high data rate transmission of signals at low power. To generate ternary signals, two differential output signals were combined together as shown in Fig. B.1, using a resistive network. To match the output impedance of the differential signals, which is 100 Ohms to the transmission line which connects the pulse generator to a mixer circuitry, a

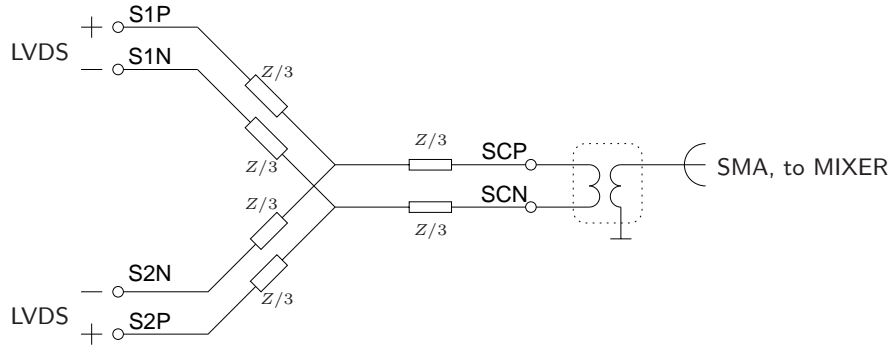


Figure B.1.: Resistive power combiner for ternary signals

LVDS 1	LVDS 2	OUT
0	0	0
0	1	-1
1	0	+1
1	1	0

Table B.1.: Truthtable for the resistive power combiner

broadband BALUN (BALanced/UNbalanced) transducer was used. The resistors of the combiner are computed as $Z/3$ where Z is the conventionally used impedance of 50 Ohms. Please note that a loss of 6dB is inherently present in this power combiner because the power is distributed over two ports.

According to the transmitted bits of the two LVDS outputs, the output signals of the power combiner are constructed according to the truth table shown in Table B.1. With this mapping positive and negative “rectangular” pulses with a duration down to 500 ps can be generated with the high speed digital outputs.

Thus, it is possible to generate ternary, very short duration pulses with a bandwidth of app. 2 GHz. However, as seen in the general introduction, the frequency bands for unlicensed UWB transmission are starting from 3.1 GHz. To convert the baseband signal to this frequency band, they have to be shifted in frequency domain (mixed) to a carrier frequency, which was chosen to be 4 GHz in our system.

B.2. RF Front-End

At the beginning the shifting of the real baseband pulses has been done by a Power Signal Generator (PSG) (Agilent E8267C) and its wideband I/Q inputs with a bandwidth of 2 GHz. However, this solution was only a good choice for the very first steps in designing the testbed. For a mobile UWB transmitter, the use of the PSG is not possible since it is a heavy-weight and expensive device. To come closer to a realistic device, the mixer circuitry has been designed separately with off-the-shelf RF components. Now the whole Local Oscillator (LO) generation and mixing is done on a small 22×14 cm board which

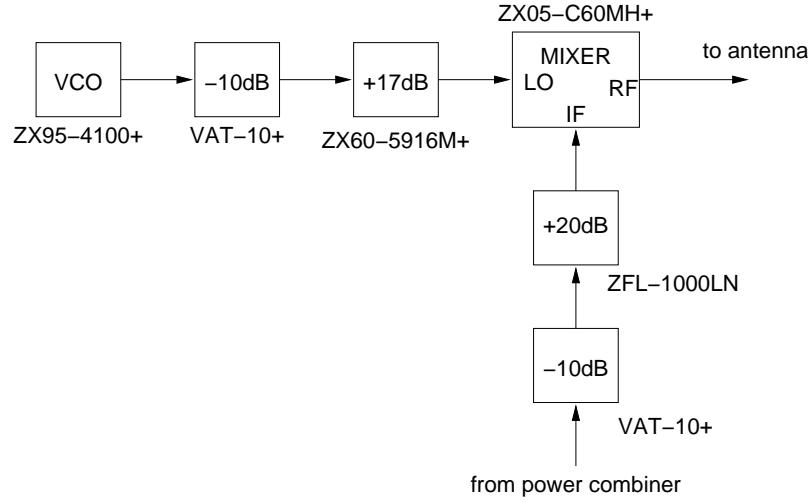


Figure B.2.: RF front-end for transmitter consisting of local oscillator, broadband mixer, and amplifiers for power level matching

just needs some additional stable power supplies to generate supply voltages for the active devices. The block diagram of the whole circuitry is shown in Fig. B.2 where the LO is generated by adjusting a fixed frequency with an adjustable DC voltage. Currently, the supply and steering voltages come from laboratory power supplies where arbitrary voltages can be selected for tuning.

A photograph of the whole mixing circuitry is shown in Fig. B.3 where all the components are connectorized versions. For a final circuit design, the whole system can be integrated on a PCB using solder-in versions of the RF components and should then even consume less space. The only challenge is to achieve good decoupling of the linearly regulated power supplies which have to be integrated as well in the RF circuitry.

B.3. UWB Antennas

To radiate signals into the air, it is necessary to have a device which matches the impedance of the electronic circuitry (usually 50 Ohms) to the impedance of the free space. Generally, such devices are called antennas. A schematic of this matching architecture is shown in Fig. B.4. Next to the impedances of the different media, the traveling waves are shown in this picture.

The wave traveling from the generator to the antenna is called V_0^+ . Since the matching is imperfect, a wave, called V_0^- is traveling back to the generator. Consequently, we can define the reflection coefficient Γ as the ratio between these two waves as

$$\Gamma = \frac{V_0^-}{V_0^+} = \frac{Z_A - Z_0}{Z_A + Z_0}, \tag{B.1}$$

where the traveling waves have been replaced with the corresponding impedances, respectively. Computing the logarithm of this ratio, generally defines the scattering parameter

Appendix B. UWB Demonstrator

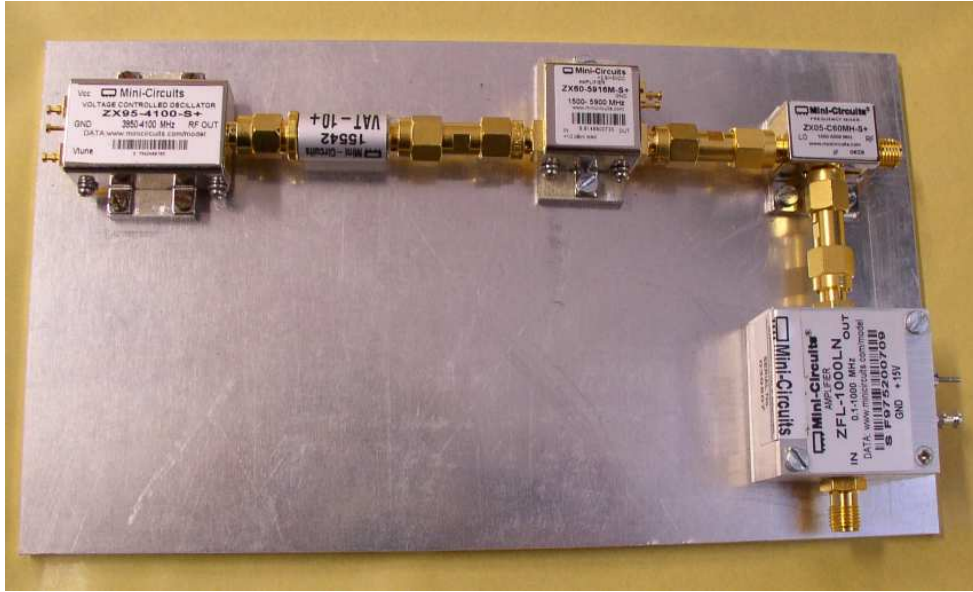


Figure B.3.: Photo of the RF front-end circuitry consisting of voltage controlled oscillator (VCO), broadband mixer, and amplifiers for power level matching

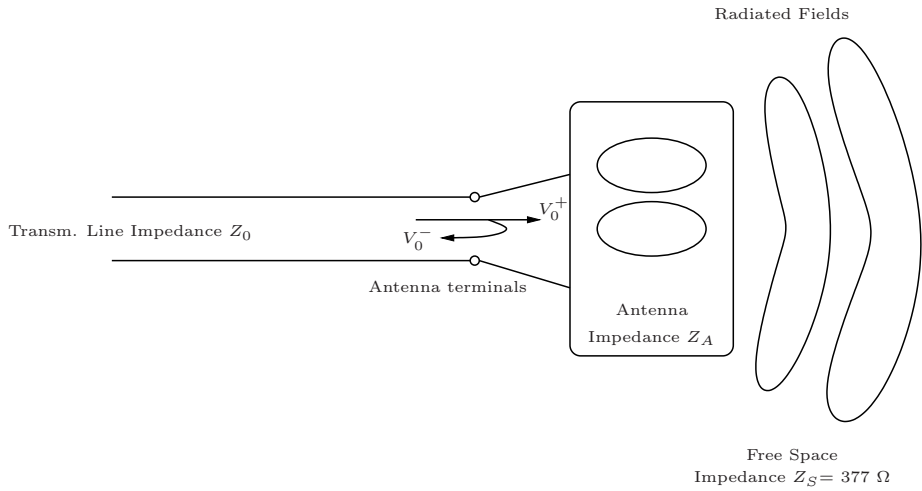


Figure B.4.: Antenna seen as a transformer for broadband matching of the 50 Ohms conventionally used in RF circuitry to the 377 Ohms of free space

S_{11} as

$$20 \log_{10} |S_{11}| = 20 \log_{10} |\Gamma| = 10 \log_{10} |\Gamma|^2. \quad (\text{B.2})$$

Another measure for the matching is the Voltage Standing Wave Ratio (VSWR) which is defined as

$$\text{VSWR} = \frac{1 + |\Gamma|}{1 - |\Gamma|}. \quad (\text{B.3})$$

For a detailed description of these parameters we refer the interested reader to [108] where

Match	VSWR	$\log_{10} S_{11} $ [dB]	Power Loss [%]
Marginal	3.00:1	-6.0	25
Good	2.00:1	-9.5	11.1
Good	1.92:1	-10	10.0
Excellent	1.50:1	-14	4
Superb	1.22:1	-20	1

Table B.2.: Comparison of the matching by means of VSWR, S_{11} , and relative power loss

a detailed treatment of theory and measurement of scattering parameters is shown.

Using these quantities to distinguish the quality of the matching we can define a very crude categorization as seen in Table B.2 [109]. Please note, that these matching qualities differ from application to application. Thus a general quality measure for the matching is difficult to define. Anyhow, within this work the threshold for a good match is set to be -10 dB or lower meaning a “good” match according to Table B.2.

For the demonstrator, four different antennas have been compared. Three of them are broadband dipole antennas which are made of two elliptic or circular patches. The antennas were designed w.r.t. the recommendations given in [109] for the size of the patches and ratios between principal axis to secondary axis, distance between the two patches, and feeding of the patches [106]. The feeding was done with a semi-rigid coaxial cable where a hard matching from the differential nature of the dipole to the single ended cable was done. A fourth antenna used in the measurement campaign was a PCB mounted patch antenna where the front patch has been improved with LTCC ceramic technology¹. Photographs of the four different antennas used in the measurement campaign are shown in Fig. B.5(a)-B.5(d).

B.3.1. Matching

In this section the measurement results obtained with a conventional Vector Network Analyzer (VNA) for analyzing the matching performance of the four different antennas are briefly described. The network analyzer was calibrated according to the OSM (Open Short Match) calibration standard to eliminate the effects of the cables and imperfections of the directive elements in the VNA front-end [108]. For further considerations the operating range of these antennas is considered to be in regions where the matching is better than -10 dB to achieve a good match.

As seen in Fig. B.6(a), with the elliptical structure, the matching is achieved over a very broad frequency range. For the elliptical antenna it even exceeds the targeted frequency band with a good match from app. 3 to app. 12 GHz. The circular antennas have a smaller operating range (3 to 9 GHz and 3 to 10 GHz) but are easier to construct since coins in the desired size are available. The LTCC antenna also achieves good matching in the frequency range from 2.5 to 11 GHz. This is quite remarkable because achieving

¹Thanks again to Manfred Stadler and Michael Leitner from EPCOS OHG Deutschlandsberg for providing the antenna.

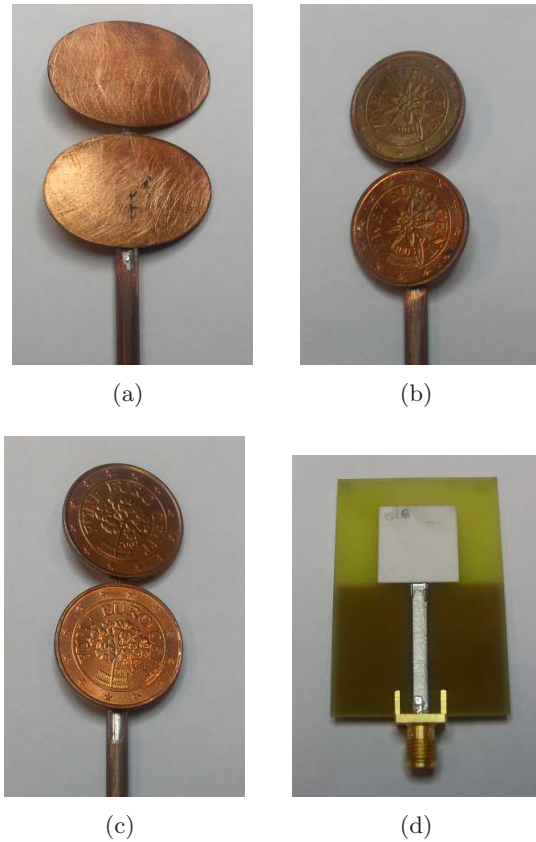


Figure B.5.: Antennas measured in the measurement campaign: (a) Broadband dipole antenna with two elliptical patches; (b) Broadband dipole antenna with small circular patches; (c) Broadband dipole antenna with big circular patches; (d) Broadband monopole antenna in LTCC technology

a good match on PCB is rather easy for narrow band systems but for wideband or even UWB systems this is not trivial.

B.3.2. Directivity Measurements

To verify the directivity of the constructed antennas, a measurement in an anechoic chamber has been conducted². For that reason, the antenna has been mounted onto a tower which can be turned around the x and z axes. The rotation angle θ around the x axis was adjustable from 0 to 360 deg. Around the z axis, the whole tower can be rotated by $\varphi = 0, \dots, 180$ degrees. This allows to measure one half-sphere of the directivity pattern of the antennas. Since the antenna is symmetric in its physical dimensions, the other half-sphere is assumed to be the same. As a probing system a calibrated waveguide was used which was approximately 1.5 m away from the measured antenna in the anechoic chamber. This can be considered to be a far-field measurement (or considering a wavelength at 10 GHz a

²Thanks to Sven Dortmund and the HFT Institute at University of Hannover, Germany for performing the measurements.

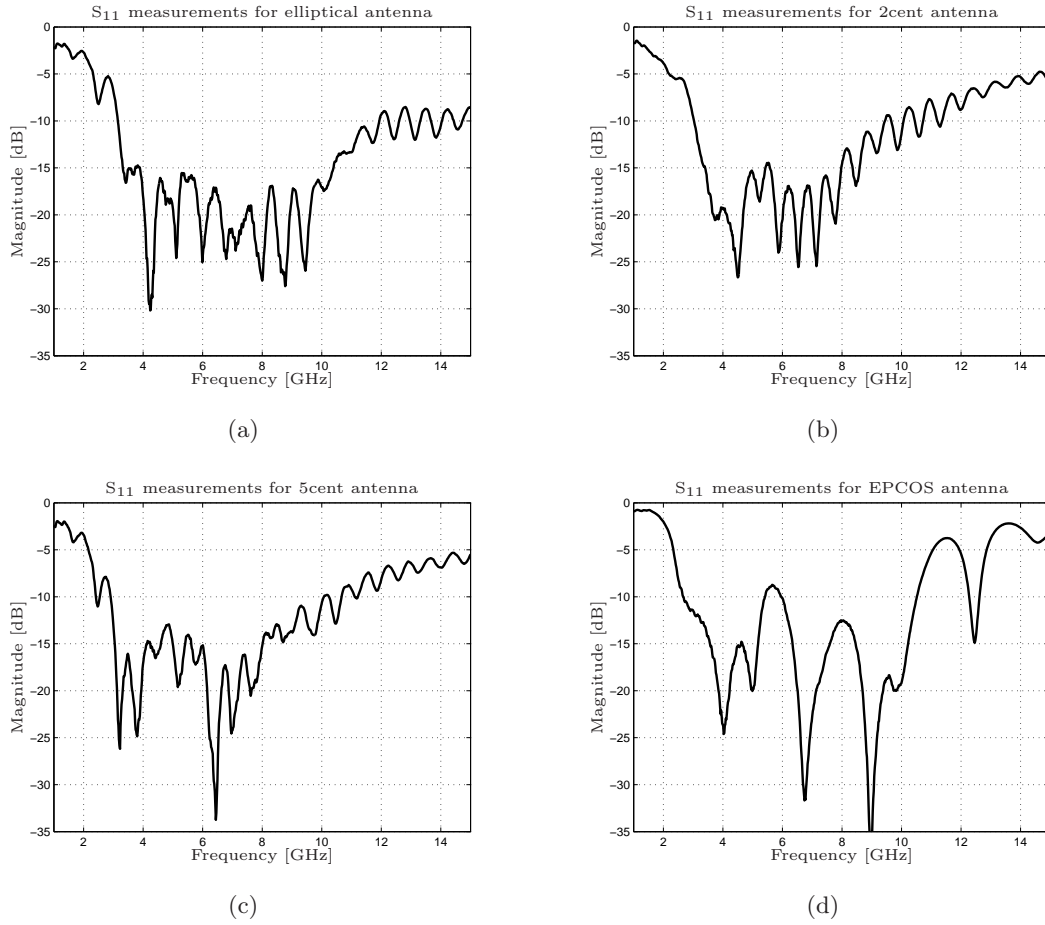


Figure B.6.: Matching of the broadband antennas w.r.t. S_{11} : (a) Broadband dipole antenna with two elliptical patches; (b) Broadband dipole antenna with small circular patches; (c) Broadband dipole antenna with big circular patches; (d) Broadband monopole antenna in LTCC technology

close to near-field) and a transformation considering effects of the chamber geometry and introducing an infinitely far boundary condition has to be applied [110]. The far-field for this geometry and frequencies can be computed to be between 5 cm and 11 cm [111].

For the intensity measurements each of the two angles is swept from the minimum value to the maximum value and a continuous wave (CW) signal at a certain frequency (here 3 and 10 GHz) is measured. The intensity plots for the 3 GHz measurements are shown in Fig. B.7 as a surface over the two angles ϑ and φ . What can be observed easily is, that all antennas have almost omnidirectional beampatterns except for the angles of $\varphi=90$ deg. and $\varphi=270$ deg. This is obvious because in these scenarios the antenna points with the bottom or with the top to the probe and since the electromagnetic wave is propagated to the right and left side, a minimum is encountered. Additionally, a small mismatch from the ideal spheric pattern is seen at $\vartheta=90$ deg. and $\varphi=60$ deg. and 120 deg. which means that a minor directivity to the front side is present. This is assumed to be from the feeding

Appendix B. UWB Demonstrator

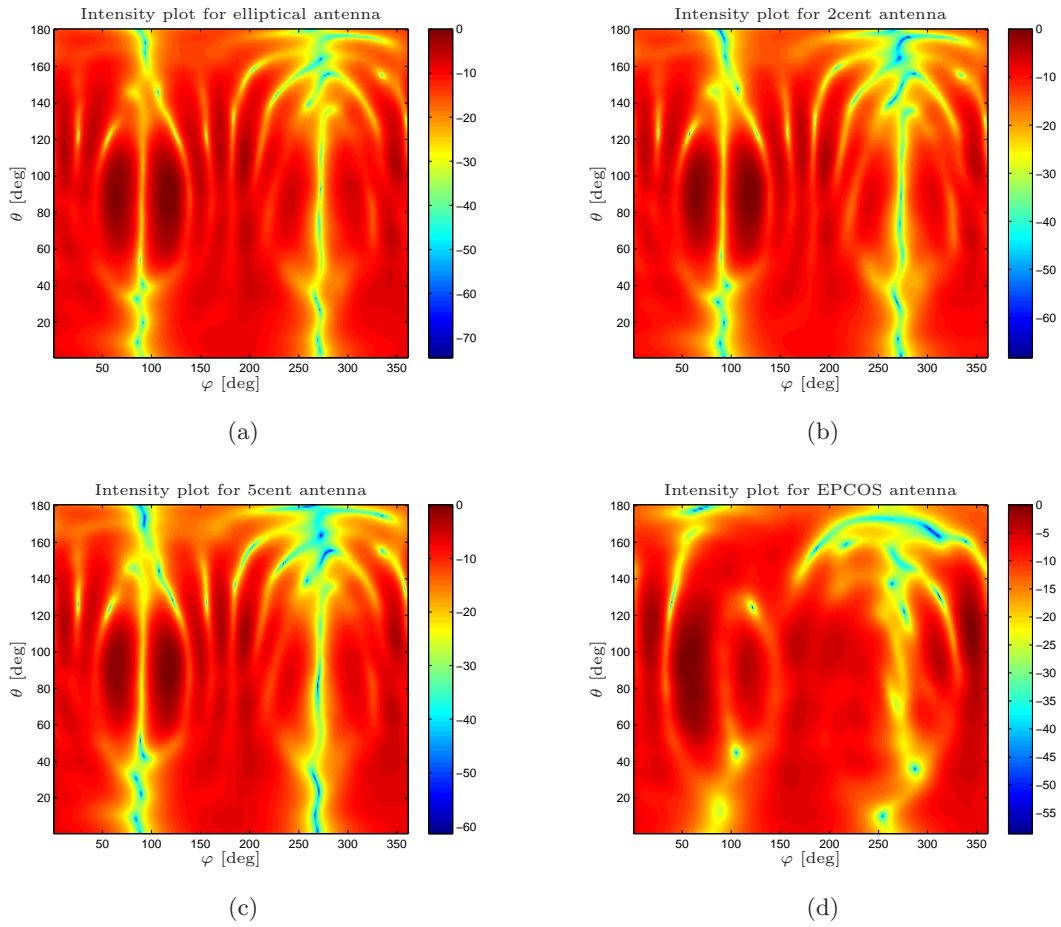


Figure B.7.: Intensity plots of the broadband antennas at 3 GHz: (a) Broadband dipole antenna with two elliptical patches; (b) Broadband dipole antenna with small circular patches; (c) Broadband dipole antenna with big circular patches; (d) Broadband monopole antenna in LTCC technology

line and can also be observed in the horizontal cuts shown in Fig. B.8. These cuts are only shown for 3 GHz in this report, since the cuts at 10 GHz show a pretty similar picture.

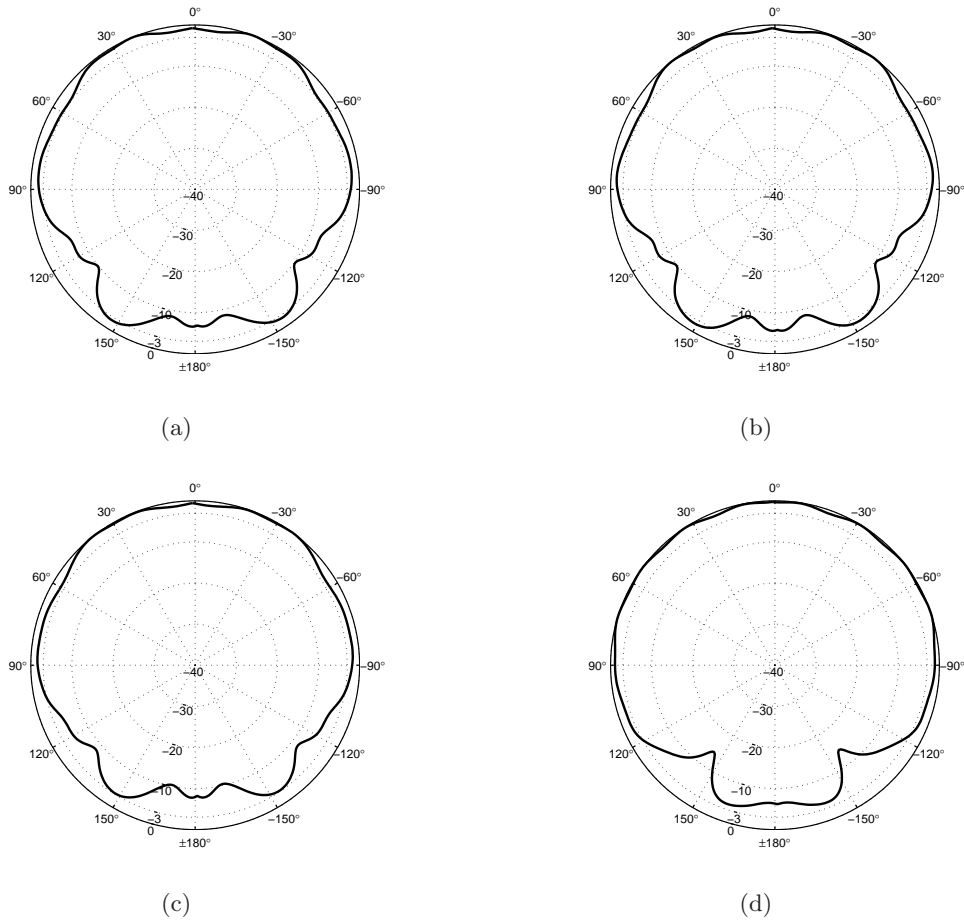


Figure B.8.: Horizontal directivity plots at 3 GHz: (a) Broadband dipole antenna with two elliptical patches; (b) Broadband dipole antenna with small circular patches; (c) Broadband dipole antenna with big circular patches; (d) Broadband Monopole antenna in LTCC technology

Similarly the effects at $\varphi=90$ deg. and $\varphi=270$ deg. can be nicely seen in the vertical cuts which show minima exactly at these angles (*cf.* Fig. B.10).

Similar effects are observed at a frequency of 10 GHz as shown in Fig. B.9. However, one can see that due to the high frequency more and more ripple occurs in the spherical surface which causes a minor degradation of the performance of the antenna. One can additionally see that the sphere does not show any distinct maxima anymore, which means that the variance of the ripple around the sphere is less for higher frequencies.

Finally, the polarization of the antennas is shown at 3 GHz and 10 GHz in Fig. B.11 and Fig. B.12, respectively. This was measured with a 90 deg. rotated output of the probe used for the measurements. It is seen that a separation of the two polarization areas is possible over a wide angular range. However, at the borders, i.e., where the sphere of the directivity pattern has its minima, the two components have equal magnitude and cannot be separated anymore.

Appendix B. UWB Demonstrator

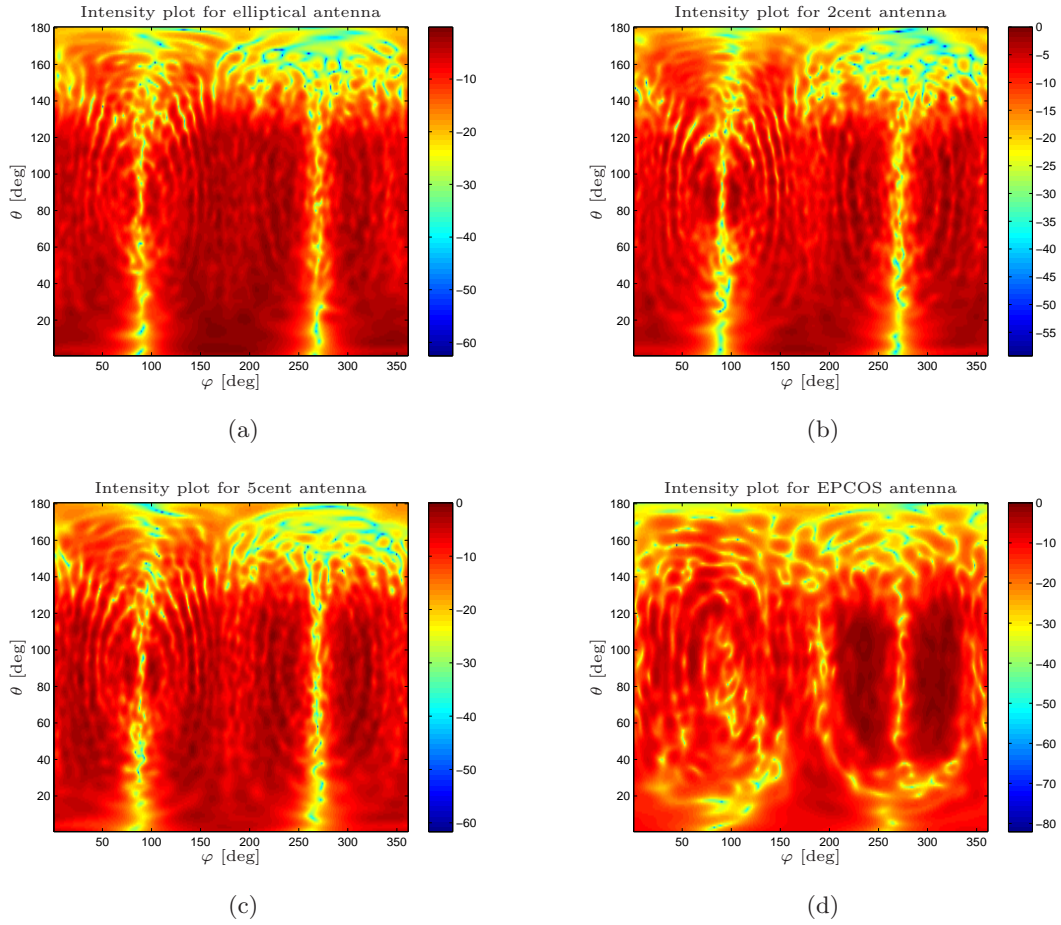


Figure B.9.: Intensity plots of the broadband antennas at 10 GHz: (a) Broadband dipole antenna with two elliptical patches; (b) Broadband dipole antenna with small circular patches; (c) Broadband dipole antenna with big circular patches; (d) Broadband Monopole antenna in LTCC technology

At 10 GHz the polarization properties of the dipole antennas becomes even worse. Now, only a good separation between the two components can be achieved in a very narrow band around the center (*cf.* Fig. B.12(d)). This shows a great influence of the angle when two such antennas are used for a communication system. We will see similar performance measures when we look at the antenna gains measured in the time domain.

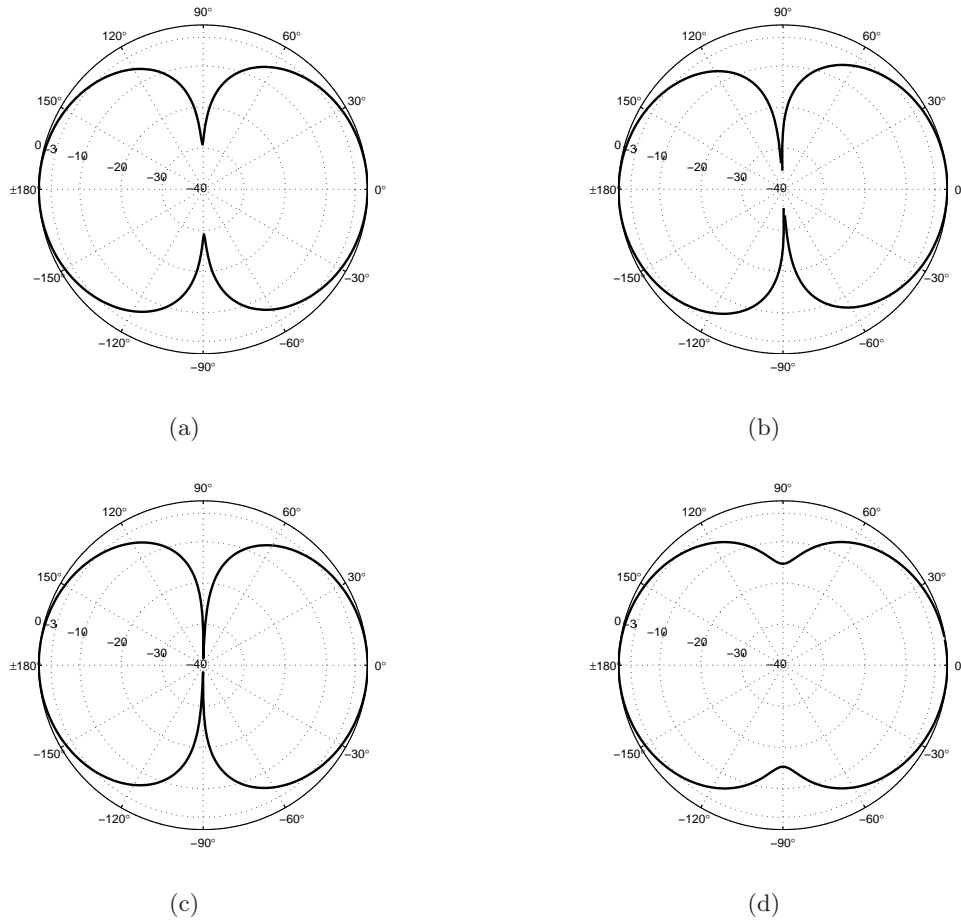


Figure B.10.: Vertical directivity plots at 3 GHz: (a) Broadband dipole antenna with two elliptical patches; (b) Broadband dipole antenna with small circular patches; (c) Broadband dipole antenna with big circular patches; (d) Broadband Monopole antenna in LTCC technology

B.3.3. Gain Measurements

Measurement Setup

For gain measurements carried out at TU Delft³, antenna pairs of the same type, have been used in the measurements, which are assumed to be identical in their characteristics. This is however not true generally, but for obtaining a first estimate for the antenna gain, this assumption is reasonable. The measurements are carried out in the time domain. For this reason a very narrow pulse is used. The used measurement equipment can generate a pulse of 50 ps width. The reference pulse used for calibration of the equipment is shown in Fig. B.13. We see that the pulse shows some ringing at the falling edge. However, for a pulse of this duration the pulse is reasonably well shaped. Additionally the pulse generator shows some signal at about 8 ns which is due to the pulse generation circuitry. For our

³Many thanks to Zoubir Irahhten for helping with the measurements

Appendix B. UWB Demonstrator

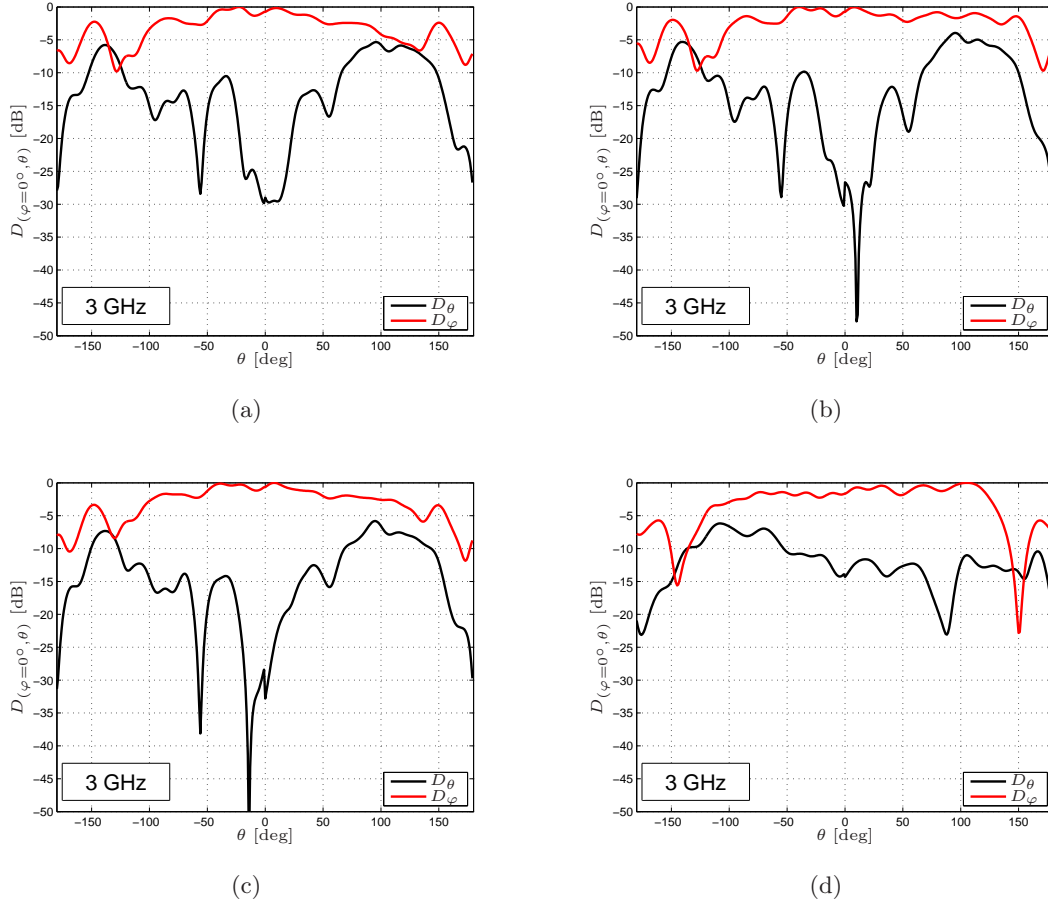


Figure B.11.: Polarization plots of the broadband antennas at 3 GHz: (a) Broadband dipole antenna with two elliptical patches; (b) Broadband dipole antenna with small circular patches; (c) Broadband dipole antenna with big circular patches; (d) Broadband Monopole antenna in LTCC technology

measurements these low reflections at this time are not interesting any more and don't influence the obtained measurement results. The sampling head used is working with the stroboscopic sampling principle. This means, that the pulse is transmitted periodically with a repetition frequency of 100 kHz and each time a single, slightly shifted sample is taken from the received pulse. Thus the exported measurements seem to have a sampling frequency of 200 GHz which is achieved by this special sampling technique.

For the different gain measurements this pulse shape was calibrated by simply interconnecting all the measurement cables and putting an attenuator with 30 dB to the sampling head to achieve proper amplitude scaling. Then this measured waveform was stored and used as a reference pulse.

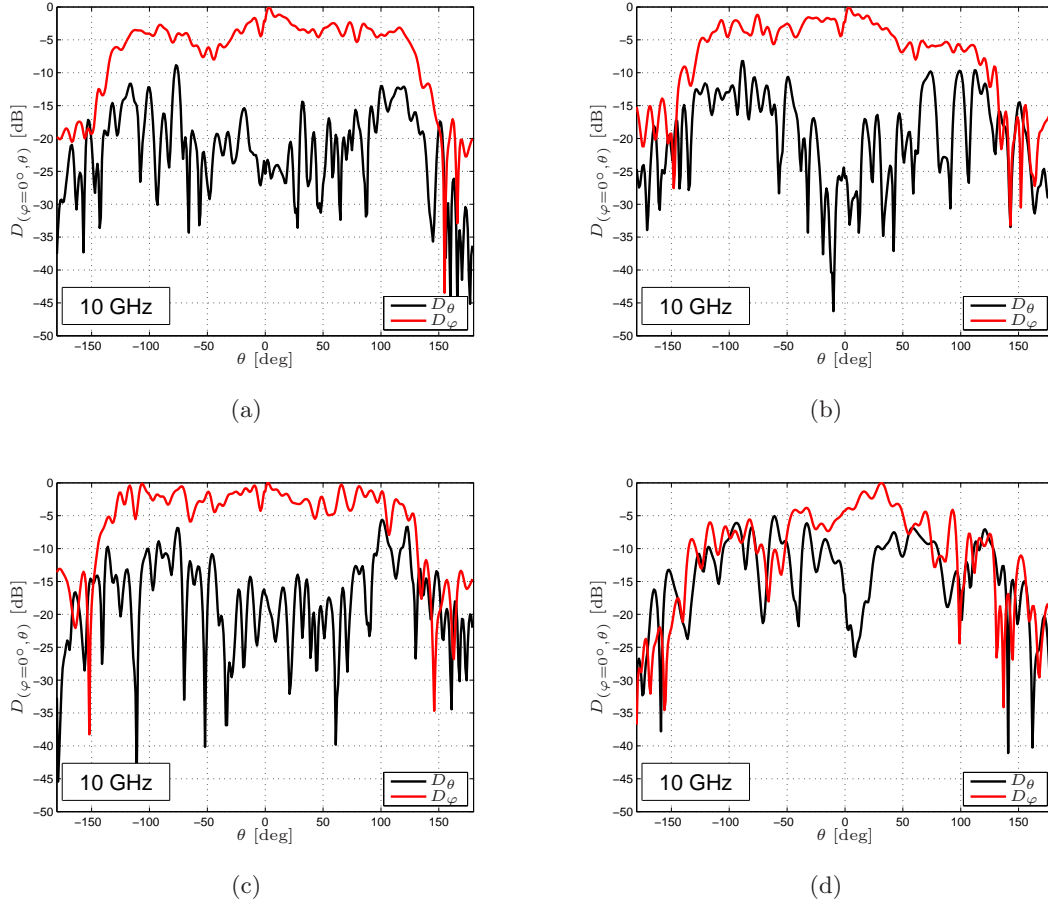


Figure B.12.: Polarization plots of the broadband antennas at 10 GHz: (a) Broadband dipole antenna with two elliptical patches; (b) Broadband dipole antenna with small circular patches; (c) Broadband dipole antenna with big circular patches; (d) Broadband Monopole antenna in LTCC technology

Gain Measurements

After this calibration measurement, the antennas response to the pulse omitting any multipath components, were measured. For that purpose the antennas have been separated by 1m to be in the far-field for these high frequencies. The pulse generator and the sampling head have been connected to either one of the antennas and the previously used attenuator has been removed. Since both of the two antennas are assumed to be equal, one can define the link budget for this system quite accurately. The received power $P_r(f)$ at the receiving antenna is given as

$$P_r(f) = P_t(f)G_{ant}^2(f)P_f(f), \quad (\text{B.4})$$

where $P_t(f)$ is the transmitted power, $G_{ant}(f)$ is the antenna gain, and $P_f(f)$ is the free space path loss. The free space path loss is further defined as

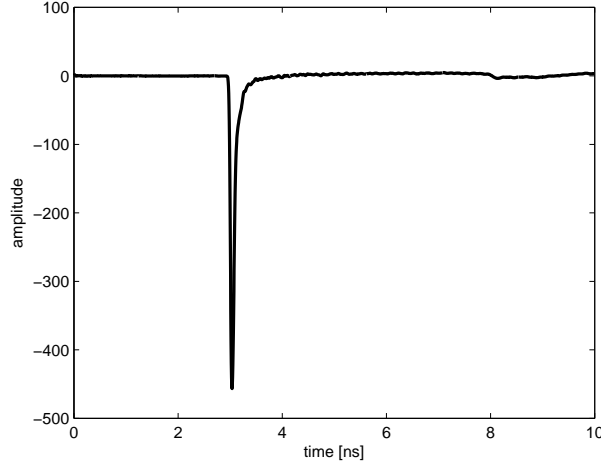


Figure B.13.: Reference Pulse used for calibration

$$P_f(f) = \left(\frac{\lambda}{4\pi d} \right)^2 = \left(\frac{c}{4\pi d f} \right)^2 \quad (\text{B.5})$$

where λ is the wavelength, d is the distance, c is the speed of light, and f is the frequency.

By substituting (B.5) into (B.4) and expressing the antenna gain, we obtain

$$G_{ant}(f) = \sqrt{\frac{P_r(f)}{P_t(f)P_f(f)}} = \frac{4\pi d}{c} f \frac{V_r(f)}{V_t(f)} \quad (\text{B.6})$$

where due to the square root the received and transmitted power can be replaced by the according voltages if they are using the same impedance. With these equations, the antenna gain can be easily computed for each frequency.

Measurement Scenarios

To determine the gain, we have measured several scenarios of arranging receiver and transmitter antenna. The most obvious task was to put both antennas in the same horizontal plane. The gain is then measured when both antennas are in upright position as shown in Fig. B.14(a). Furthermore the cross polarization of the antennas was measured. For that purpose, one of the antennas was rotated by 90° and the antenna feeding points have been adjusted again that they are in the same horizontal plane. This is depicted in Fig. B.14(b).

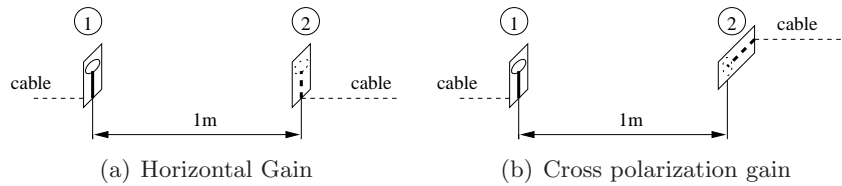


Figure B.14.: Scenarios for Gain measurements

In the measurement campaign we have compared the previously introduced antennas again (i.e., 2cent, 5cent, and EPCOS).

Measurement Results

Measurements were carried out in the time-domain with a very short pulse. This pulse, having a very broad spectrum was used to measure the antenna gain over frequency. However, some odd things appeared in the measurements which will be described later. First of all, the antenna gain measurements obtained when all antennas are mounted in an upright position are shown. Fig. B.15 shows the environment where the antennas were measured. The antennas were mounted with some tape to wooden pillars which were approximately 170cm high. For the cross-polarization measurements, a 90° bent connector has been used to achieve the rotation. If just one connector was used, the antenna feeding points are not in the same horizontal plane anymore thus one of the pillars had to be elevated during these measurements.



Figure B.15.: Gain measurements in lab

The first results for upright positions of the antennas are shown in Fig. B.16. One can see that the 2cent and 5cent antennas work reasonably well in the targeted frequencies for Ultra Wide-Band communications. The third antenna has a notch at app. 7 GHz and can thus be used only below or above these frequencies. However, it is very likely, that the connector of the antenna, which is actually quite close to the effective antenna is the reason for such a result.

After that we have rotated one antenna by 90° and elevated the wooden pillar to achieve

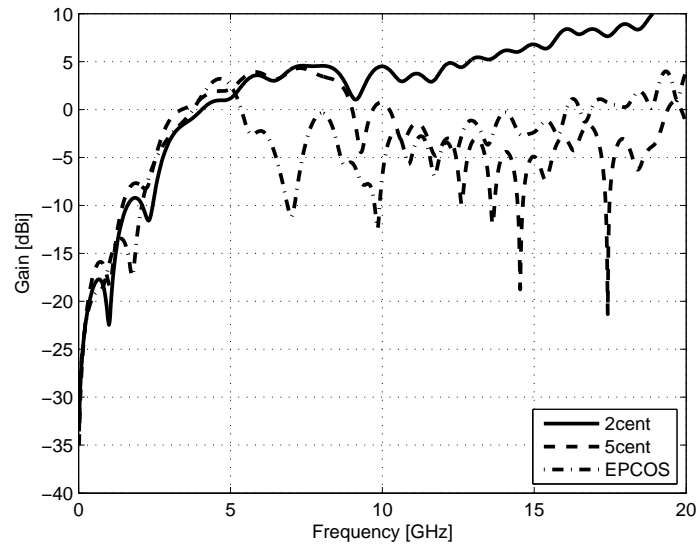


Figure B.16.: Comparison of the gain for different antennas

similar height for both antennas. The results are shown in Fig. B.17. It is seen clearly that the polarized waves are very well attenuated and a polarization of at least -5dB is achieved with these simple antennas with the coins and app. -10dB are achieved by the EPCOS antenna. One main reason for this result is that due to the asymmetric feeding to the symmetric dipole of the coins a common mode current exists in the feeding line. This current also propagates from the shield and contributes to a bad result when comparing the polarization measurements. To investigate the notch at 7 GHz for the EPCOS antennas a

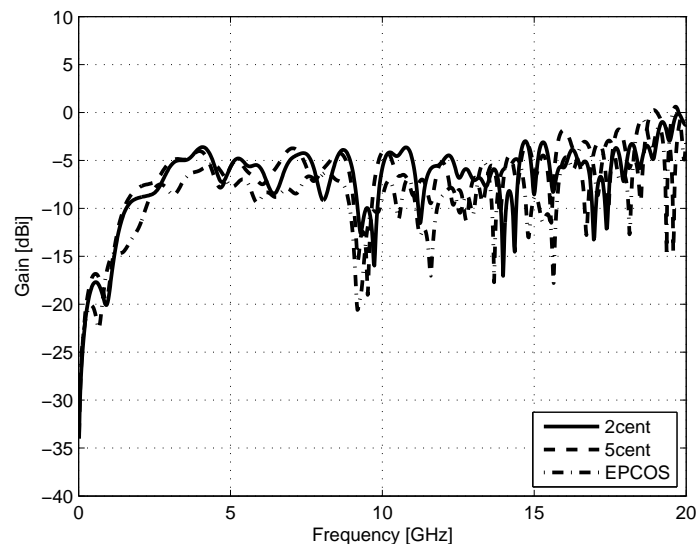


Figure B.17.: Comparison of the cross-polarization gain for different antennas

bit further, a second measurement has been carried out. The transmitter antenna was now the EPCOS antenna and the receiver antenna was replaced by a bi-conical antenna. This antenna is assumed to have flat gain response to be able to compare the measured results. The obtained measurements are shown in Fig. B.18. It is seen clearly, that the deep notch

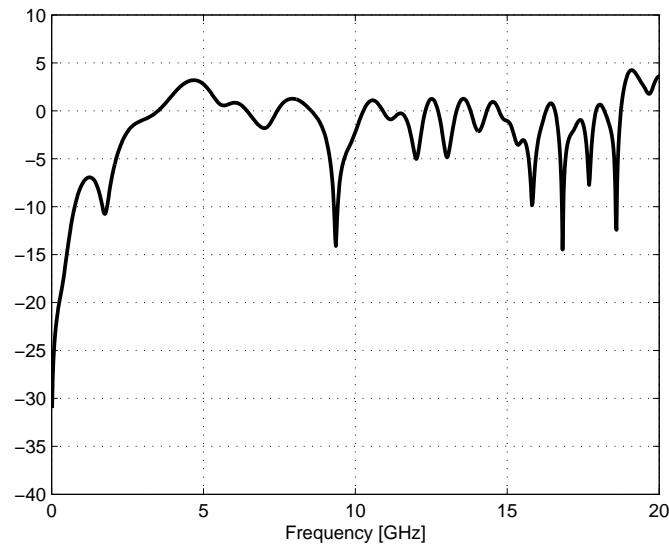


Figure B.18.: Reference measurement of EPCOS antenna with bi-conical antenna

at 7 GHz vanished for this setup. This is due to the fact that the bi-conical antenna has an almost flat gain response which is shown in Fig. B.19. Additionally, the two biconical

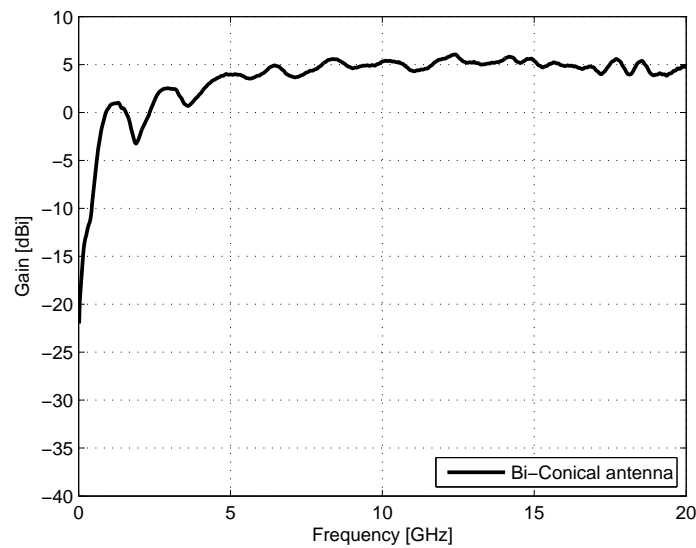


Figure B.19.: Biconical antenna gain

Appendix B. UWB Demonstrator

antennas are shown in Fig. B.20. The antennas used in this measurement campaign have



Figure B.20.: Biconical antennas

reasonable performance in the targeted frequency ranges for UWB. For lower frequencies, the coin antennas show weak results but still offer a gain of about 1-2 dBi (i.e., w.r.t an ideal isotropic radiator) over the frequency ranges from 3-5 GHz. In higher frequency ranges the simple coin antennas work even better, achieving a gain of almost 4 dBi for frequencies from 5.5-9 GHz. Conversely, the EPCOS antenna shows also reasonable performance in the low frequency regions (3-5 GHz), where it is almost comparable in performance to the two other antennas. However, for the frequency of 7 GHz, the antenna shows a deep notch in the gain which is most likely because of the measurement setup and the connectors mounted on the PCB of the antenna. The connectors are too closely mounted to the effective antenna and are assumed to interfere with the connectors, which have approximately the same size. However, a comparison measurement with an antenna with almost flat frequency response has been carried out as well. There it is seen, that the influence of having twice the connectors is certainly weakened and the notch is still present but flattened. The absolute gain value from this supporting measurement has not been calibrated because the main assumption for the measurements, i.e. that the antennas are approximately equal, is not possible in this scenario anymore, making a gain computation according to (B.6) not valid anymore.

Standardized UWB Channels

C.1. Statistical Channel Models

Analysis and design of wireless communication systems are based on the knowledge of the propagation characteristics. Radio propagation mechanisms in the mobile and indoor environments are rather complex. Propagating radio signals undergo attenuation by objects. Because of reflection, refraction and scattering, the transmitted wave arrives at the receiver through different paths having different amplitudes and phases. These are the three main effects which impact the description of a mobile radio channel. *Reflection* occurs when a propagating electromagnetic wave impinges on a smooth surface with large dimensions compared to the RF wavelength λ . Furthermore, *diffraction* occurs when the radio path between the transmitter and receiver is obstructed by a dense body with large dimensions compared to λ , causing secondary waves to be formed behind the obstructing body. Diffraction and reflection are phenomena that account for RF energy travelling from the transmitter to the receiver without a line-of-sight path between the two. Diffraction is often termed “shadowing”. *Scattering* occurs when a radio wave impinges on either a large rough surface or any surface whose dimensions are on the order of λ or less, causing the reflected energy to spread out in all directions [33,34]. In wideband pulse transmission this causes delayed and attenuated echoes of each transmitted pulse, which in digital communication systems results in inter-symbol interference and fading of the received signal power. This potentially limits the achievable data rate of the wireless transmission and strategies to mitigate fading have to be investigated. If the knowledge of the propagation effects could be incorporated and used in the receiver architecture, the performance of the communication system is improved. The characterization of the wireless radio propagation channel is based on the mathematical model of the channel, which can be defined either in the time- or in the frequency-domain. A good overview about UWB channel modeling is presented in [16] and is further extended in this document.

C.1.1. Description of Different Propagation Effects

In wireless communication systems it is necessary to test the proposed transceiver architectures with the occurring propagation channels. One approach to obtain these channels is to model the physical effects of a wireless propagation channel with an impulse response.

Appendix C. Standardized UWB Channels

These channel models can be either deterministic, stochastic or hybrid channel models, with their according advantages and disadvantages. If a wireless channel is modeled deterministically it is essential to know many parameters of the environment (i.e. positions of reflectors, scatterers, etc.). Thus, it is a very complex task to account for all possible reflections/scatterers which result in a multipath component at the receiver. One idea to simplify this approach is to generate a hybrid channel model which can be computed with a low number of parameters of the geometry (reflectors/scatterers). These geometric measures determine a grid of dominant rays in the channel impulse response but to lower the complexity, the adjacent regions of the impulse response are modeled stochastically. Conversely, statistical channel models just represent the average behavior of a channel, which possibly occurs in a real world situation. The major advantage of the statistical channel models is that only a small amount of statistical parameters is needed to generate one realization of a channel impulse response.

C.1.2. Statistical Modeling of the Path Loss Exponent

In general, if a signal is transmitted through free space, it undergoes attenuation. The received power $P_r(d)$ is dependent on the distance d between transmitter and receiver, and is given by Friis equation [33] as

$$P_r(d) = \frac{P_t G_t G_r \lambda^2}{(4\pi)^2 d^2} \quad (\text{C.1})$$

where P_t denotes the power of the transmitter, and G_r, G_t are the gains of the receiver and transmitter antennas, respectively. It is seen clearly, that the path loss is dependent on the distance d and on the wavelength λ of the transmitted wave, which is given by

$$\lambda = \frac{c}{f} = \frac{2\pi c}{\omega_c} \quad (\text{C.2})$$

where c is the propagation speed, i.e., the speed of light. In conventional narrowband systems the frequency-dependence is negligible because it remains approximately constant within the frequency range of interest. If a received signal shows fluctuations due to multipath or shadowing, a narrowband model approach is to define the pathloss as

$$G_{pr}(d, f_c) = \frac{\mathbb{E}\{P_{RX}(d, f_c)\}}{P_{TX}} \quad (\text{C.3})$$

where the expectation operator should cover an area which is large enough to allow averaging large-scale fading parameters (shadowing) and small-scale fading effects. Due to the huge bandwidth of UWB signals, the frequency dependence of the channel transfer function has to be considered. Thus it makes sense to define a frequency dependent path gain

$$G_{pr}(d, f) = \mathbb{E}\left\{\int_{f-\Delta f/2}^{f+\Delta f/2} |H(\tilde{f}, d)|^2 d\tilde{f}\right\} \quad (\text{C.4})$$

where $H(f, d)$ is the channel transfer function. It greatly simplifies the modeling of the path loss if we assume that the path gain is a function of distance and frequency which can be written as a product of terms

$$G_{pr}(d, f) = G_{pr}(f)G_{pr}(d). \quad (\text{C.5})$$

C.1. Statistical Channel Models

Considering the distance dependent path loss $G_{pr}(d)$ to be the same as in conventional narrowband systems the results obtained there are reused. For the path gain in dB we obtain that

$$G_{pr}(d) = G_{pr,0} + 10n \log_{10} \left(\frac{d}{d_0} \right) \quad (C.6)$$

where the reference distance d_0 is usually set to 1 m, and $G_{pr,0}$ is the path gain at the reference distance. The propagation exponent is denoted as n . Different values for the path loss exponent are obtained according to the environments where the path loss is measured. Additionally the pathloss exponent is different for line-of-sight (LOS) and non line-of-sight (NLOS) channels (*cf.* Table C.1) [112, 113, 114, 115, 116, 117].

	Environment	path loss exponent n
LOS	narrow corridor	1.0
	industrial env.	1.2
	office and residential env.	$\sim 1.5 - 2$
NLOS	industrial and outdoor env.	2 - 2.5
	office and residential env. (soft NLOS)	3 - 4
	indoor env. (hard NLOS)	4 - 7

Table C.1.: Path loss exponents for different environments

The frequency dependence of the path gain is usually given as

$$\sqrt{G_{pr}(f)} \propto f^{-\kappa} \quad (C.7)$$

where κ was evaluated by different measurement campaigns. The different parameter values are shown in Table C.2

Environment	Frequency dependence exponent κ
office env. (w. antenna eff.) [118]	0.8 - 1.4
industrial env. (w/o antenna eff.)	-1.4
residential env. (w/o antenna eff.)	+1.5

Table C.2.: Frequency dependence exponents for different environments

Since it is seen that the coefficient κ can have positive and negative values it would be useful to make similar model assumptions as for n , i.e. model it as a Gaussian random variable [17]. Up to this point nobody has further investigated this topic. Alternative models of the frequency dependence of the pathloss include a frequency-dependent pathloss exponent $n(f)$ and an exponential dependence $\log_{10}(PL(f)) \propto \exp(-\delta f)$, where δ is varying between 1.0 (LOS) and 1.4 (NLOS) [119].

C.1.3. Fading

One important physical phenomenon in a mobile radio channel is fading. A rough overview of different fading effects is shown in Fig. C.1. The fading phenomenon is separated in two different types of fading, namely *large-scale* fading and *small-scale* fading. Large-scale fading represents the average signal power attenuation or path loss due to motion over large areas. This is usually affected by terrain contours (hills, forrests, etc.) or in indoor environments by objects, walls, etc. between transmitter and receiver. The receiver is often referred to as being “shadowed” by different objects within the landscape. The statistics of large-scale fading provide a way of computing an estimate of the path loss as a function of distance. On the other hand, small-scale fading represents dramatic changes in signal amplitude and phase due to small changes in the environment (typically at half-wavelength dimension) between receiver and transmitter. The origin for small-scale fading (as depicted in Fig. C.1) is the dispersion of the mobile radio channel, leading to interference. Additionally, fading occurs due to time variance of the channel which is related to changes in the environment as moving objects or persons.

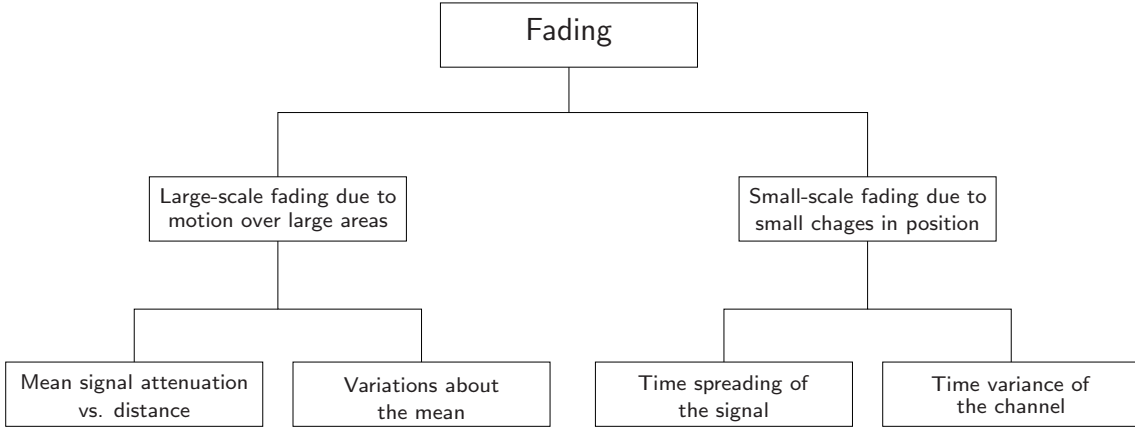


Figure C.1.: Overview of fading sources for mobile radio channels [120]

Statistical Modeling of Large-Scale Fading

Large-scale fading is defined as the variation of the local mean power around the path loss. Usually it is modeled to exhibit a lognormal distribution with different variances of the process for LOS (1-2 dB) and NLOS (2-6 dB) scenarios [116, 114, 115, 112, 117]. An important refinement of path loss modeling was introduced in [121] and applied to UWB systems in [122]. In their approach, the path loss exponent n is a random variable that changes from building to building but has a probability density function (pdf) which is well approximated by a Gaussian distribution. Thus they specified the mean and the variance of the distributions according to Table C.3.

Generally the pathloss exponent n in [122] is defined for eq. (C.6) as

$$n = \mu_n + n_1\sigma_n \tag{C.8}$$

where n_1 is a zero-mean Gaussian random variable with a variance of one, i.e. $n_1 \sim \mathcal{N}(0, 1)$. For distances larger than the reference distance d_0 the variations around the path loss are

Parameter	LOS		NLOS	
	Mean	Std. Dev.	Mean	Std. Dev.
$PL_0(\text{dB})$	47	NA	51	NA
μ_n	1.7	0.3	3.5	0.97
σ_n (dB)	1.6	0.5	2.7	0.98

Table C.3.: Parameters of the Ghassemzadeh pathloss model

modeled with a distance dependent random variable $S(d)$, i.e.

$$PL(d) = \left[PL_0 + 10n \log_{10} \left(\frac{d}{d_0} \right) \right] + S(d), \quad d \geq d_0, \quad (\text{C.9})$$

where $S(d)$ is mathematically represented by

$$S = n_2\chi, \quad \chi = \mu_\chi + n_3\sigma_\chi \quad (\text{C.10})$$

where n_2 and n_3 are zero-mean, unit variance Gaussian random variables. This yields a total attenuation (in dB) due to shadowing and path loss of

$$\overline{PL(d)} = [PL_0 + 10\mu_n \log_{10} d] + [10n_1\sigma_n \log_{10} d + n_2\mu_\chi + n_2n_3\sigma_\chi] \quad (\text{C.11})$$

Limitations to the Gaussian random variables n_1, n_2 and n_3 apply to avoid unphysical attenuation, i.e., n_1 is limited within $[-0.75, 0.75]$ and n_2, n_3 are limited to the interval $[-2, 2]$. The values for the pathloss at reference distance, mean and variance for the random variables used in eq. (C.11) are found in Table C.3. The frequency dependence is not modeled in [122].

Statistical Modeling of Small-Scale Fading

Usually the multipath propagation channel is described by the response of the channel to a single pulse. This means that all the multiple reflections are collected unless no detectable components of the pulse are occurring anymore. Thus, each component of the impulse response is defined by a delay τ_i and an amplitude α_i . The channel impulse response is given by the sum over all different components.

$$h(t) = \sum_{i=0}^N \alpha_i \delta(t - \tau_i) \quad (\text{C.12})$$

To describe small-scale fading, it is important to describe the statistical properties of the path gains α_i within a small area caused by the superposition of unresolvable components. In narrowband systems a tap of the impulse response in general represents a superposition of many paths, thus the central limit theorem is applicable and the complex path amplitudes exhibit a Gaussian distribution. For UWB systems the resolution in time is much higher and only a few components are superimposed for one distinct path. Due to the huge bandwidth it is also useless to define the impulse response of the system in complex

Appendix C. Standardized UWB Channels

baseband which is used in conventional narrowband systems. The impulse response is modeled in real baseband and the phase of the paths becomes irrelevant. Thus, other statistical distributions [123] have to be used to describe these effects which are

- Nakagami distribution with parameters m, Ω [124], [36]

$$p(r) = \frac{2m^m r^{2m-1}}{\Gamma(m)\Omega^m} \exp\left(-\frac{m}{\Omega}r^2\right)$$

It was found to fit the measurement results best in [125], [126].

- Rice distribution s, σ [127], [128]

$$p(r) = \frac{r}{\sigma^2} \exp\left(-\frac{r^2 + s^2}{2\sigma^2}\right) I_0\left(\frac{rs}{\sigma^2}\right)$$

It was used in [129] and [118], and describes the envelope of a sum of one dominant component and many smaller components.

- Lognormal distribution with parameters μ, σ [130]

$$p(r) = \frac{1}{r\sqrt{2\pi\sigma^2}} \exp\left(-\frac{(\log(r) - \mu)^2}{2\sigma^2}\right)$$

was suggested in [131]. One advantage is that the small-scale statistics and the large-scale statistics have the same form and the superposition of the two effects is modeled again with a lognormal variable.

- POCA and NAZU distribution [132], [133]

$$p(r) = r \frac{K^2(\nu)}{\sigma} \int_0^{2\pi} (x_0 + x_1 \cos(u) + x_2 \cos(2u) + x_3 \cos(3u) + x_4 \cos(4u))^{-(\nu+1)/2} du$$

where x_0, x_1, x_2, x_3 and x_4 are different polynomials which are found in the given references. It was suggested in [133] for modeling the small-scale fading of the channel.

- Weibull distribution with parameters α, β [130]

$$p(r) = \alpha\beta^{-\alpha} r^{\alpha-1} \exp\left(-\frac{r}{\beta}\right)^\alpha$$

is successfully used to describe the small-scale fading in [134] and [119].

- Rayleigh distribution [135] has been found suitable for some environments, even when the binwidth is very small. In [116] a Rayleigh fading was observed in an industrial environment (many metallic scatterers) even for 7.5 GHz measurement bandwidth. Also for the indoor measurements presented in [76], a Rayleigh distribution turns out to be a good model.

Another important aspect is the correlation of fading between different delays. Such a correlation can occur either if the wide-sense stationary uncorrelated scattering (WSSUS) model [136] is not valid anymore or per-pulse dispersion occurs. Per-pulse dispersion is a phenomenon which occurs if individual MPCs are distorted their and influence the adjacent bins, which results in correlated fading at these bins. This correlated fading could not be measured or observed in the channel measurements [125]. However, the authors in [76] observed this phenomenon.

C.1.4. General Shape of the Impulse Response

It has been recognized in many wideband channel measurements, that the rays tend to arrive within clusters. A model which considers these effects was proposed by *Saleh and Valenzuela* [137]. It allows the channel to consist of three different types of contributions. In their measurement campaign they used a 1.5 GHz CW signal which was modulated by a train of 10 ns pulses with a repetition period of 600 ns. Due to this fine resolution in time domain, they obtained a very accurate model for a wideband channel ($\sim 100\text{MHz}$). Generally, the complex lowpass equivalent impulse response [36] of a channel is given by

$$h(t) = \sum_k \beta_k e^{j\theta_k} \delta(t - \tau_k) \quad (\text{C.13})$$

which means that the channel consists of path gains β_k , phase shifts θ_k and delays τ_k . Saleh and Valenzuela defined a model which is also able to describe the clustering effect of the rays. Thus the impulse response of the SV model is given by

$$h_{sv}(t) = \sum_{l=0}^L \sum_{k=0}^K a_{k,l} \exp(j\theta_{k,l}) \delta(t - T_l - \tau_{k,l}) \quad (\text{C.14})$$

where $a_{k,l}$ denotes the weight of the k th component within the l th cluster, T_l is the delay of the l th cluster, $\tau_{k,l}$ is the delay of the k th multipath component (MPC) relative to the l th cluster arrival time T_l . The phases $\theta_{k,l}$ are uniformly distributed within $[0, 2\pi)$ for the bandpass system. K and L are the number of MPCs and the number of clusters, respectively. They can be fixed or modeled as a stochastic variable.

C.1.5. Path Interarrival Times

Several different models for interarrival times of the MPCs have been proposed.

- *Regularly-spaced arrival times* are useful for dense multipath profiles. Since the different multipath components are not resolvable, a regular grid is defined on which all resolvable MPCs have to lie, i.e. $T_l + \tau_{k,l} = i\Delta$ with Δ being the resolution of the grid and the variable i span cover the whole time axis which is spanned by the impulse response [116].
- *Poisson arrival times* are probably the most popular model for the arrival times within a cluster. The probability density function for the arrival of MPC path k at a certain time $\tau_{k,l}$ and conditioned on the arrival time of the previous MPC, i.e. $\tau_{k-1,l}$, is given as [137]

$$p(\tau_{k,l}|\tau_{k-1,l}) = \lambda_l \exp[-\lambda(\tau_{k,l} - \tau_{k-1,l})], k > 0 \quad (\text{C.15})$$

Appendix C. Standardized UWB Channels

where the arrival time of the first ray in each cluster is by definition positive, i.e., $\tau_{0,l} > 0$. The model proposed by Saleh and Valenzuela allows only a constant λ for all clusters which was also assumed for the 802.15.3a model (see Section C.2). However, measurements have shown that the arrival rate is larger for later clusters, thus λ_l for each cluster is used here.

- *Mixed Poisson processes* are used as a refinement for observations which occurred in the UWB channel measurements. The mixture of two Poisson processes fits the observations better than using a single Poisson process [138]. Thus the pdf of the interarrival times is given as

$$p(\tau_{k,l}|\tau_{k-1,l}) = \beta\lambda_1 \exp[-\lambda_1(\tau_{k,l} - \tau_{k-1,l})] + (\beta - 1)\lambda_2 \exp[-\lambda_2(\tau_{k,l} - \tau_{k-1,l})], k > 0 \quad (\text{C.16})$$

where β is the mixture probability and λ_1, λ_2 are the ray arrival rates.

C.1.6. Cluster Powers and Cluster Shapes

The *Power Delay Profile (PDP)* is given (assuming ergodicity) as the expectation of the squared value of the absolute taps of a channel impulse response, i.e.,

$$P(\tau) = \mathbf{E}_t\{|h(t, \tau)|^2\}. \quad (\text{C.17})$$

where τ denotes the delays to describe a single impulse response of a channel, and t denotes a possible variability of the channel over time [139]. The most common model for the power delay profile is that each cluster exhibits an exponential decay, i.e.,

$$\mathbf{E}\{|a_{k,l}|^2\} \propto \Omega_l \exp(-\tau_{k,l}/\gamma_l) \quad (\text{C.18})$$

where Ω_l is the integrated energy of the l th cluster, and γ_l is the intra-cluster decay constant. The cluster powers, averaged over the large-scale fading, follow an exponential decay

$$10 \log(\Omega_l) = 10 \log(\exp(-T_l/\Gamma)) \quad (\text{C.19})$$

where Γ is the inter cluster decay time constant. Additionally the interarrival times of the clusters are also modeled by a Poisson process

$$p(T_l|T_{l-1}) = \Lambda \exp[-\Lambda(T_l - T_{l-1})], l > 0 \quad (\text{C.20})$$

where Λ is the cluster arrival rate.

With the shown model assumptions it is possible to model a huge range of wideband channels, thus this model is widely used. A UWB channel is somewhat different in its behavior. It is necessary to account for these special properties which were observed in the measurement campaigns [129, 140, 141].

- The first component of a cluster can show stronger power than the one given by eq. (C.18). In conventional narrowband systems this is only true for the first path of the first cluster, i.e. the LOS component. In UWB systems this is also possible in more than one cluster due to specular reflections in later clusters.

C.2. Parameters of the IEEE 802.15.3a Channel Model

- The cluster decay rates γ_l depend on the delay of the cluster. A possible solution to achieve this is with a linear increase of γ_l with the cluster delay [116]

$$\gamma_l \propto k_\gamma T_l + \gamma_0 \quad (\text{C.21})$$

- The cluster powers show random variations around the value given by eq. (C.19) due to shadowing effects and are modeled with a lognormal distribution.
- The small scale averaged cluster shape is not strictly monotonous but shows a “fine structure”, i.e., deviations from the exponential decay. Thus a random variable $s(\tau_{k,l})$ for eq. (C.18) helps to model this observed effect [122].
- In some environments the cluster shape does not show a sharp onset but rather a first gradual increase until a local maximum is reached and then a decrease. Thus an alternative PDP shape has been suggested for that case [17]

$$E\{|a_{k,l}|^2\} \propto (1 - \xi \exp(-\tau_{k,l}/\gamma_{rise})) \exp(-\tau_{k,l}/\gamma_1) \quad (\text{C.22})$$

C.2. Parameters of the IEEE 802.15.3a Channel Model

The IEEE has formed a standardization group, IEEE 802.15.3a, which has proposed a standardized channel model for UWB Personal Area Networks (PAN) communication systems [4]. The aim of the high data rate standardization group (TG3a) was to define channel models which are representative for the typical behavior of a wireless UWB channel in different scenarios at short distance. The data rates for the 3a standard are up to 110 Mbps at 10m distance, 200 Mbps at 4m distance and higher datarate at lower distance. It is very essential to have standardized stochastic channel models which represent the physical effects to make a fair comparison between different transceiver structures.

C.2.1. The Model

The 802.15.3a standardization group has proposed the following channel model which consists of the following discrete time impulse response

$$h(t) = X \sum_{l=0}^L \sum_{k=0}^K \alpha_{k,l} \delta(t - T_l - \tau_{k,l}) \quad (\text{C.23})$$

where $\{\alpha_{k,l}\}$ are the multipath coefficients, $\{T_l\}$ is the delay of l th cluster, $\{\tau_{k,l}\}$ is the delay of the k th multipath component relative to the l th cluster. The variable $\{X\}$ represents the log-normal shadowing. Similarly to the Saleh/Valenzuela model the cluster arrival times T_l and ray arrival times $\tau_{k,l}$ exhibit a Poisson distribution which are specified by the pdf

$$p(T_l|T_{l-1}) = \Lambda \exp[-\Lambda(T_l - T_{l-1})], l > 0 \quad (\text{C.24})$$

and

$$p(\tau_{k,l}|\tau_{k-1,l}) = \lambda \exp[-\lambda(\tau_{k,l} - \tau_{k-1,l})], k > 0 \quad (\text{C.25})$$

Appendix C. Standardized UWB Channels

where T_l is the arrival rate of the first path in the l th cluster, Λ is the cluster arrival rate, and λ denotes the ray arrival rate. The channel coefficients are defined as

$$\alpha_{k,l} = p_{k,l} \xi_l \beta_{k,l} \quad (\text{C.26})$$

where $p_{k,l}$ is a random variable with equal probability for $+1$ and -1 representing signal inversion due to reflection, ξ_l reflects the fading associated with the l th cluster, and $\beta_{k,l}$ corresponds to the fading associated with the k th ray of the l th cluster. The path gains exhibit a lognormal distribution, i.e.,

$$20 \log_{10}(\xi_l \beta_{k,l}) \propto \mathcal{N}(\mu_{k,l}, \sigma_1^2 + \sigma_2^2) \quad (\text{C.27})$$

or equivalently

$$|\xi_l \beta_{k,l}| = 10^{(\mu_{k,l} + n_1 + n_2)/20} \quad (\text{C.28})$$

where n_1 and n_2 are zero-mean Gaussian random variables with variances σ_1^2 and σ_2^2 , which represent the fading on each cluster and each ray, respectively. The average PDP is given as

$$\mathbb{E}\{|\xi_l \beta_{k,l}|^2\} = \Omega_0 e^{-T_l/\Gamma} e^{-\tau_{k,l}/\gamma}, \quad (\text{C.29})$$

where Ω_0 is the mean energy of the first path of the first cluster and Γ , γ are the cluster and ray decay factor, respectively. The mean of the lognormal distribution is given by

$$\mu_{k,l} = \frac{10 \log(\Omega_0) - 10T_l/\Gamma - 10\tau_{k,l}/\gamma - (\sigma_1^2 + \sigma_2^2) \log(10)}{\log(10)} \quad (\text{C.30})$$

Finally, since the lognormal shadowing of the total multipath energy is captured by the term X_i , the total energy contained in the terms $\{\alpha_{k,l}^i\}$ is normalized to unity for each realization. The shadowing is modeled as a lognormal distributed random variable, i.e.,

$$20 \log_{10}(X_i) \propto \mathcal{N}(0, \sigma_x^2) \quad (\text{C.31})$$

C.2.2. Channel Parameters

The goal of the 802.15.3a standardization task group was to develop a standard channel model for high data rate communication. They also specified four different parameter sets to generate the channels with the equations shown in the previous subsection. The different channel models are labeled CM1 - CM4 and represent different scenarios. CM1 is an LOS channel for the range of 0-4m distance. Conversely, CM2 and CM3 are representing NLOS channels with distances of 0-4m and 4-10m, respectively. CM4 is a “worst-case” scenario for an NLOS channel which has a very dense multipath structure. Additionally the channel models are also characterized by their RMS delay spread [137] which is given by

$$\tau_{rms} = \sqrt{\overline{\tau^2} - (\overline{\tau})^2} \quad (\text{C.32})$$

where each moment of the PDP is computed as

$$\overline{\tau^n} = \frac{\sum_k \tau_k^n \alpha_k^2}{\sum_k \alpha_k^2}, \quad n = 1, 2. \quad (\text{C.33})$$

C.3. The IEEE 802.15.4a Channel Model

Target Channel Characteristics	CM1	CM2	CM3	CM4
τ_m [ns] (Mean excess delay)	5.05	10.38	14.18	
τ_{rms} [ns] (rms delay spread)	5.28	8.03	14.28	25
NP10dB (number of paths within 10 dB of the strongest path)			35	
NP (85%) (number of paths that capture 85% of the channel energy)	24	36.1	61.54	
Model Parameters				
Λ [1/ns] (cluster arrival rate)	0.0233	0.4	0.0667	0.0667
λ [1/ns] (ray arrival rate)	2.5	0.5	2.1	2.1
Γ (cluster decay factor)	7.1	5.5	14	24
γ (ray decay factor)	4.3	6.7	7.9	12
σ_1 [dB] (std. dev. of cluster lognormal fading)	3.4	3.4	3.4	3.4
σ_2 [dB] (std. dev. of ray lognormal fading)	3.4	3.4	3.4	3.4
σ_x [dB] (std. dev. of lognormal fading term for total multipath realizations)	3	3	3	3
Model Characteristics for 167ps sampling time				
τ_m [ns]	5.0	9.9	15.9	30.1
τ_{rms} [ns]	5	8	15	25
NP10dB	12.5	15.3	24.9	41.2
NP (85%)	20.8	33.9	64.7	123.3
Channel energy mean [dB]	-0.4	-0.5	0.0	0.3
Channel energy std. dev. [dB]	2.9	3.1	3.1	2.7

Table C.4.: Parameters for the different channel models in the 802.15.3a standard [4]

The moment is obtained from the general definition of the impulse response shown in (C.12). The different parameters of the channel models are shown in Table C.4.

We see from Table C.4 that for a measurement bandwidth of 6 GHz (167 ps time resolution) the quantities like the RMS delay spread and other channel parameters are quite accurate compared to the target channel characteristics. For the target channel characteristics many values of representative quantities of the PDP are not even specified. Especially in CM4 where the definition of the model is said to be just a “worst case” scenario which should represent a very dense multipath channel.

C.3. The IEEE 802.15.4a Channel Model

The 802.15.4a standardization group has been developing a standard for UWB systems with low data rates and geolocation capabilities. Since the 802.15.3a standard only covers indoor environments for wireless personal area networks (WPANs) a lot of effects which are occurring in other scenarios are not covered in the 3a standard. Additionally, several effects are included in the model, which potentially increase the model accuracy, but on the other hand also increase the model complexity. Apart from the model accuracy, three different scenarios have been defined.

- *4a HF* covers the same frequency range as the 802.15.3a channel, i.e., 3.1GHz to

Appendix C. Standardized UWB Channels

10.6GHz with several different scenarios.

- *4a LF* covers the frequency range from 100MHz to 1000MHz.
- *4a Body Area Network (BAN)* is a special case which tries to model the propagation channel between two devices mounted on the human body.

Furthermore, a lot of different environments have been defined, i.e.,

- residential indoor
- office indoor
- industrial
- outdoor
- farm environments

In these different environments the specifications are done for an LOS and an NLOS scenario – the only exception is the farm environment which has only an NLOS scenario defined. Generally all the models are based on measurement campaigns. The model consists of a generalized Saleh/Valenzuela model [137]. Again the farm environment is excluded of the general model description because the model could not be fit into the measurements properly.

C.3.1. The Model

The path loss of the model is considered to be frequency and distance dependent. The distance dependence and frequency dependence are given by eq. (C.6) and (C.7), respectively. Shadowing is **not** included in the model for reasons that are related to specific simulation requirements in the 15.4a standardization. The generalizations of the Saleh/Valenzuela model include

- The number of clusters exhibits a Poisson distribution, where the mean \bar{L} is a model parameter.
- For some of the environments the cluster decay constant is linearly time dependent (C.21).
- For some NLOS environments (office and industrial), the PDP is not exponentially decaying but is given by (C.22)
- For indoor residential and office environments, the path arrival is given by a mixed Poisson distribution (*cf.* (C.16)).
- For industrial environments the channel model is a dense multipath channel. This means that each path contains a significant amount of energy and the rather complex description with clusters is not feasible anymore. For that case a tapped delay line model is used.

C.3. The IEEE 802.15.4a Channel Model

The small-scale fading of the amplitudes is modeled with a Nakagami distribution, where the parameter m of the distribution is independent of the delay, with the exception of the first component. It can have a higher m -factor. The parameter sets for the different environments are collected in Table C.5 and Table C.6.

Appendix C. Standardized UWB Channels

	Residential ¹		Indoor Office ²	
	LOS	NLOS	LOS	NLOS
Path loss				
PL_0 [dB]	43.9	48.7	36.6	51.4
n	1.79	4.58	1.63	3.07
S [dB]	2.22	3.51	-	-
σ_S	-	-	1.9	3.9
A_{ant} [dB]	3	3	3	3
κ [dB/octave]	1.12 ± 0.12	1.53 ± 0.32	-3.5	5.3
Power delay profile				
\bar{L}	3	3.5	5.4	1
Λ [1/ns]	0.047	0.12	0.016	NA
λ_1, λ_2 [1/ns], β	1.54, 0.15, 0.095	1.77, 0.15, 0.045	0.19, 2.97, 0.0184	NA
Γ [ns]	22.61	26.27	14.6	NA
k_γ	0	0	0	NA
γ_0 [ns]	12.53	17.50	0	NA
$\sigma_{cluster}$ [dB]	2.75	2.93	-	NA
Small-scale fading				
m_0 [dB]	0.67	0.69	0.42	0.5
k_m	0	0	0	0
\hat{m}_0 [dB]	0.28	0.32	0.31	0.25
\hat{k}_m	0	0	0	0
\tilde{m}_0	NA: all paths have	same m-factor distribution	-	-
χ	-	-	NA	0.86
γ_{rise}	-	-	NA	15.21
γ_1	-	-	NA	11.84

Table C.5.: Parameters for the residential and indoor office environments in the 802.15.4a standard [17]

¹valid up to 20 m (10 GHz), based on measurements in [142]

²valid up to 28 m (2-8 GHz), based on measurements in [114]

C.3. The IEEE 802.15.4a Channel Model

	Outdoor ¹		Open Outdoor ²
	LOS	NLOS	NLOS
Path loss			
PL_0 [dB]	43.29	43.29 ³	48.96
n	1.76	2.5 ³	1.58
σ_S [dB]	0.83	2 ³	3.96
A_{ant} [dB]	3	3	3
κ [dB/octave]	-1.6	0.4 ³	-
Power delay profile			
\bar{L}	13.6	10.5	3.31
Λ [1/ns]	0.048	0.0243	0.0305
λ_1, λ_2 [1/ns], β	0.27, 2.41, 0.0078	0.15, 1.13, 0.062	0.0225, 0, 0
Γ [ns]	31.7	104.7	56
k_γ	0	0	0
γ_0 [ns]	3.7	9.3	0.92
$\sigma_{cluster}$ [dB]	-	-	-
Small-scale fading			
m_0 [dB]	0.77	0.56	4.1
k_m	0	0	0
\hat{m}_0 [dB]	0.78	0.25	2.5
\hat{k}_m	0	0	0
\tilde{m}_0	-	-	0
χ	NA	NA	NA
γ_{rise}	NA	NA	NA
γ_1	NA	NA	NA

Table C.6.: Parameters for the outdoor and open outdoor environments in the 802.15.4a standard [17]

¹valid up to 17 m (3-6 GHz), based on measurements in [114]

²Model extracted based on measurements in a snow-covered open area

³educated guess

Appendix C. Standardized UWB Channels

Kronecker Product and Correlation Matrix for the Second-Order Equalizer

D.1. Commutation of the Kronecker Product

The Kronecker product of vectors is not commutative, which means that if the operands are exchanged a different result is obtained. However, it is always possible to find a permutation matrix \mathbf{P} that achieves

$$\mathbf{c} = \mathbf{a} \otimes \mathbf{b} \equiv \mathbf{P}(\mathbf{b} \otimes \mathbf{a}). \quad (\text{D.1})$$

If we assume that \mathbf{a} is an $m \times 1$ vector and \mathbf{b} is an $n \times 1$ vector, \mathbf{c} is an $mn \times 1$ vector. Thus, a valid permutation matrix has to be an $mn \times mn$ matrix.

If we assume that \mathbf{E}_{xy} is a matrix with dimensions $m \times n$ filled up with zeros, except for a single 1 at the position (x, y) we can express the permutation matrix as

$$\mathbf{P} = [\text{vec}(\mathbf{E}_{11}), \text{vec}(\mathbf{E}_{12}), \dots, \text{vec}(\mathbf{E}_{mn})], \quad (\text{D.2})$$

where $\text{vec}(\cdot)$ is denoting the vector operator, i.e., the operator that stacks a matrix into a vector columnwise [143].

D.2. Correlation Matrix of the Data Terms

In this section we derive an analytical description for the correlation matrix \mathbf{R}_r . Since it contains all different correlations between data terms up to eighth order we can give a set of rules how to create this matrix in a systematic way. First of all, we describe the correlation matrix a bit more explicitly. The correlation between the data terms is given as $\mathbf{E}\{\mathbf{r}[k]\mathbf{r}^T[k]\}$ where each of the data terms is given as $\mathbf{r}[k] = [\mathbf{s}^T[k], (\mathbf{s}[k] \otimes \mathbf{s}[k])^T]^T$ and $\mathbf{s}[k]$ can be expressed as $\mathbf{s}[k] = [\mathbf{d}_x^T[k], (\mathbf{d}_x[k] \boxtimes \mathbf{d}_x[k])^T]^T$. Substituting this, we obtain

$$\begin{aligned} \mathbf{r}[k] = & \left[\mathbf{d}_x^T[k], (\mathbf{d}_x[k] \boxtimes \mathbf{d}_x[k])^T, \right. \\ & \left. [\mathbf{d}_x^T[k], (\mathbf{d}_x[k] \boxtimes \mathbf{d}_x[k])^T] \otimes [\mathbf{d}_x^T[k], (\mathbf{d}_x[k] \boxtimes \mathbf{d}_x[k])^T] \right]^T. \end{aligned} \quad (\text{D.3})$$

Appendix D. Correlation Matrix for the Second-Order Equalizer

To determine the autocorrelation matrix, the expectation operator of the outer product of (D.3) with itself has to be computed. If one studies the structure of the data products in detail, one can see that the matrix consists of sections with products of different orders. To analyze these products stepwise, we separate the correlation matrix in four parts, like

$$\mathbf{R}_r = \begin{bmatrix} \mathbf{R}_1 & \mathbf{R}_2 \\ \mathbf{R}_2^T & \mathbf{R}_3 \end{bmatrix} \quad (\text{D.4})$$

where the separating line between the parts is drawn right after the fourth-order parts. Since the data vector up to the fourth-order products is defined with the reduced Kronecker notation, \mathbf{R}_1 is exactly the same as \mathbf{R}_s used for the linear equalizer. For the higher-order terms, contained in \mathbf{R}_2 and \mathbf{R}_3 , we can define conditions which have to be computed for each element and then it can be decided whether there is correlation between the terms or not. For the following, we assume that all the processes are stationary. Thus we drop the time index k of the data vectors. Furthermore, in each element of \mathbf{R}_2 and \mathbf{R}_3 we get a certain amount of data symbols contributing. Under assumption A1, we can say, that for each element in the correlation matrix where an odd number of data symbols is contributing, the resulting correlation is zero. For an even number of contributing symbols, we can define conditions which have to be fulfilled such that there is correlation between the data symbols, otherwise also these data symbols are uncorrelated.

Generally, the amount of different conditions which have to be checked is huge in this case. However, this problem is very similar with a set partitioning problem in combinatorics [144]. There, Bell has specified a number (i.e., the Bell number) which gives the number of partitioned sets of one dataset. For our problem not all different subsets are interesting. We just want to focus on the subsets which are contributing something different from zero to the autocorrelation matrix of the data vector.

For the correlation of two data symbols, we have exactly one case where this condition is fulfilled. There the contribution in the autocorrelation matrix is $\mathbf{E}\{d_i d_j\} = c^2$ for $i = j$, where d_i is the i -th element of $\mathbf{d}_x[k]$. If we consider four symbols, we get already four matches which contribute a different value than zero to the correlation matrix. These four cases are split in three sets of two data symbols and one set of four data symbols. Considering six data symbols, generally gives 31 different possible conditions. These 31 split to 15 where we have three pairs of data symbols, 15 where we have one pair of data symbols and one quad of data symbols, and one single six-element entry. For the eight-data-symbol case we have generally 374 subsets of the 4140 (the Bell number B_8) that contribute. There we find 103 terms consisting of four pairs, 210 terms consisting of a group of four and two pairs, 25 terms consisting of a pair and a group of six elements, 35 terms consisting of two groups of four and one single entry which is consisting of a group of eight. This totally gives 374 different conditions and by superimposing the other contributions with less than eight elements, we get a total number of 410 different possibilities to get a contribution in the autocorrelation matrix which is different from zero. To clarify the grouping, we depict the conditions once again in (D.5) where the different permutations are obtained when shifting indices.

Similar considerations are possible for the two other correlation matrices $\mathbf{R}_{s,n}$ and \mathbf{R}_m

D.2. Correlation Matrix of the Data Terms

$$\begin{aligned}
 \mathbf{E}\{d_i d_j\} &= c^2 && \text{if } i = j && 1 \\
 \mathbf{E}\{d_i d_j d_k d_l\} &= c^4 && \left\{ \begin{array}{l} \text{if } i = j \wedge k = l \\ \vdots \\ \text{if } i = j = k = l \end{array} \right. && 4 \\
 \mathbf{E}\{d_i d_j d_k d_l d_m d_n\} &= c^6 && \left\{ \begin{array}{l} \text{if } i = j \wedge k = l \wedge m = n \\ \vdots \\ \text{if } i = j = k = l \wedge m = n \\ \vdots \\ \text{if } i = j = k = l = m = n \end{array} \right. && 31 \\
 \mathbf{E}\{d_i d_j d_k d_l d_m d_n d_o d_p\} &= c^8 && \left\{ \begin{array}{l} \text{if } i = j \wedge k = l \wedge m = n \wedge o = p \\ \vdots \\ \text{if } i = j = k = l \wedge m = n \wedge o = p \\ \vdots \\ \text{if } i = j = k = l = m = n \wedge o = p \\ \vdots \\ \text{if } i = j = k = l \wedge m = n = o = p \\ \vdots \\ \text{if } i = j = k = l = m = n = o = p \end{array} \right. && 374
 \end{aligned} \tag{D.5}$$

and similar conditions can be formulated for the correlation terms of noise and data samples, i.e., the entries in the correlation matrix.

To show the complicated structure of such a correlation matrix, we have generated an example for the case where channel and equalizer have the same length of 6 taps. One can observe some regularity in this matrix. Each element containing a value different from zero is visualized with a dot. The matrix has $2652 \times 2652 = 7033104$ entries. However, only 22152 of them are non-zero, allowing sparse matrix computations reducing computational complexity.

Appendix D. Correlation Matrix for the Second-Order Equalizer

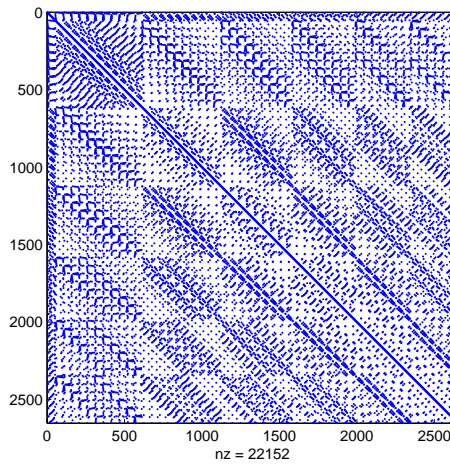


Figure D.1.: Autocorrelation matrix of the data vector $\mathbf{r}[k]$. The matrix has 2652×2652 elements, where 22152 are non-zero which reduces computational because of the sparsity.

Derivation of the Compensation Filters

To compensate for the mismatch spectra, an M -periodic time-varying filter $g_n[l]$, which relates the input $\hat{x}[n]$ to the output $x[n]$ is used. This filter is given as

$$x[n] = \sum_{l=-\infty}^{\infty} g_n[l] \hat{x}[n-l]. \quad (\text{E.1})$$

The filter digitally predistorts the digital output signal before digital-to-analog conversion and compensates therefore for the periodic nonuniform holding effects. Since $g_n[l]$ is periodic with M , we can represent it as the inverse discrete Fourier transform (IDFT)

$$g_n[l] = \sum_{k=0}^{M-1} \check{g}_k[l] e^{jkn \frac{2\pi}{M}} \quad (\text{E.2})$$

with the DFT

$$\check{g}_k[l] = \frac{1}{M} \sum_{n=0}^{M-1} g_n[l] e^{-jkn \frac{2\pi}{M}}. \quad (\text{E.3})$$

In accordance with (3.18) and different from the common definition [31], we have the normalization factor $1/M$ in the DFT. After substituting (E.2) in (E.1), we can write

$$\begin{aligned} x[n] &= \sum_l \sum_{k=0}^{M-1} \check{g}_k[l] e^{jkn \frac{2\pi}{M}} \hat{x}[n-l] \\ &= \sum_{k=0}^{M-1} \left(\sum_{l=-\infty}^{\infty} \check{g}_k[l] \hat{x}[n-l] \right) e^{jk \frac{2\pi}{M} n}. \end{aligned} \quad (\text{E.4})$$

The discrete-time Fourier transform (DTFT) of (E.4) gives

$$X(e^{j\omega}) = \sum_{k=0}^{M-1} \check{G}_k(e^{j(\omega-k\frac{2\pi}{M})}) \hat{X}(e^{j(\omega-k\frac{2\pi}{M})}) \quad (\text{E.5})$$

Appendix E. Derivation of the Compensation Filters

where

$$\check{G}_k(e^{j\omega}) = \frac{1}{M} \sum_{n=0}^{M-1} G_n(e^{j\omega}) e^{-jkn \frac{2\pi}{M}} \quad (\text{E.6})$$

is the DTFT of (E.3). Because the time-varying filter $g_n[l]$ precompensates the signal in the digital domain, it can only affect the analog output signal of the DAC within a bandwidth of $2\pi/T_s$. In practice, we will choose the fundamental band between $-\pi/T_s$ and π/T_s , but theoretically we could compensate for any higher-order band. The continuous-time output given by (3.17) can be represented within the fundamental band in discrete-time as [31]

$$Y(e^{j\omega}) = \sum_{k=0}^{M-1} \check{H}_k(e^{j\omega}) X \left(e^{j(\omega - k \frac{2\pi}{M})} \right) \quad (\text{E.7})$$

with

$$\check{H}_k(e^{j\omega}) = \check{H}_k \left(j \frac{\omega}{T_s} \right) \quad |\omega| \leq \pi, \quad (\text{E.8})$$

where it is assumed, without loss of generality, that $T=1$. Thus, after ideal digital-to-analog conversion the spectrum given in (E.7) is identical to the spectrum in (3.17) within the fundamental band. Substituting the output of the filter (E.5) in (E.7) results in the output

$$\begin{aligned} Y(e^{j\omega}) &= \sum_{k_1=0}^{M-1} \sum_{k=0}^{M-1} \check{H}_{k_1}(e^{j\omega}) \check{G}_k(e^{j(\omega - (k_1+k) \frac{2\pi}{M})}) \\ &\quad \times X \left(e^{j(\omega - (k_1+k) \frac{2\pi}{M})} \right). \end{aligned} \quad (\text{E.9})$$

The precompensation filter and the discrete-time model of the holding signal is illustrated in Fig. E.1(a) for the two-periodic case. With $l = k_1 + k$ one can simplify (E.9) to

$$\begin{aligned} Y(e^{j\omega}) &= \sum_{k=0}^{M-1} \sum_{l=k}^{M-1+k} \check{H}_{l-k}(e^{j\omega}) \check{G}_k(e^{j(\omega - l \frac{2\pi}{M})}) \\ &\quad \times X \left(e^{j(\omega - l \frac{2\pi}{M})} \right) \\ &= \sum_{l=0}^{M-1} \sum_{k=0}^{M-1} \check{H}_{l-k}(e^{j\omega}) \check{G}_k(e^{j(\omega - l \frac{2\pi}{M})}) \\ &\quad \times X \left(e^{j(\omega - l \frac{2\pi}{M})} \right) \end{aligned} \quad (\text{E.10})$$

where the periodicity of $\check{H}_{l-k}(e^{j\omega})$ has been exploited. Thus, the overall transfer function can be expressed as

$$Y(e^{j\omega}) = \sum_{l=0}^{M-1} \check{F}_l \left(e^{j(\omega - l \frac{2\pi}{M})} \right) X \left(e^{j(\omega - l \frac{2\pi}{M})} \right) \quad (\text{E.11})$$

with

$$\check{F}_l(e^{j\omega}) = \sum_{k=0}^{M-1} \check{H}_{l-k}(e^{j(\omega + l \frac{2\pi}{M})}) \check{G}_k(e^{j\omega}), \quad (\text{E.12})$$

E.1. Two-Periodic Nonuniform Holding Signals

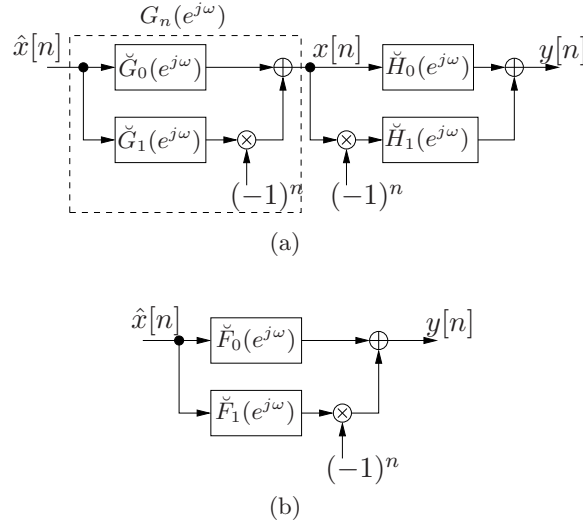


Figure E.1.: Illustration of the used compensation model for $M=2$. (a) Time-varying compensation filter $G_n(e^{j\omega})$ and the discrete-time model of a two-periodic nonuniform holding signal. (b) Transfer function of the combined system.

as it is shown in Fig. E.1(b) for the two-periodic case. From multi-rate theory one knows that a system is defined as a perfect reconstruction system if the output is the scaled and delayed version of the input [145]. In our compensation problem any attenuation of the output signal leads to a reduced dynamic and any amplification of the output signal can cause unwanted overflows with saturation effects. Therefore, unity gain of the overall system is required. Applying these definitions to (E.11) perfect reconstruction is obtained if

$$\check{F}_l \left(e^{j(\omega - l\frac{2\pi}{M})} \right) = \begin{cases} e^{-j\omega\Delta}, & \text{for } l = 0 \\ 0, & \text{for } l = 1, 2, \dots, M-1 \end{cases} \quad (\text{E.13})$$

where Δ is the delay of the system. If (E.13) is fulfilled all mismatch spectra are canceled and furthermore the $\sin(x)/x$ distortions in the fundamental band are equalized. The time-varying filter $g_n[l]$ can be efficiently implemented as an M -channel maximally decimated multi-rate filter bank [145].

E.1. Two-Periodic Nonuniform Holding Signals

For the two-periodic case, i.e., $M = 2$ we can quickly derive the filters in a closed form.

E.1.1. Solution of the Matrix Equation

By expressing (E.11), (E.12), and (E.13) in matrix notation one obtains

$$\begin{bmatrix} e^{-j\omega\Delta} \\ 0 \end{bmatrix} = \begin{bmatrix} \check{H}_0(e^{j\omega}) & \check{H}_1(e^{j\omega}) \\ \check{H}_1(e^{j(\omega+\pi)}) & \check{H}_0(e^{j(\omega+\pi)}) \end{bmatrix} \begin{bmatrix} \check{G}_0(e^{j\omega}) \\ \check{G}_1(e^{j\omega}) \end{bmatrix}. \quad (\text{E.14})$$

Appendix E. Derivation of the Compensation Filters

Solving the matrix equation leads to

$$\begin{bmatrix} \check{G}_0(e^{j\omega}) \\ \check{G}_1(e^{j\omega}) \end{bmatrix} = \begin{bmatrix} \frac{-\check{H}_0(e^{j(\omega+\pi)})}{P(e^{j\omega})} \\ \frac{\check{H}_1(e^{j(\omega+\pi)})}{P(e^{j\omega})} \end{bmatrix} e^{-j\omega\Delta} \quad (\text{E.15})$$

where

$$P(e^{j\omega}) = \check{H}_1(e^{j\omega})\check{H}_1(e^{j(\omega+\pi)}) - \check{H}_0(e^{j\omega})\check{H}_0(e^{j(\omega+\pi)}). \quad (\text{E.16})$$

Applying the IDFT as defined in (E.2) to (E.15) the transfer functions of the time-varying filter $g_n[l]$ is obtained as

$$\begin{bmatrix} G_0(e^{j\omega}) \\ G_1(e^{j\omega}) \end{bmatrix} = \begin{bmatrix} \frac{\check{H}_1(e^{j(\omega+\pi)}) - \check{H}_0(e^{j(\omega+\pi)})}{P(e^{j\omega})} \\ \frac{-\check{H}_1(e^{j(\omega+\pi)}) + \check{H}_0(e^{j(\omega+\pi)})}{P(e^{j\omega})} \end{bmatrix} e^{-j\omega\Delta}. \quad (\text{E.17})$$

By using (E.16) with a discrete-time version of (3.18) a further simplification of (E.17) is possible and the two precompensation filters are given as

$$G_0(e^{j\omega}) = \frac{2H_1(e^{j(\omega+\pi)})}{H_1(e^{j\omega})H_0(e^{j(\omega+\pi)}) + H_0(e^{j\omega})H_1(e^{j(\omega+\pi)})} e^{-j\omega\Delta}, \quad (\text{E.18})$$

and

$$G_1(e^{j\omega}) = \frac{2H_0(e^{j(\omega+\pi)})}{H_1(e^{j\omega})H_0(e^{j(\omega+\pi)}) + H_0(e^{j\omega})H_1(e^{j(\omega+\pi)})} e^{-j\omega\Delta}. \quad (\text{E.19})$$

E.1.2. FIR Filter Design Example

For the design example two-periodic holding signals with relative timing offsets of $r_0 = 0$ and $r_1 = 0.0312$ that are generated by a simulated 10-bit time-interleaved DAC are assumed. The digital signal has been a multi-tone signal with frequencies $[0.0542, 0.1123, 0.1704, 0.2285, 0.2866, 0.3447]f_s$. Without any compensation one obtains the energy density spectrum shown in Fig. E.2. It is seen that the output spectrum has a $\sin(x)/x$ shape and that there are additional distortions due to nonuniform holding effects. The largest unwanted spur in the fundamental band, i.e., the band between 0 and 0.5, is about -31 dBc.

To approximate the ideal frequency responses given by (E.17) causal finite-impulse response (FIR) filters $G_n^a(e^{j\omega})$ are used, which have transfer functions

$$G_n^a(e^{j\omega}) = \sum_{l=0}^N g_n[l] e^{-j\omega l} \quad (\text{E.20})$$

and approximate the ideal frequency responses in the minimax (Chebychev) sense, i.e.,

$$\min |G_n(e^{j\omega}) - G_n^a(e^{j\omega})|, \quad \omega \in [0, \omega_c], \quad \omega_c \leq \pi \quad (\text{E.21})$$

where frequencies above ω_c belong to the don't care band. The approximation problem has been solved by using the Matlab software CVX¹, where the designed filters are of order $N = 14$ with $\Delta = 7$ and $\omega_c = 0.8\pi$.

E.1. Two-Periodic Nonuniform Holding Signals

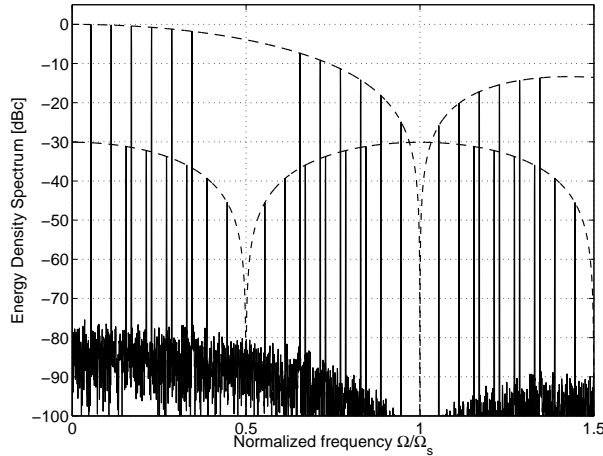


Figure E.2.: Output of the simulated 10-bit DAC with two-period nonuniform holding signals ($M=2$).

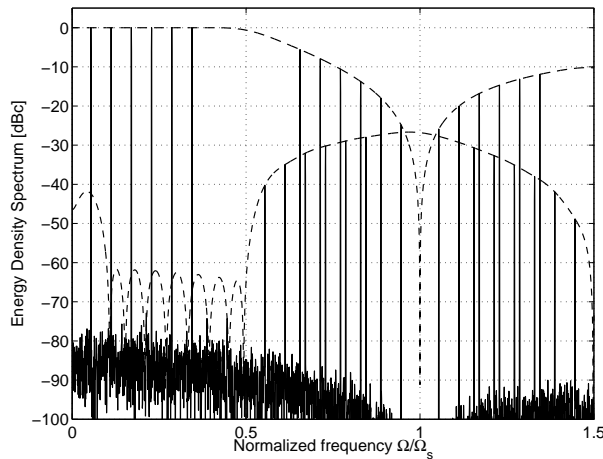


Figure E.3.: Output of the simulated 10-bit DAC with two-period nonuniform holding signals and time-varying precompensation filter.

The DAC output with precompensation is shown in Fig. E.3. Within the fundamental band the unwanted distortions are reduced considerably. The largest spur is about -62 dBc, which is an improvement of 31 dB compared to the uncompensated case. A higher attenuation of the distortions is achievable by increasing the filter order. When comparing the out-of-band energy of Fig. E.2 and Fig. E.3 it is recognized that the out-of-band energy in Fig. E.3 is slightly increased by about 2 dB. This minor amplification of the out-of-band energy should not influence the design of the analog reconstruction filter significantly. One possibility to overcome this issue is to include the influence of the compensation filter on the out-of-band energy as another filter design parameter.

¹<http://www.stanford.edu/boyd/cvx/>

Appendix E. Derivation of the Compensation Filters

Curriculum Vitae

Christoph Krall was born in St. Veit an der Glan, Austria, on October 25, 1979. After primary school he attended a technical college for telecommunication engineering, i.e., HTBLA Mössingerstraße, Klagenfurt, Austria. In 1999 he started his studies in Electrical Engineering at Graz University of Technology, Austria where he focused on communications engineering, signal processing, and information technology. His diploma thesis was written at Delft University of Technology, The Netherlands (Prof. Gerard J.M. Janssen) where he investigated nonlinear equalizer structures for a broadband wireless communication system. After finishing this project, he got the Dipl.-Ing. (MSc) degree in Jan. 2005 from Graz University of Technology.

In Feb. 2005 he started with his PhD research project at the Christian Doppler Laboratory for Nonlinear Signal Processing at Graz University of Technology, Austria. During this time he was again at Delft University of Technology, The Netherlands for a research visit of two months and worked with Prof. Alle-Jan van der Veen and Dr. Geert Leus. His research interests are wireless communication systems, nonlinear signal processing, and adaptive signal processing.

Appendix E. Derivation of the Compensation Filters

Bibliography

- [1] Federal Communications Commission, “Part 15 Rules,” FCC, <http://www.fcc.gov/oet/info/rules/part15/>, Tech. Rep., April 2007.
- [2] W. Hirt, “The European UWB Radio Regulatory and Standards Framework: Overview and Implications,” in *IEEE International Conference on Ultra Wideband (ICUWB2007)*, Singapore, September 2007, ☞.
- [3] B. Hosler, “Passing FCC Regulations and RF Design Challenges,” Wireless USB Developers Conference, May 2006, ☞.
- [4] A. F. Molisch, J. R. Foerster, and M. Pendergrass, “Channel Models for Ultrawideband Personal Area Networks,” *IEEE Personal Communications Magazine*, vol. 10, pp. 14 – 21, December 2003, ☞.
- [5] C. Ellison, “IOGEAR Wireless USB Hub and Adapter Review: Deja Vu all over again,” <http://www.smallnetbuilder.com/content/view/30175/85/1/3/>, September 2007, ☞.
- [6] *IEEE P802.15.4a-2007 (Amendment 1), 802.15.4: Wireless Medium Access Control (MAC) and Physical Layer (PHY) Specifications for Low-Rate Wireless PANs*, IEEE Computer Society Std., 2007, ☞.
- [7] J. D. Taylor, *Ultra-Wideband Radar Technology*. CRC Press LLC, 2001.
- [8] M.-G. Di Benedetto and G. Giancola, *Understanding Ultra Wide Band Radio Fundamentals*. Upper Saddle River, New Jersey 07458: Prentice Hall PTR, 2004.
- [9] C. Krall and K. Witrissal, “Parallel OFDM Signal Generation for UWB Systems,” in *2006 IEEE Conference on Ultra Wideband (ICUWB 2006)*, Waltham, MA, September 2006, pp. 243–247, ☞.
- [10] C. Krall, C. Vogel, and K. Witrissal, “Time-Interleaved Digital-to-Analog Converters for UWB Signal Generation,” in *2007 IEEE Conference on Ultra Wideband (ICUWB 2007)*, Singapore, September 2007, ☞.

Bibliography

- [11] K. Witrisal, G. Leus, M. Pausini, and C. Krall, "Equivalent System Model and Equalization of Differential Impulse Radio UWB Systems," *IEEE Journal on Selected Areas in Communications*, vol. 23, no. 9, pp. 1851–1862, September 2005, [↗](#).
- [12] Y. D. Alemseged, "Modeling and Mitigation of Narrowband Interference in Transmitted-Reference UWB Systems," Ph.D. dissertation, Graz University of Technology, Austria, March 2008, [↗](#).
- [13] C. Steiner and K. Witrisal, "Multiuser Interference Modeling and Suppression for a Multichannel Differential IR-UWB System," in *Proc. IEEE International Conference on Ultra-Wideband, ICU*, Zurich, Switzerland, September 2005, pp. 667–672, [↗](#).
- [14] C. Krall, K. Witrisal, H. Koepl, G. Leus, and M. Pausini, "Nonlinear Equalization for Frame-Differential IR-UWB Receivers," in *2005 IEEE Conference on Ultra Wideband (ICU 2005)*, Zurich, Switzerland, September 2005, pp. 576–581, [↗](#).
- [15] ECMA, *ECMA-368: High Rate Ultra Wideband PHY and MAC Standard*. Geneva, Switzerland: ECMA (European Association for Standardizing Information and Communication Systems), Jun. 2005, [↗](#). [Online]. Available: <http://www.ecma.ch/ecma1/STAND/ecma-368.htm>
- [16] A. F. Molisch, "Ultrawideband Propagation Channels - Theory, Measurement, and Modeling," *IEEE Trans. Veh. Technol.*, vol. 54, no. 5, pp. 1528 – 1545, September 2005, [↗](#).
- [17] A. F. Molisch, K. Balakrishnan, C.-C. Chong, S. Emami, A. Fort, J. Karedal, J. Kunisch, H. Schantz, U. Schuster, and K. Siwiak, "IEEE 802.15.4a channel model - final report," IEEE, Tech. Rep., November 2004, [↗](#).
- [18] A. Batra, J. Balakrishnan, G. Aiello, J. Foerster, and A. Dabak, "Design of a Multi-band OFDM System for Realistic UWB Channel Environments," *IEEE Trans. Microw. Theory Tech.*, vol. 52, no. 9, pp. 2123–2138, 2004, [↗](#).
- [19] R. Fisher, R. Kohno, M. Mc Laughlin, and M. Welborn, "DS-UWB Physical Layer Submission to 802.15 Task Group3a," IEEE P802.15-04/0137r3, Tech. Rep., July 2004, [↗](#).
- [20] ISO, *ISO/IEC 26907:2007: High Rate Ultra Wideband PHY and MAC Standard*. International Standardization Organization, Mar. 2007.
- [21] W. Alliance, "WiMedia Logical Link Control Protocol," The WiMedia Alliance, Tech. Rep., August 2007, [↗](#).
- [22] L. Hanzo, M. Münster, B. J. Choi, and T. Keller, *ODFM MC-CDMA for Broadband Multi-User Communications, WLANs and Broadcasting*. John Wiley & Sons Ltd., 2003.
- [23] H. Schulze and C. Lüders, *Theory and Applications of OFDM and CDMA Wideband Wireless Communications*. John Wiley & Sons Ltd., 2005.

- [24] M. Ibnkahla, *Signal Processing for Future Mobile Communications Systems: Challenges and Perspectives*. CRC Press, 2004.
- [25] S. B. Weinstein and P. M. Ebert, “Data Transmission by Frequency-Division Multiplexing Using the Discrete Fourier Transform,” *IEEE Trans. Commun. Technol.*, vol. 19, no. 5, pp. 628 – 634, October 1971, ☞.
- [26] P. Duhamel and M. Vetterli, “Fast Fourier Transforms: A Tutorial Review and a State of the Art,” *Signal Processing*, vol. 19, no. 4, pp. 259 – 299, 1990, ☞.
- [27] B. Daneshrad, L. J. Cimini, Jr., M. Carloni, and N. Sollenberger, “Performance and Implementation of Clustered OFDM for Wireless Communications,” *Mobile Networks and Applications*, vol. 2, pp. 305 – 314, 1997, Baltzer Science Publishers BV, ☞.
- [28] S. H. Müller and J. B. Huber, “OFDM with Reduced Peak-to-mean Power Ratio by Optimum Combination of Partial Transmit Sequences,” *Electronic Letters*, vol. 33, pp. 368 – 369, February 1997, ☞.
- [29] L. J. Cimini, Jr. and N. R. Sollenberger, “Peak-to-Average Power Ratio Reduction of an OFDM Signal Using Partial Transmit Sequences,” *IEEE Commun. Lett.*, vol. 4, no. 3, pp. 86 – 88, March 2000, ☞.
- [30] T. Beth, W. Fumy, and R. Mühlfeld, “Zur Algebraischen Diskreten Fourier-Transformation,” *Archiv der Mathematik*, vol. 40, no. 1, pp. 238 – 244, December 1983, ☞.
- [31] A. V. Oppenheim, R. W. Schaffer, and J. R. Buck, *Discrete-Time Signal Processing*, 2nd ed. Prentice Hall Inc., 1998.
- [32] B. Muquet, Z. Wang, G. Giannakis, M. de Courville, and P. Duhamel, “Cyclic Prefixing or Zero Padding for Wireless Multicarrier Transmissions?” *IEEE Trans. Commun.*, vol. 50, no. 12, pp. 2136–2148, 2002, ☞.
- [33] T. S. Rappaport, *Wireless Communications - Principles and Practice*. Prentice Hall, Inc., 1999.
- [34] M. Pätzold, *Mobile Fading Channels*, 2nd ed. John Wiley & Sons Ltd., 2002.
- [35] R. Steele and L. Hanzo, Eds., *Mobile Radio Communications*, 2nd ed. John Wiley & Sons, Ltd., 1999.
- [36] J. G. Proakis, *Digital Communications*, 4th ed. McGraw-Hill International, 2001.
- [37] F. J. Harris, “On the Use of Windows for Harmonic Analysis with the Discrete Fourier Transform,” *Proc. IEEE*, vol. 66, no. 1, pp. 51 – 83, January 1978, ☞.
- [38] R. E. Crochiere and L. R. Rabiner, *Multirate Digital Signal Processing*. Prentice Hall Inc., 1983.

Bibliography

- [39] P. P. Vaidyanathan and K. Swaminathan, "Alias-Free, Real-Coefficient m -Band QMF Banks for Arbitrary m ," *IEEE Trans. Circuits Syst.*, vol. CAS-34, no. 12, pp. 1485 – 1496, December 1987, [↗](#).
- [40] P. P. Vaidyanathan, "Quadrature Mirror Filter Banks, M-Band Extensions and Perfect-Reconstruction Techniques," *IEEE ASSP Mag.*, pp. 4 – 20, July 1987, [↗](#).
- [41] Y. C. Lim, "Frequency-Response Masking Approach for the Synthesis of Sharp Linear Phase Digital Filters," *IEEE Trans. Circuits Syst.*, vol. CAS-33, pp. 357 – 364, April 1986, [↗](#).
- [42] Y. C. Lim and Y. Lian, "Frequency-Response Masking Approach for Digital Filter Design: Complexity Reduction via Masking Filter Factorization," *IEEE Trans. Circuits Syst. II*, vol. 41, no. 8, pp. 518 – 525, August 1994, [↗](#).
- [43] L. Feng and W. Namgoong, "An Adaptive Maximally Decimated Channelized UWB Receiver with Cyclic Prefix," *IEEE Trans. Circuits Syst. I*, vol. 52, no. 10, pp. 2165–2172, 2005, [↗](#).
- [44] *16-Bit, 500MSps, 2x - 16x Interpolating Dual-Channel DAC*, <http://www.ti.com>, Texas Instruments, [↗](#).
- [45] *16-Bit 160 MSPS 2x/4x/8x Interpolating Dual TxDAC® + D/A Converter*, <http://www.analog.com>, Analog Devices, [↗](#).
- [46] E. A. Lee and D. G. Messerschmitt, *Digital Communication*, 2nd ed. Kluwer Academic Publishers, 1994.
- [47] S. Gezici, Z. Tian, G. Giannakis, H. Kobayashi, A. Molisch, H. Poor, and Z. Sahinoglu, "Localization via Ultra-Wideband Radios: A Look at Positioning Aspects for Future Sensor Networks," *IEEE Signal Process. Mag.*, vol. 22, no. 4, pp. 70–84, July 2005, [↗](#).
- [48] C. Vogel and C. Krall, "Compensation of Distortions Due to Periodic Nonuniform Holding Signals," in *IEEE 6th Symposium on Communication Systems, Networks and Digital Signal Processing (CSNDSP)*, submitted, Graz, Austria, July 2008, [↗](#).
- [49] B. Hu and N. Beaulieu, "Pulse Shapes for Ultra Wideband Communication Systems," *Wireless Communications, IEEE Transactions on*, vol. 4, no. 4, pp. 1789–1797, 2005, [↗](#).
- [50] F. C. Moon, *Chaotic and fractal dynamics*. John Wiley & Sons, Inc., 1992.
- [51] "Analog Devices AD9734 10-Bit, 1200 MSPS D/A Converter," Sept. 2006. [Online]. Available: <http://www.analog.com>
- [52] F. Maloberti, "High-speed data converters for communication systems," *IEEE Circuits Syst. Mag.*, vol. 1, no. 1, pp. 26–36, 2001, [↗](#).

- [53] G. Gielen, R. Rutenbar, S. Borkar, R. Brodersen, J.-H. Chern, E. Naviasky, D. Saias, and C. Sodini, “Tomorrow’s analog: just dead or just different?” in *2006 43rd ACM/IEEE Design Automation Conference*, San Francisco, CA, 2006, pp. 709–710, [↗](#).
- [54] B. Murmann, “Digitally Assisted Analog Circuits,” *IEEE Micro*, vol. 26, no. 2, pp. 38–47, March–April 2006, [↗](#).
- [55] M. Clara, W. Klatzer, A. Wiesbauer, and D. Straeußnigg, “A 350MHz low-OSR $\Delta\Sigma$ current-steering DAC with active termination in 0.13 μm CMOS,” in *2005 IEEE International Solid-State Circuits Conference, 2005. Digest of Technical Papers. ISSCC*, San Francisco, CA, 2005, pp. 118–588 Vol. 1, [↗](#).
- [56] R. Adams, K. Nguyen, and K. Sweetland, “A 113-dB SNR Oversampling DAC with Segmented Noise-Shaped Scrambling,” *IEEE J. Solid-State Circuits*, vol. 33, no. 12, pp. 1871–1878, 1998, [↗](#).
- [57] A. G. Venes, K. L. Miller, and P. Vorenkamp, “Method and System for Time Interleaved Digital to Analog Conversion for a Cable Modem,” U.S. Patent US2 006 098 823, May, 2006, [↗](#).
- [58] Xilinx, “Virtex-4 ML403 Embedded Platform,” Xilinx Inc., Tech. Rep., May 2006. [Online]. Available: <http://www.xilinx.com>
- [59] “Stanford Research Systems CG635 Synthesized Clock Generator,” 2006. [Online]. Available: <http://www.thinksrs.com/products/CG635.htm>
- [60] U. Seng-Pan, S. Sai-Weng, and R. Martins, “Exact spectra analysis of sampled signals with jitter-induced nonuniformly holding effects,” *IEEE Trans. Instrum. Meas.*, vol. 53, no. 4, pp. 1279–1288, August 2004, [↗](#).
- [61] L. Angrisani, M. D’Apuzzo, and M. D’Arco, “Modeling timing jitter effects in digital-to-analog converters,” in *2005 IEEE International Workshop on Intelligent Signal Processing*, Faro, Portugal, September 2005, pp. 254–259, [↗](#).
- [62] D. Domanin, U. Gatti, P. Malcovati, and F. Maloberti, “A multipath polyphase digital-to-analog converter for software-radio transmission systems,” in *The 2000 IEEE International Symposium on Circuits and Systems*, vol. 2, Geneva, Switzerland, May 2000, pp. 361–364, [↗](#).
- [63] C.-K. Yang, V. Stojanovic, S. Modjtahedi, M. Horowitz, and W. Ellersick, “A serial-link transceiver based on 8-GSamples/s A/D and D/A converters in 0.25- μm CMOS,” *IEEE J. Solid-State Circuits*, vol. 36, no. 11, pp. 1684–1692, November 2001, [↗](#).
- [64] Y.-C. Jenq, “Digital-to-analog (D/A) converters with nonuniformly sampled signals,” *IEEE Trans. Instrum. Meas.*, vol. 45, no. 1, pp. 56–59, February 1996, [↗](#).
- [65] Y. C. Jenq, “Digital Spectra of Nonuniformly Sampled Signals: A Robust Sampling Time Offset Estimation Algorithm for Ultra High-Speed Waveform Digitizers Using

Bibliography

- Interleaving,” *IEEE Trans. Instrum. Meas.*, vol. 39, no. 1, pp. 71–75, February 1990, [↗](#).
- [66] C. Farrow, “A Continuously Variable Digital Delay Element,” in *The 1988 IEEE International Symposium on Circuits and Systems*, vol. 3, Helsinki, Finland, June 1988, pp. 2641–2645, [↗](#).
- [67] M. Win, G. Chrisikos, and N. Sollenberger, “Performance of RAKE Reception in Dense Multipath Channels: Implications of Spreading Bandwidth and Selection Diversity Order,” *IEEE J. Sel. Areas Commun.*, vol. 18, no. 8, pp. 1516–1525, August 2000, [↗](#).
- [68] —, “Effects of Chip Rate on Selective RAKE Combining,” *IEEE Commun. Lett.*, vol. 4, no. 7, pp. 233–235, July 2000, [↗](#).
- [69] M. Weisenhorn and W. Hirt, “Robust Noncoherent Receiver Exploiting UWB Channel Properties,” in *Ultra Wideband Systems, 2004. Joint with Conference on Ultra-wideband Systems and Technologies*, Kyoto, Japan, 18-21 May 2004, pp. 156–160, [↗](#).
- [70] F. Troesch, F. Althaus, and A. Wittneben, “Modified Pulse Repetition Coding Boosting Energy Detector Performance in Low Data Rate Systems,” in *Ultra-Wideband, 2005. ICU 2005. 2005 IEEE International Conference on*, Zurich, Switzerland, 5-8 Sept. 2005, pp. 508–513, [↗](#).
- [71] C. Rushforth, “Transmitted-Reference Techniques for Random or Unknown Channels,” *IEEE Trans. Inf. Theory*, vol. 10, no. 1, pp. 39–42, Jan. 1964, [↗](#).
- [72] M. Pausini, “Autocorrelation Receivers for Ultra Wideband Wireless Communications,” Ph.D. dissertation, Delft University of Technology, The Netherlands, December 2007, [↗](#).
- [73] T. Q. S. Quek and M. Z. Win, “Analysis of UWB Transmitted-Reference Communication Systems in Dense Multipath Channels,” *IEEE J. Sel. Areas Commun.*, vol. 23, no. 9, pp. 1863 – 1874, September 2005, [↗](#).
- [74] Q. Dang, A. Trindade, A.-J. van der Veen, and G. Leus, “Signal Model and Receiver Algorithms for a Transmit-Reference Ultra-Wideband Communication System,” *IEEE J. Sel. Areas Commun.*, vol. 24, no. 4, pp. 773–779, April 2006, [↗](#).
- [75] R. Hoor and H. Tomlinson, “Delay-Hopped Transmitted-Reference RF Communications,” in *2002 IEEE Conference on Ultra Wideband Systems and Technologies, 2002. Digest of Papers.*, Baltimore, MD, 2002, pp. 265–269, [↗](#).
- [76] U. Schuster and H. Bölcskei, “Ultrawideband Channel Modeling on the Basis of Information-Theoretic Criteria,” *IEEE Trans. Wireless Commun.*, vol. 6, no. 7, pp. 2464 – 2475, July 2007, [↗](#).
- [77] R. Hoor and H. Tomlinson, “Delay-Hopped Transmitted-Reference RF Communications,” in *2002 IEEE Conference on Ultra Wideband Systems and Technologies, 2002. Digest of Papers.*, Baltimore, MD, 2002, pp. 265–269, [↗](#).

- [78] C. Krall, K. Witrissal, G. Leus, and H. Koepl, “Minimum Mean Squared Error Equalization for Second-Order Volterra Systems,” *IEEE Trans. Signal Process.*, 2007, submitted.
- [79] J. Romme, “UWB Channel Fading Statistics and Transmit-Reference Communication,” Ph.D. dissertation, Graz University of Technology, Austria, March 2008, [↗](#).
- [80] S. Franz and U. Mitra, “Integration Interval Optimization and Performance Analysis for UWB Transmitted Reference Systems,” in *2004 International Workshop on Ultra Wideband Systems*, Kyoto, Japan, May 2004, pp. 26–30, [↗](#).
- [81] C. Steiner, “Multiuser Interference Modeling and Suppression for Differential IR-UWB Systems,” Master’s thesis, Graz University of Technology, Austria, 2005, [↗](#).
- [82] S. Haykin, *Neural Networks: A Comprehensive Foundation*. MacMillan Publishing Company, 1994.
- [83] M. Schetzen, *The Volterra and Wiener Theories of Nonlinear Systems*. New York: Krieger Publishing, 1980.
- [84] V.J. Mathews and G. L. Sicuranza, *Polynomial Signal Processing*. Wiley-Interscience, 2000.
- [85] R. Hermann, “Volterra modeling of digital magnetic saturation recording channels,” *IEEE Trans. Magn.*, vol. 26, no. 5, pp. 2125–2127, Sep 1990, [↗](#).
- [86] S. Benedetto and E. Biglieri, “Nonlinear Equalization of Digital Satellite Channels,” *IEEE J. Sel. Areas Commun.*, vol. 1, no. 1, pp. 57–62, Jan. 1983, [↗](#).
- [87] H. Koepl and P. Singerl, “An efficient scheme for nonlinear modeling and predistortion in mixed-signal systems,” *IEEE Trans. Circuits Syst. II*, vol. 53, no. 12, pp. 1368–1372, Dec. 2006, [↗](#).
- [88] F. Gao and W. Snelgrove, “Adaptive Linearization of a Loudspeaker,” in *1991 International Conference on Acoustics, Speech, and Signal Processing, ICASSP*, vol. 5, Toronto, Canada, April 1991, pp. 3589–3592, [↗](#).
- [89] E. Aschbacher and M. Rupp, “Modelling and identification of a nonlinear power-amplifier with memory for nonlinear digital adaptive pre-distortion,” in *4th IEEE Workshop on Signal Processing Advances in Wireless Communications, SPAWC 2003*, Rome, Italy, 15-18 June 2003, pp. 658–662, [↗](#).
- [90] E. A. Lee, D. G. Messerschmitt, and J. R. Barry, *Digital Communication*. Springer Netherlands, 2004.
- [91] M. Ibnkahla, Ed., *Signal Processing for Mobile Communications Handbook*. CRC Press, 2005.








Bibliography

- [92] A. Carini, J. V. Mathews, and G. L. Sicuranza, "Exact and p th Order Equalization and Linearization of Recursive Polynomial Systems," in *Thirty-Second Asilomar Conference on Signals, Systems & Computers*, Pacific Grove, CA, USA, Nov. 1998, pp. 688 – 692, ☞.
- [93] E. Mumolo and A. Carini, "On the Stability of Discrete Time Recursive Volterra Filters," *IEEE Signal Process. Lett.*, vol. 6, no. 9, pp. 230–232, Sept. 1999, ☞.
- [94] M. Schetzen, "Theory of p th-Order Inverses of Nonlinear Systems," *IEEE Trans. Circuits Syst.*, vol. CAS-23, no. 5, pp. 285–291, May 1976, ☞.
- [95] G. B. Giannakis and E. Serpedin, "Linear Multichannel Blind Equalizers of Nonlinear FIR Volterra Channels," *IEEE Trans. Signal Process.*, vol. 45, no. 1, pp. 67 – 81, January 1997, ☞.
- [96] J. Romme and K. Witrisal, "Transmitted-Reference UWB Systems using Weighted Autocorrelation Receivers," *IEEE Trans. Microw. Theory Tech.*, vol. 54, no. 4, pp. 1754–1761, April 2005, ☞.
- [97] A. Redfern and G. Zhou, "A Root Method for Volterra System Equalization," *IEEE Signal Process. Lett.*, vol. 5, no. 11, pp. 285–288, Nov. 1998, ☞.
- [98] R. Nowak and B. Van Veen, "Volterra Filter Equalization: A Fixed Point Approach," *IEEE Trans. Signal Process.*, vol. 45, no. 2, pp. 377–388, Feb. 1997, ☞.
- [99] S. Im, "Adaptive Equalization of Nonlinear Digital Satellite Channels Using a Frequency-Domain Volterra Filter," in *Military Communications Conference, 1996. MILCOM '96, Conference Proceedings, IEEE*, vol. 3, McLean, VA, Oct. 1996, pp. 843 – 848, ☞.
- [100] G. Raz and B. Van Veen, "Blind Equalization and Identification of Nonlinear and IIR Systems-A Least Squares Approach," *IEEE Trans. Signal Process.*, vol. 48, no. 1, pp. 192–200, Jan. 2000, ☞.
- [101] V. S. Kafka and U. Appelt, "Nonlinear Equalization by Recursive Polynomial Systems with a Nonlinear Predictor," in *IEEE-EURASIP Workshop on Nonlinear Signal and Image Processing, NSIP'01*, Baltimore, MD, 2001, ☞.
- [102] S. Haykin, *Adaptive Filter Theory*, 4th ed. Prentice Hall, 2002.
- [103] V. J. Mathews, "Adaptive Polynomial Filters," *IEEE Signal Process. Mag.*, vol. 8, pp. 10 – 26, July 1991, ☞.
- [104] C. Krall, "Nonlinear Equalization for a Frame-Differential IR-UWB Receiver," Master's thesis, Delft University of Technology, The Netherlands, August 2004, ☞.
- [105] S. Egger, "UWB Demonstrator with Scope on Synchronization," Master's thesis, Graz University of Technology, March 2007, ☞.
- [106] B. Schiffer, "Design of a UWB Antenna," Graz University of Technology, Tech. Rep., 2007.

- [107] *The LVDS Owners Manual*, 3rd ed., National Semiconductor, 2004, ☞.
- [108] M. Hiebel, *Fundamentals of Vector Network Analysis*. Munich, Germany: Rohde and Schwarz Press, 2007.
- [109] H. Schantz, *The Art and Science of Ultra-Wideband Antennas*. Artech House, 2005.
- [110] J. E. Hansen, *Spherical Near-Field Antenna Measurements*. Stevenage, Herts, UK: The Institution of Engineering and Technology, IET, 1988.
- [111] C. A. Balanis, *Antenna Theory*, 2nd ed. John Wiley & Sons Ltd., 1997.
- [112] W. Ciccognani, A. Durantini, and D. Cassioli, “Time Domain Propagation Measurements of the UWB Indoor Channel Using PN-Sequence in the FCC-Compliant Band 3.6-6 GHz,” *IEEE Trans. Antennas Propag.*, vol. 53, no. 4, pp. 1542–1549, 2005, ☞.
- [113] J. Keignart, J.-B. Pierrot, N. Daniele, A. Alvarez, M. Lobeira, J. L. Garcia, G. Valera, and R. P. Torres, “U. C. A. N. Report on UWB Basic Transmission Loss,” U.C.A.N., Tech. Rep. IST-2003-32710-U.C.A.N., March 2003, ☞.
- [114] B. Kannan *et. al.*, “UWB Channel Characterization in Indoor Office Environments,” IEEE, Tech. Rep. 802.15-04-0439-00-004a, August 2004, ☞.
- [115] —, “UWB Channel Characterization in Outdoor Environments,” IEEE, Tech. Rep. 802.15-04-0440-00-004a, August 2004, ☞.
- [116] J. Karedal, S. Wyne, P. Almers, F. Tufvesson, and A. Molisch, “Statistical analysis of the UWB channel in an industrial environment,” in *2004 IEEE 60th Vehicular Technology Conference, 2004. VTC2004-Fall.*, vol. 1, Los Angeles, CA, 2004, pp. 81–85 Vol. 1, ☞.
- [117] D. Cassioli, W. Ciccognani, and A. Durantini, “UWB Channel Model Report,” Ultrawaves, Tech. Rep. IST-2001-35189, November 2003, ☞.
- [118] J. Kunisch and J. Pamp, “Measurement Results and Modeling Aspects for the UWB Radio Channel,” *IEEE Conference on Ultra Wideband Systems and Technologies*, pp. 19 – 23, 2002, ☞.
- [119] A. Álvarez, G. Valera, M. Lobeira, R. Torres, and J. L. García, “New Channel Impulse Response Model for UWB Indoor System Simulations,” in *Proceedings VTC 2003 spring*, Jeju, Korea, 2003, pp. 1 – 5, ☞.
- [120] B. Sklar, “Rayleigh Fading Channels in Mobile Digital Communication Systems Part I: Characterization,” *IEEE Commun. Mag.*, vol. 35, no. 7, pp. 90 – 100, July 1997, ☞.
- [121] V. Erceg, L. J. Greenstein, S. Y. Tajandra, S. R. Parkoff, A. Gupta, B. Kulic, A. A. Julius, and R. Bianchi, “An Empirically Based Path Loss Model for Wireless Channel in Suburban Environments,” *IEEE J. Sel. Areas Commun.*, pp. 1205 – 1211, 1999, ☞.

Bibliography

- [122] S. S. Ghassemzadeh, R. Jana, C. W. Rice, W. Turin, and V. Tarokh, "Measurement and Modeling of an Ultra-Wide Bandwidth Indoor Channel," *IEEE Trans. Commun.*, pp. 1786 – 1796, 2004, ☞.
- [123] A. Papoulis and S. Unnikrishna Pillai, *Probability, Random Variables and Stochastic Processes*, 4th ed. Mc Graw Hill, 2002.
- [124] M. Nakagami, "The m - distribution, a general formula of intensity distribution for rapid fading," in *Statistical Methods of Radio Wave Propagation: Proceedings of a Symposium held at the University of California, Pergamon Press*, 1960, pp. 3 – 36.
- [125] D. Cassioli, M. Z. Win, and A. F. Molisch, "The Ultra-Wide Bandwidth Indoor Channel: From Statistical Model to Simulations," *IEEE J. Sel. Areas Commun.*, vol. 20, no. 6, pp. 1247 –1257, August 2002, ☞.
- [126] D. Cassioli and A. Durantini, "A time-domain propagation model of the uwb indoor channel in the fcc-compliant band 3.6 - 6 ghz based on pn-sequence channel measurements," in *IEEE 59th Vehicular Technology Conference, 2004. VTC 2004-Spring.*, vol. 1, Milan, Italy, 2004, pp. 213–217 Vol.1, ☞.
- [127] S. O. Rice, "Mathematical analysis of random noise," *Bell Systems Tech. Journal*, vol. 23, pp. 282 – 332, 1954, ☞.
- [128] —, "Mathematical analysis of random noise," *Bell Systems Tech. Journal*, vol. 24, pp. 46 – 156, 1954, ☞.
- [129] V. Hovinen, M. Hämäläinen, and T. Patsi, "Ultra Wideband Indoor Radio Channel Models: Preliminary Results," in *2002 IEEE Conference on Ultra Wideband Systems and Technologies, 2002. Digest of Papers.*, Baltimore, MD, 2002, pp. 75–79, ☞.
- [130] H. Hashemi, "The Indoor Radio Propagation Channel," *Proc. IEEE*, vol. 81, no. 7, pp. 943 – 968, 1993, ☞.
- [131] J. R. Foerster and Q. Li, "Uwb Channel Modeling Contribution from Intel," Intel Corporation, Hillboro, OR, USA, Tech. Rep. P802.15 02/279SG3a, June 2002, ☞.
- [132] D. S. Polydorou and C. N. Capsalis, "A new theoretical model for the prediction of rapid fading variations in an indoor environment," *IEEE Trans. Veh. Technol.*, vol. 46, no. 3, pp. 748 – 754, August 1997, ☞.
- [133] H. Zhang, T. Udagawa, T. Arita, and M. Nakagawa, "A statistical model for the small-scale multipath fading characteristics of ultra wideband indoor channel," in *2002 IEEE Conference on Ultra Wideband Systems and Technologies*, vol. Digest of Papers, Baltimore, MD, 2002, pp. 81 – 86, ☞.
- [134] P. Pagani and P. Pajusco, "Experimental assessment of the uwb channel variability in a dynamic indoor environment," in *15th IEEE International Symposium on Personal, Indoor and Mobile Radio Communications, 2004. PIMRC 2004.*, vol. 4, Barcelona, Spain, 2004, pp. 2973–2977 Vol.4, ☞.

- [135] G. L. Turin, F. D. Clapp, T. L. Johnston, S. B. Fine, and D. Lavry, "A Statistical Model of Urban Multipath Propagation," *IEEE Trans. Veh. Technol.*, vol. VT-21, no. 1, pp. 1 – 9, 1972, .
- [136] P. A. Bello, "Characterization of Randomly Time-Variant Linear Channels," *IEEE Trans. Commun.*, vol. 11, pp. 360 – 393, December 1963, .
- [137] A. A. M. Saleh and R. A. Valenzuela, "A Statistical Model for Indoor Multipath Propagation," *IEEE J. Sel. Areas Commun.*, vol. SAC-5, no. 2, pp. 128 – 137, February 1987, .
- [138] C.-C. Chong, Y. Kim, and S.-S. Lee, "A Modified S-V Clustering Channel Model for the UWB Indoor Residential Environment," in *Proceedings IEEE VTC Spring 05*, Stockholm, Sweden, June 2005, .
- [139] A. F. Molisch, Ed., *Wideband Wireless Digital Communications*. Prentice Hall PTR, 2001.
- [140] J. Keignart and N. Daniele, "Subnanosecond uwb channel sounding in frequency and temporal domain," in *2002 IEEE Conference on Ultra Wideband Systems and Technologies, 2002. Digest of Papers.*, Baltimore, MD, 2002, pp. 25–30, .
- [141] A. S. Y. Poon and M. Ho, "Indoor multiple-antenna channel characterization from 2 to 8 ghz," in *IEEE International Conference on Communications, 2003. ICC '03.*, vol. 5, Anchorage, AK, 2003, pp. 3519–3523 vol.5, .
- [142] C.-C. Chong, Y. Kim, and D.-S. Lee, "UWB Indoor Propagation Channel Measurements and Data Analysis in Various Types of High-Rise Apartments," *The 60th IEEE Semiannual Conference on Vehicular Technology*, pp. 150 – 154, September 2004, .
- [143] A. Graham, *Kronecker Products and Matrix Calculus With Applications*. Ellis Horwood Ltd., 1981.
- [144] J. H. van Lint and R. M. Wilson, *A Course in Combinatorics*, 1st ed. Cambridge University Press, 1993.
- [145] P. P. Vaidyanathan, *Multirate Systems and Filter Banks*. Prentice Hall, 1993.